Dissertation
submitted to the
Combined Faculties of the Natural Sciences and Mathematics
of the Ruperto-Carola-University of Heidelberg. Germany
for the degree of
Doctor of Natural Sciences

Put forward by
Jakob Herpich
born in Rostock, Germany
Oral examination: May 8, 2017

# On the Physical Origin of Radial Surface Density Profiles in Disk Galaxies

Für Opa Friedemann

## On the Physical Origin of Radial Surface Density Profiles in Disk Galaxies

Observations have long established that the radial stellar surface density profiles in disk galaxies are nearly exponential (Type-I profiles). Stellar disks in numerical simulations also tend to approach an exponential profile. Deep imaging has revealed systematic deviations in the profile at large galactocentric radii. Beyond a break the profile may continue with a steeper (Type-II) or shallower (Type-III) exponential profile. In this thesis, I present numerical and analytical models that aim towards a physical understanding of how such profiles come about. I carried out numerical simulations designed to give extensive control over the physical conditions of disk galaxy formation. On this basis, I argue that the type of profile correlates with the initial spin of a galaxy's host dark matter halo: Type-II/III disks are hosted by high-/low-spin halos. Type-I disks occur at intermediate spins. The formation mechanism for the Type-II disks is consistent with previous results in the literature. Through a very detailed analysis of the low-spin simulations I show that the formation of Type-III profiles can be linked to the formation of a strong bar in low-spin halos. Observational predictions are provided to test the presented hypotheses.

The evolution of the radial disk structure can be interpreted as shuffling of the individual stars' angular momenta. Maximizing a suitably defined entropy in stellar angular momentum space yields an analytic prediction for the radial surface density profiles, given any galactic rotation curve and the corresponding stellar mass and angular momentum of the disk. I carefully compare this result with observational data and simulated disks. It gives a fair match to observations and is in very good agreement with those simulations that provide the closest match to the model assumption of perfectly circular stellar orbits.

## Über die physikalischen Ursachen radialer Flächendichteprofile von stellaren Scheiben in Spiralgalaxien

Beobachtungen ergaben, dass das radiale Flächendichteprofil von Spiralgalaxien exponentiell abfällt (Profil vom Typ-I). Auch in numerischen Simulationen treten exponentielle Profile auf. Genauere Beobachtungen zeigen, dass diese Profile *gebrochen* sein können. Außerhalb eines solchen Bruchs ist das Profil wieder expoentiell aber steiler (Typ-II) oder flacher (Typ-III). Diese Arbeit zielt darauf ab, dem physikalischen Ursprung dieser beobachteten Profile näher zu kommen. Der erste Teil der Arbeit basiert auf numerischen Simulationen. Diese wurden so geplant, dass sie möglichst gute Kontrolle der physikalischen Bedingungen bei der Scheibenentstehung ermöglichen. Die Ergebnisse legen nahe, dass der Profiltyp vom anfänglichen Gesamtdrehimpuls des dunkle Materie Halos abhängt, der die entsprechende Galaxie beherbergt. Bei geringem Drehimpuls entstehen Typ-II, bei hohem Typ-III und dazwischen Typ-I Profile. Die simulierten Typ-II Profile entsprechen in ihrer Entwicklung bereits, aus der Literatur, bekannten Ergebnissen. Die Entstehung von Typ-III Profilen kann mit der Entstehung eines massiven Balkens in Verbindung gebracht werden. Es werden beobachtbare Vorhersagen zur Verifizierung dieser Hypothese gemacht.

Im zweiten Teil wird eine analytische Formel für radiale Flächendichteprofile abgeleitet. Diese hängt ab von der galaktischen Rotationskurve sowie der Masse und dem Drehimpuls der stellaren Scheibe. Ein sorgfältiger und ausführlicher Vergleich mit Beobachtungen ergibt moderate Übereinstimmung, der mit Simulationen gute Übereinstimmung — sofern die Modellvoraussetzung perfekter Kreisbahnen aller Sterne gut angenähert wird.

# Contents

# Preface

In this thesis, I document four years of research on stellar dynamics in disk galaxies. This is a contribution to the field of fundamental research on the origin and evolution of the Universe usually referred to as *cosmology*. It does not have any immediate technical, medical, social, or political application. The motivation to pursue such a quest lies in human curiosity, in the human desire to close gaps of knowledge, to explore what is beyond the limits of our imagination. To me, this means to uncover the yet unknown characteristics of our Universe. In the case of this thesis, it is a better understanding of what may shape the disks of spiral galaxies. That is why I attempted to complete a PhD in Astrophysics.

This thesis is my contribution to the quest of understanding the origin of our Universe and its evolution. Its scientific results have been published by or submitted to a major astrophysical journal. It is my hope that these results will trigger further research on the topic of galactic disk morphology.

I start this thesis with a brief summary of textbook knowledge (e.g. Dodelson 2003; Mo et al. 2010) about the currently favored model of cosmology and galaxy formation. In doing so, I also highlight the importance of galaxies as probes for cosmological models. Given their key role in cosmological research, I extensively review the current state of research on galaxies. This has a particular focus on stellar dynamics in disk galaxies, which is the main subject of research presented in this thesis. The following three chapters are each dedicated to a major project covered in this thesis. Each of these correspond to a paper of which I am first author and that is either submitted to or accepted by a major peer-reviewed astrophysical journal. In chapter 2, I introduce numerical simulations, which reproduce all types of observed radial profiles of stellar disks in galaxies. This marks an unprecedented accomplishment. The formation of one kind of these profiles, antitruncations, is not yet fully understood. In chapter 3, I show that the formation of strong galactic bars can be dynamically linked to the formation of these profiles. This conclusion is based on a detailed analysis of the respective subset of simulations from chapter 2. While bars have been previously suspected to be related to antitruncated disks, no specific dynamical process has yet been published in the literature. The third project of this thesis is to develop an analytical model for the radial profile of disk galaxies which is based on statistical mechanics. It is described in chapter 4 and is a

unique approach that explains why radial profiles in observed and simulated galaxies naturally approach a near-exponential shape. The thesis is closed by a summary of the projects and a discussion of their implications. I also address unsolved issues and discuss possible paths leading to prospective answers.

A lot of the work presented in this thesis is the result of collaborative efforts. This includes supervision by my advisers, coding and providing simulation software, the scientific expertise of my colleagues to name the most significant support. Throughout this thesis I use the grammatical form of singular (I/me) to refer to work that I did myself and use the plural (we/us) to mark work that was done by or with my collaborators. Wherever appropriate, I explicitly name the specific person that deserves credit for respective contributions. All people that contributed to this thesis are explicitly named in the Acknowledgments at the end of this thesis.

The papers (Herpich et al. 2015a,b, 2017) that this thesis is based on have been written mostly my myself. The text of the respective chapters is based on that of the papers. Where appropriate I edited the text to match the context of this thesis, I changed parts of the text, and added some additional content and information.

# 1 Introduction

The field of astronomy is the oldest natural science and prototypical for today's empirical sciences. The historical importance of observing and studying celestial objects is based on mystical properties that ancient peoples assigned to them. Additionally, practical applications, such as the creation of calendars, caused our ancestors to observe and record the objects' motion on the sky (North 2008).

The early humans' capabilities of observing the sky were limited to those of their naked eyes. Thus, their astronomy relied on studying only those celestial objects that are visible by eye, namely the sun, the moon, bright planets, and very bright (close-by) stars. This did not stop ancient astronomers from pursuing astronomy as a quantitative science. They collected a large body of astrometric data and stellar brightnesses (North 2008).

In the early 17$^{\text{th}}$ century the telescope was invented. This marked the most influential revolution in astronomy to this day. Within the following few years, it helped astronomers, in particular Galilei and Kepler, to make ground breaking discoveries (Sengerling and North 2012). The most relevant for the field of cosmology was to resolve individual stars in the *Milky Way*. It marks the first observational hint that the sun is hosted by a galaxy.

In the meantime, modern technology has allowed for the development of very sophisticated telescopes and instruments that have greatly advanced our knowledge about the celestial objects and the Universe. The largest optical telescopes to date have primary mirrors with a diameter of about 10 m. The *European Extremely Large Telescope* (E-ELT) is currently under construction and will be the world's largest optical telescope with a primary dish of almost 40 m. Other than growing bigger, observational technology now allows for extending the observable range of the electromagnetic spectrum to cover the entire range from the very low radio frequencies up to high energy gamma-rays. Due to the opacity of the Earth's atmosphere for large parts of the electromagnetic spectrum, the corresponding ranges can only be observed with space-borne observatories. These have the additional advantage that their observations are not subject to atmospheric turbulence; and hence achieve a better angular resolution. Some radio observatories achieve even better angular resolution through interferometric observations, e.g. the *Atacama Large Millimeter Array* (ALMA).

The development of high resolution spectroscopy enables astronomers to go beyond plain photometric imaging of celestial objects. It allows for the detection of absorption and emission lines from atoms, ions, and complex molecules. With such data, the abundance of chemical elements and molecules can be measured; and hence the chemical composition of astronomical objects. Spectroscopy is also essential for (i) studying the dynamics and kinematics of these objects through detecting the Doppler shift of emission or absorption lines and (ii) for measuring the cosmological redshift of distant objects (see section 1.1.1).

All these advances in observational techniques have driven the limits of the observable Universe far beyond those from the time of the first telescopes. Consequently, our understanding about cosmology and galaxies has made extraordinary progress. In this chapter, I review the current state of scientific knowledge in these fields while focusing on the aspects, which are most relevant for the understanding of the presented research.

Current and future observational missions, like the Gaia satellite or the *James Webb Space Telescope* (JWST), are going to increase the body of data even further. These will allow the research community to test their theories, to constrain their models, and ultimately to discover the unexpected that may revolutionize our picture of the Universe. The recent discovery of gravitational waves by the LIGO experiment (Abbott et al. 2016) even opened up a completely different, non-electromagnetic, window for observing the Universe.

## 1.1 The Standard Model of Cosmology

The Universe is believed to originate from an initially hot, dense, and homogeneous state. From this initial state, it cooled and expanded to evolve into its present state. All (large-scale) structure and chemical elements that are present today emerge during this process.

The standard model of cosmology describes the physics that governs this transition. In this section I give a short overview over the *Lambda Cold Dark Matter* ($\Lambda$CDM) model, which is currently accepted as the standard model by a majority of the astrophysical community.

### 1.1.1 The Expansion of the Universe

In the $\Lambda$CDM model the Universe originates from a *Big Bang* from which it continues to expand to this day. This expansion is theoretically described by the Friedmann equations (Friedmann 1922). These are based on Einstein's general relativity theory

of gravitation and the cosmological principle. This principle states that the Universe is isotropic and homogeneous on large scales.

The Universe is believed to be predominantly made up of cold dark matter (CDM, 26 %), dark energy (69 %), and a much smaller contribution of a baryonic component (5 %, Planck Collaboration et al. 2016). Dark energy corresponds to a cosmological constant $\Lambda$. Hence, the name $\Lambda$CDM.

The expansion of the Universe has first been observationally established by Hubble (1929) who published the famous Hubble diagram and determined the value of the Hubble constant $H_0$, the current expansion rate of the Universe. This diagram shows that local galaxies recede from our Milky Way with a velocity that is proportional to their distance. More recently Riess et al. (1998) and Perlmutter et al. (1999) made the Nobel Prize winning discovery that the Universe's expansion is accelerating. They analyzed type Ia supernovae (SNe) and conclude that their data is consistent with a non-zero cosmological constant. This work marks the latest breakthrough that fundamentally changed our understanding of the cosmic expansion history. It establishes the existence of a non-zero $\Lambda$-term in the Friedmann equations through ruling out a matter dominated Universe (Frenk and White 2012, and references therein).

Mathematically the expansion of the Universe is described by distinguishing two measures of distance. The first is the comoving distance $x = |x_1 - x_2|$ between two fixed points, which does not change when the Universe expands. The second is the physical distance $r = |r_1 - r_2|$ between these points. They are related by the cosmological expansion factor $a$, which is a function of cosmic time $t$:

$$r(t) = a(t)x. \tag{1.1}$$

$a(t)$ is defined such that it is unity at present. Another fundamental cosmological quantity that is related to $a$ is the cosmological redshift $z$. The expansion of physical distance between fixed points in space causes the wavelength $\lambda$ of photons to grow with time as they propagate through space: $\lambda(t) = a(t)\lambda_0$. The redshift is defined as the relative difference in $\lambda$ between the time of its emission and its detection:

$$z := \frac{\lambda_0 - \lambda_e}{\lambda_e} = \frac{a_0 - a_e}{a_e} = a_e^{-1} - 1. \tag{1.2}$$

The subscripts 0 and e indicate the given quantity's value at present and the time of emission of the photon, respectively. The relative velocity of two objects (e. g. two galaxies) can be computed via differentiating equation (1.1):

$$\frac{dr}{dt} = x(t)\frac{da}{dt} + a(t)\frac{dx}{dt}. \tag{1.3}$$

The first term is due to the expansion of the Universe, usually referred to as the *Hubble flow*, and the latter is due to changes of the comoving position of the objects in question, referred to as *peculiar motion.*

According to its definition in equation (1.2), $z$ is a measure of the time at which the light that we observe was emitted. Hence, it is a measure of distance to that object. However, due to its direct and bijective mapping to the expansion factor it is also commonly used as a measure of cosmic time. It encodes the time at which objects emit light that would today be detected with the respective redshift.

## 1.1.2  The Early Universe

As stated above, the very early Universe is hot, dense and homogeneous. In the initial plasma, all forms of energy are in thermodynamic equilibrium. As it cools and expands, the individual components decouple from this plasma. The detailed history of these processes leaves observational signatures, such as the free-streaming scale of dark matter (DM) or the power spectrum of the cosmic microwave background (CMB). These signatures allow to place constraints on the expansion history of the Universe.

The first component to decouple from the primordial plasma is DM. The nature of DM remains unknown, since a prospective particle candidate has yet to be detected (Peter 2012). As of now, its nature can only be constrained by its effects on cosmology and galaxies. Current constraint suggest that it is made up of cold and heavy particles ($\gtrsim 10\,\text{keV}$) with non-relativistic velocities that only weakly interact with fundamental forces other than gravity (Bertone et al. 2004). For cosmological considerations, it is practical to assume that CDM only interacts gravitationally. Warm or hot candidates for the DM component can be ruled out, e. g. through observing the Lyman-$\alpha$ forest (e. g. Viel et al. 2013)[1]. The existence of DM is observationally motivated to reconcile observations on galactic (rotation curves, gravitational lensing, satellite velocity dispersion), galaxy cluster (galaxy velocity dispersion, gravitational lensing, Sunyaev-Zel'dovich effect) and cosmological scales (CMB anisotropies, Bertone et al. 2004 and references therein).

As the Universe further expands and dilutes, Big Bang nucleosynthesis starts to produce light elements. The predicted abundances of these elements agree very well with observations (Cyburt et al. 2016). The next step in the cooling Universe is the recombination of electrons and protons, which allowed photons to travel freely. These primordial photons comprise the CMB which can still be observed today. Its

---

[1]The Lyman-$\alpha$ forest is a feature with many absorption lines in the reshifted spectra of distant quasars.

discovery was awarded a Nobel Prize (Penzias and Wilson 1965).

### 1.1.3 Structure and Galaxy Formation

Once matter and radiation fully decoupled, the stage for structure and galaxy formation is set. The formation of structure in the Universe can only be understood by extending the ΛCDM model. This model assumes that the Universe is *perfectly* isotropic and homogeneous. This, however, is only true on very large spatial scales. To understand how matter condenses into compact structures, such as galaxies, galaxy clusters etc., cosmologists usually resort to initial quantum fluctuations and the theory of inflation. This theory states that in the first $\approx 10^{-35}$ s the Universe was rapidly expanding at an exponential rate. This rapid expansion "freezes in" potential quantum fluctuations that otherwise would annihilate (Dodelson 2003).

These initial anisotropies can be measured in the CMB, which had been the task of three satellite missions: the *Cosmic Background Explorer* (COBE), the *Wilkinson Microwave Anisotropy Probe* (WMAP), and the *Planck* mission. The latter is also the latest of these missions and provides the most accurate measurement of the initial anisotropies, or more precisely of the corresponding power spectrum, and of the expansion history of the Universe (Planck Collaboration et al. 2016).

In this physical context, structure forms through gravitational collapse of over-densities and hierarchical growth of collapsed objects. That means that small scale overdensities, which exceed a certain critical value, collapse first followed by the collapse of more massive structures. This process is highly non-linear. Unlike baryonic matter, DM has no pressure and collapses more efficiently than baryons. After collapse, these structures virialize and form a CDM halo. Pure DM simulations (i. e. effects of baryons are neglected) show that these have a universal radial density profile, the *Navarro-Frenk-White* (NFW) profile (Navarro, Frenk, and White 1997). Large collapsed objects are formed through frequent merging of small halos. This paradigm is dubbed the *hierarchical merging scenario* and is a direct prediction of the ΛCDM model (Mo et al. 2010). These DM halos are the scene of galaxy formation and are populated by luminous galaxies. How galaxies form in DM halos is the subject of section 1.5.

On large scales, galaxies and their host DM halos are arranged in clusters which are connected by filaments and sheets of DM halos, which also host galaxies. This structure is commonly called the *cosmic web*. It has been observed (Geller and Huchra 1989; Colless et al. 2001; York et al. 2000) and reproduced by simulations of cosmic structure formation, which only treat DM and ignore the effects of baryons (Springel et al. 2006; Frenk and White 2012).

Given its success in explaining numerous properties of the Universe on large

scales, the ΛCDM model is widely considered the best cosmological model (Naab and Ostriker 2016). Nevertheless, it faces some serious challenges on smaller, i. e. galactic and sub-galactic, scales. The central density profiles of DM halos and properties of satellite galaxy populations, as predicted by ΛCDM, seem to contradict observations (e. g. Moore 1994, 1999; Klypin et al. 1999; de Blok et al. 2001a,b; Swaters et al. 2003; Gentile et al. 2009; Boylan-Kolchin et al. 2011, 2012). The effects of baryonic physics (i. e. star formation (SF) and feedback) either solve these problems (e. g. Bullock et al. 2000; Macciò et al. 2010; Nickerson et al. 2011; Mashchenko et al. 2008; Governato et al. 2010; Macciò et al. 2012; Pontzen and Governato 2012; Di Cintio et al. 2013; Garrison-Kimmel et al. 2013) or at least seem very promising (e. g. Fattahi et al. 2016; Sawala et al. 2016; Dutton et al. 2016; Wetzel et al. 2016).

## 1.2  The Discovery of Galaxies

The idea that the Universe is populated by galaxies arose in the 18$^{th}$ and 19$^{th}$ century. Back then, astronomers like Charles Messier or William and John Herschel cataloged (Messier 1781; Herschel 1864) and studied extended celestial objects which they dubbed *nebulae*. However, William Herschel's theory of *island universes* proved to be inconsistent. He could not prove that the island universes were extragalactic (Longair 2006).

The issue remained unsolved well into the 20$^{th}$ century. The question of whether the *spiral* nebulae were extragalactic or part of the Milky Way was the subject of the *Great Debate* between Harlow Shapley and Heber D. Curtis in 1920. The solution was provided five years later by Edwin Hubble who identified 35 Cepheid stars in the Triangulum Galaxy (M33) and the Andromeda nebula (M31). He used the period-luminosity relation (Leavitt and Pickering 1912) to determine the absolute magnitude of these stars. With this information he could determine their distance and was able to prove that these objects had distances much larger than any estimate of the Galaxy's size (Hubble 1925, 1926a). The extragalactic nature of spiral nebulae was proven.

## 1.3  Galaxies as Cosmological Probes

The existence of galaxies and many of their properties are well established scientific facts. We have seen that the fate of galaxies and that of the Universe are tightly connected. Many (statistical) properties of galaxies and the galaxy population depend strongly on the underlying cosmological model. Any cosmological theory has to be

able to reproduce these. Thus, galaxies serve as probes to test cosmological models.

The morphology and other properties such as the star formation rate and efficiency, etc. may be determined by processes external as well as internal to the galaxy and its host halo. The former strongly depend on the underlying cosmological model of the Universe. The latter, often called *secular processes*, do not and, thus, they do not need to be explained by a cosmological model. In this thesis, I present models that possibly explain certain features of observed spiral galaxy morphology via secular dynamics, namely the radial density profiles of stellar disks in spiral galaxies.

The central subject of this thesis is the physics and stellar dynamics of disk galaxies. In order to understand the results and implications of the studies presented here, it is crucial to know about the properties of galaxies. Therefore, the following sections give a short review on galaxies in general and on disk galaxies and their stellar dynamics in more detail. Much of this is based on two excellent books by Houjun Mo, Frank van den Bosch, and Simon White (Mo et al. 2010) as well as James Binney and Scott Tremaine (Binney and Tremaine 2008) and a selection of great review papers (van der Kruit and Freeman 2011; Sellwood 2014; Somerville and Davé 2015).

## 1.4  Classification of Galaxies

### 1.4.1  Catalogs of Galaxies

Nebulae have been observed and recorded in catalogs in the 18$^{th}$ and 19$^{th}$ century. The most famous of these catalogs are the *Messier* catalog by Charles Messier (Messier 1781) and the *New General Catalogue of Nebulae and Clusters of Stars* (NGC) and its two supplementary *Index Catalogues* published by John Dreyer (Dreyer 1888, 1895, 1910). The objects in these catalogs are not limited to galaxies but also contain real nebulae or globular clusters. The 104 objects from the final Messier catalog are named M1 to M104. The NGC lists 7840 objects and the Index Catalogues add another 5386 objects to the list. Together with its Index Catalogues, the NGC contains all Messier objects. The listed objects are named according to their number in these catalogs, e. g. the Andromeda galaxy is usually referred to as M31, its NGC name is NGC 224.

### 1.4.2  The Hubble Sequence

In 1926, Hubble published his classification scheme for extragalctic nebulae (Hubble 1926b) which is still used for a qualitative classification of galaxies. The famous Hubble tuning-fork diagram (Figure 1.1), a graphical representation of Hubble's classification scheme for extragalactic nebulae, was first published considerably later in 1936
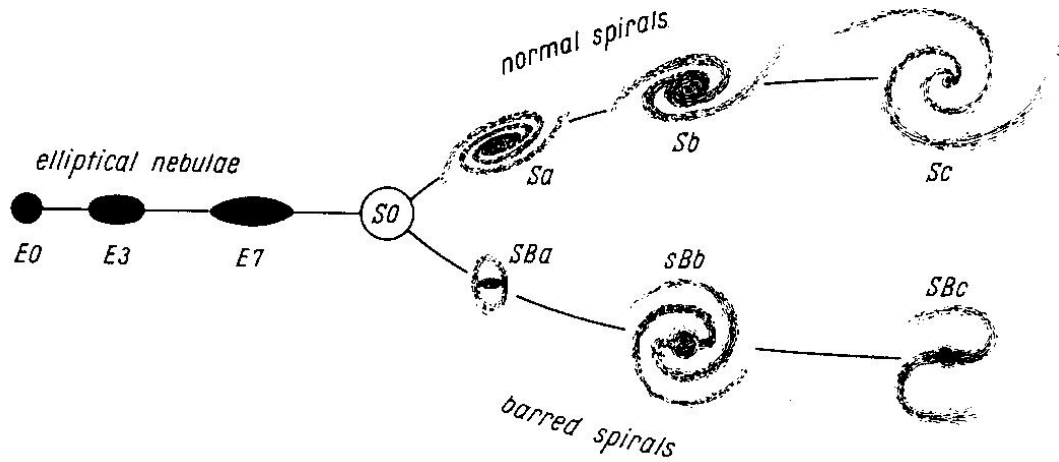
**Figure 1.1:** Hubble's famous tuning-fork diagram for the classification of galaxies as first published in Hubble (1936).

(Hubble 1936). He divided extragalactic nebulae into two main classes: *ellipticals* and *spirals*. Hubble dubbed the former *early*- and the latter *late*-type nebulae.

The elliptical nebulae are sequenced from spherical (E0) to very elongated (E7) where the corresponding number indicates the nebula's ellipticity. Nebulae with ellipticities exceeding a value of 7 were classified as spirals. Hubble decided that the ellipticities of spirals are not suited for a more refined classification. He used structural properties for further classification instead. They are divided into normal (S) and barred spirals (SB). For spirals, the sequence of ellipticities is replaced by three criteria:

1. the size of the unresolved central region,

2. the degree of winding of the spiral arms and

3. the degree of resolution in the arms.

Nebulae with a large central nucleus and tightly coiled arms are denoted by the letter *a* and considered to be the natural extension of the sequence of ellipticals. Hubble dubbed these *early*-type spirals. The sequence continues with *intermediate*-type (*b*) and finishes with *late*-type (*c*) spirals which have unwound spiral arms and a small nucleus. The terms *early, intermediate*, and *late* refer to the position in the sequence.[2]

---

[2]The term *early-type spiral* must not be confused with *early-type galaxy*. It is merely a sub-classification of spiral or late-type galaxies. The term early-type galaxy refers to elliptical galaxies (see above).

The intermediate stage between elliptical and spiral nebulae are disk-like galaxies without any visible spiral structure. They are called *lenticular* (S0). All galaxies that do not fit any of these classes of regular nebulae are classified as *irregular* nebulae (I).

Until the early 20th century the term *nebulae* was used to refer to all extended objects on the sky in general, including galaxies. Today, the term is reserved for interstellar gas clouds and the term *galaxy* refers to extended DM-dominated objects that host stars.

Hubble explicitly pointed out that his classification scheme is "descriptive and entirely independent of any theory" but also mentioned that it is "almost identical" to the theoretical evolutionary sequence derived by Jeans (1919), i. e. elliptical galaxies evolve from left to right in the Hubble sequence eventually turning into late-type spirals. Presently, this interpretation is believed to be untrue (e. g., Mo et al. 2010, see also section 1.5.2). However, the nomenclature of early- (ellipticals, left in the sequence) and late-type (spirals, right) galaxies has persisted until the present day. Due to their shape, spiral galaxies are often also referred to as disk galaxies. Throughout this thesis I use the terms early-type and elliptical galaxy, as well as late-type, spiral, and disk galaxy interchangeably.

### 1.4.3 Further Classification Criteria

The Hubble sequence classifies galaxies based on their apparent morphology. However, galaxies show a much more diverse set of different properties such as their total luminosity, their surface brightness, their photometric color, their gas content, their current star formation activity, and whether or not they have active galactic nuclei (AGN). Many of these classification criteria correlate with their morphological Hubble type. Generally, early-type galaxies are more massive/luminous, have lower gas content, and are photometrically redder than late-type galaxies (Mo et al. 2010, and references therein).

### 1.4.4 Describing the Population of Galaxies

A directly observable property of the galaxy population is the galaxy luminosity function $\phi(L)$. It describes the spatial density of galaxies of a given luminosity $L$. This function depends on the photometric filter band used for the observations and on many other factors such as the morphological type, the color, the redshift, or the environment of the galaxy. In combination with population synthesis models and the respective spectroscopic and multi-band photometric data, a galaxy stellar mass function $\phi(M_\star)$ can be constructed (Mo et al. 2010). Recently, stellar masses of

galaxies have been estimated via fitting their spectral energy distribution (Somerville and Davé 2015).

Comparing the stellar mass function to the halo mass function $\phi(M_{\mathrm{halo}})$ allows to determine the star formation efficiency in galaxies as a function of halo or galaxy stellar mass. This is usually achieved with the abundance matching technique (e. g., Moster et al. 2010, 2013; Behroozi et al. 2013; Hudson et al. 2015), where the most luminous galaxy is mapped to the most massive one and so on. These studies consistently show that star formation in galaxies is very inefficient and that its peak is at a halo mass of $M_{\mathrm{halo}} = 10^{11.6}\,\mathrm{M_{\odot}}$ at $z = 0$ where the galaxies stellar mass fraction is ≈25 % of the cosmic baryon fraction (Moster et al. 2013).

This raises the question of why star formation in galaxies is so inefficient. An equivalent question is: What stops the gas to efficiently condense in DM halos and what keeps it from cooling and forming stars once it has settled in the center of these halos? This has been termed the *overcooling problem.* To solve this problem, we have to consider two different regimes. For host halos with a mass of $M_{\mathrm{halo}} \lesssim 10^{12}\,\mathrm{M_{\odot}}$ many studies show that energetic feedback from massive stars and SNe may heat, ionize and/or expel the cool and dense gas. With a combination of these consequences of SN feedback realistic disk galaxies can be produced in state-of-the-art simulations. Disk galaxies populate the respective mass regime up to $10^{12}\,\mathrm{M_{\odot}}$, but not exclusively (Somerville and Davé 2015).

For larger halo masses these mechanisms are not effective any more and the overcooling problem cannot be resolved by stellar and SN feedback. In this mass regime, the star formation is believed to be suppressed by feedback from AGN (Somerville and Davé 2015).

Additionally, the number of star forming galaxies does not evolve with redshift while the number of quiescent galaxies is growing. This indicates that all galaxies shut off their star formation at some point in their evolution (Somerville and Davé 2015, and references therein).

Observations show that galaxies obey a number of tight scaling relations. These are correlations with small scatter between global properties of galaxies such as the luminosity and the rotational velocity of disk galaxies (Tully and Fisher 1977) or velocity dispersion (Faber and Jackson 1976) and size (Kormendy 1977) of elliptical galaxies. These are the famous Tully-Fisher, Faber-Jackson, and Kormendy relations. The latter two are projections of the fundamental plane for ellipticals. Other relations that scale with the galaxies' stellar mass are the star forming main sequence (Noeske et al. 2007; Wuyts et al. 2011), the fraction of cold gas (Baldry et al. 2008; Peeples and Shankar 2011), and the metallicity of gas or stars (mass-metallicity relation, Tremonti et al. 2004; Gallazzi et al. 2005; Zahid et al. 2013).

Most of these relations can be (qualitatively) reproduced by models of galaxy

formation. The quantitative values for the slope and normalization of all scaling relations remain difficult to be modeled simultaneously. For more information see the review by Somerville and Davé (2015).

## 1.5 The Formation of Galaxies

In this section, I review the literature which describes how galaxies form in DM halos.

The current paradigm of galaxy formation was first described by White and Rees (1978). While the collapsing DM halos virialize via violent relaxation (Lynden-Bell 1967), the gas in the collapsing region is shock-heated to the virial temperature $T_{\mathrm{vir}}$ of the collapsed halo. $T_{\mathrm{vir}}$ generally increases with halo mass and is usually $>10^4$ K. At these temperatures, gas is usually ionized and thus may cool radiatively through bremsstrahlung, recombination, and line emission from states excited through collisions[3]. This cooling is only effective in halos with gas masses up to $10^{12}$ M$_\odot$ (Mo et al. 2010) or total masses up to $10^{13}$ M$_\odot$ (White and Rees 1978), which potentially explains the large amount of hot gas in massive collapsed structures such as groups and clusters of galaxies (Mo et al. 2010). Gas that cools, condenses and falls to the center of DM halos where it reaches densities and temperatures that allow it to fragment and form stars (White and Rees 1978). For temperatures below $10^4$ K, radiative cooling is very inefficient. Hence, in very low-mass halos the gas cannot cool and condense and we do not expect these halos to host a galaxy. This sets a lower bound on the population of halos hosting a luminous galaxy. Low-mass galaxies may merge with others to form more massive systems. When they fall into a larger galaxy they may survive and thus quite naturally explain the abundance of satellite galaxies.

Another challenge for galaxy formation models is to reproduce the entire galaxy population along the Hubble sequence, i. e. rotationally supported disk galaxies and dispersion supported elliptical galaxies. A key question is under which conditions spiral and elliptical galaxies emerge. Theorists have made tremendous progress in this field in the past decades.

### 1.5.1 Spiral Galaxies

Spiral galaxies are thought to form from gas, which was accreted from the host halo and cold streams that feed this halo. This gas cools and settles into a rotationally supported disk at the center of the host halo where it forms the stars that comprise

---

[3]Line emission is usually only efficient for heavy elements in gas, which has previously been enriched with metals.

the galaxy. The star formation process is thought to be governed by the Kennicutt-Schmidt relation (Kennicutt 1989, 1998). This star formation law states that the star formation rate surface density $\Sigma_{\mathrm{SFR}}$ is related to the gas surface density $\Sigma_{\mathrm{gas}}$ via a power law. The initial studies of Kennicutt (Kennicutt 1989, 1998) are based on global values for $\Sigma_{\mathrm{SFR}}$ and $\Sigma_{\mathrm{gas}}$. More recent studies (e. g., Bigiel et al. 2008) extended this result by studying the relation on spatially resolved scales. Bigiel et al. (2008) found that below a threshold value of $\Sigma_{\mathrm{gas}} \approx 9\,\mathrm{M}_\odot\,\mathrm{pc}^{-2}$ star formation is drastically reduced. Many models and simulations of galaxy formation implement this star formation law (e. g., Stinson et al. 2006; Dutton 2009; Stinson et al. 2013; Vogelsberger et al. 2014a; Wang et al. 2015). However, they usually transfer the relation to volume densities.

The general paradigm of disk galaxy formation relies on the conservation of the specific angular momentum distribution of gas, which is inherited from the host DM halo (e. g., Fall and Efstathiou 1980; Mo et al. 1998). Roškar et al. (2008a) found that the star forming region of a spiral galaxy grows outward over time. This results from the construction of their simulations in which high specific angular momentum gas takes more time to cool and thus settles in the disk at later times. However, this scenario is believed to be generally true (Larson 1976; van der Kruit and Freeman 2011). As the radius at which gas settles in the disk increases with increasing specific angular momentum, larger radii get populated with gas at later times. According to the Kennicutt-Schmidt law this causes the star formation to spread to larger radii with time. This scenario is dubbed *inside-out growth* of galaxy disks.

The assumption of conservation of the specific-angular momentum distribution alone produces disks, which have a central mass excess that is in tension with observations. Energetic (and ejective) stellar feedback also helps to reduce this contradiction (e. g., Dutton 2009). It preferentially removes low angular momentum gas from the center of the disk which may torque up in the halo and accrete back onto the disk with higher specific angular momentum (Brook et al. 2012; Übler et al. 2014). This mechanism is called the *galactic fountain*.

Stellar feedback has another consequence that advanced the understanding of galaxy formation. It slows down or halts the depletion of interstellar gas in galaxies by regulating star formation. Therefore, it keeps the galaxies gas rich. This is important because dry (i. e. gas-free or gas-poor) mergers are known to efficiently dissipate angular momentum and produce elliptical objects (see also section 1.5.2).

I conclude that stellar feedback is a key process in the theory of spiral galaxy formation, given its success in resolving tensions between models and observations. The physical details of stellar feedback and its implementation in (semi-)analytical and numerical modeling is beyond the scope of this thesis. The structure and evolution of stellar disks in spiral galaxies is the subject of section 1.6.

An ubiquitous feature of disk galaxies is that their rotational velocity is constant

with galactocentric radius over a large region of their stellar disk. These flat rotation curves of galaxies present some of the strongest evidence for dark matter (see reviews by van der Kruit and Allen 1978; Faber and Gallagher 1979; Roberts 2008). Reproducing them has been a major challenge in the theory of disk galaxy formation. Until about a decade ago numerical simulations had failed to achieve this goal (see section 1.6.3).

## 1.5.2 Elliptical Galaxies

Toomre (1977) showed that merging of two disk galaxies of similar mass (major mergers) may significantly reduce the total angular momentum of the system. Many subsequent studies have confirmed this and showed that dispersion dominated spherical objects can be formed this way. Minor mergers (mass ratio $\lesssim 1 : 10$) were found to play a key role in the formation of ellipticals because they can dynamically heat a stellar disk in the vertical direction (see section 4.2.2 in Somerville and Davé 2015, and references therein).

Recently, this simple merger scenario for the origin of elliptical galaxies was proven to be incomplete. Hydrodynamic simulations of gas-rich mergers of spiral galaxies showed that disks may either survive or resettle in the remnant galaxy. Further gas accretion may even reform a disk around an elliptical merger remnant. Consequently, the formation picture has been altered. Observations show that the bulk of the stellar population of ellipticals formed at least 8-10 Gyr ago ($2 \lesssim z \lesssim 4$). This leads to the assumption that their progenitors have their gas reservoir depleted or removed before that time. A possible culprit to achieve this is AGN feedback.

An alternative scenario of spheroid formation is through violent disk instabilities. These disk instabilities then form dense clumps, which form stars and migrate to the center where they contribute to the formation of a bulge component (Elmegreen et al. 2008; Dekel et al. 2009; Bournaud et al. 2011). It is still under debate whether disk instabilities contribute significantly to spheroid formation (Somerville and Davé 2015). Another internal process that is capable of moving substantial amounts of gas into the center is the formation of a central bar. In the center this gas can potentially fuel a central black hole or a growing bulge (Somerville and Davé 2015, and references therein).

The formation scenarios for spirals and ellipticals suggest that the elliptical population is more massive and luminous than spiral galaxies. This naturally follows because they originate from merging of spiral galaxies. They predominantly populate DM halos with masses $\gtrsim 10^{12}\,M_\odot$ while halos of lower mass host most spiral galaxies (Somerville and Davé 2015).
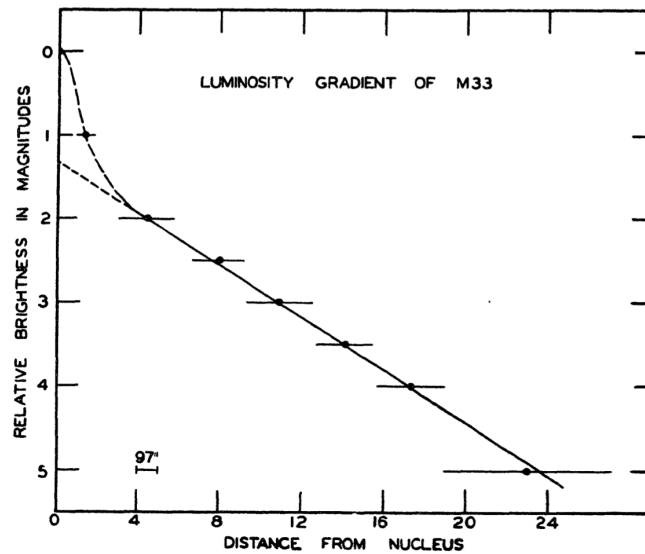
**Figure 1.2:** The mean surface brightness profile of M33. Shown is the original figure from Patterson (1940). It is the first reported observation that shows surface brightness profiles consistent with an exponential light distribution.

## 1.6 The Disks of Spiral Galaxies

Having reviewed the current paradigm of the formation of galaxies, I now focus on the structural properties and evolution of stellar disks in spiral galaxies as these are the subject of the studies presented in this thesis. Namely, these are the radial surface density profiles of stellar disks and the current understanding about their formation. Many aspects of their formation are still poorly understood and the research of this work aims to advance our understanding of the shape of stellar disks.

### 1.6.1 Exponential Disks

De Vaucouleurs (1959) summarized findings of several observational studies (e. g., Patterson 1940; van Houten et al. 1954). He found that the smoothed luminosity distribution of spiral galaxies can be well approximated by a central spherical bulge, which is surrounded by a flat component. This outer flat component has an approximately exponential radial luminosity distribution. Such an exponential profile was first recorded in M33 by Patterson (1940). Her original data are shown in figure 1.2.

Freeman (1970) states that almost every disk-like galaxy has a near-exponential surface brightness profile and established it as the most general feature of late-type

galaxies. He found that all disks share a common central *B*-band surface brightness of $\mu_B(0) \approx 21.65$ mag arcsec$^2$ for the extrapolation of the flat exponential component. The discovery of low surface brightness galaxies (LSB) has lead to a redefinition of this law to be an upper limit (Allen and Shu 1979; Bosma and Freeman 1993; de Jong 1996).

Exponential profiles also arise quite naturally in numerical simulations of disk galaxy formation in completely isolated halos (Steinmetz and Muller 1995; Roškar et al. 2008a,b, 2012; Minchev et al. 2012; Elmegreen and Struck 2013; Herpich et al. 2015a; Berrier and Sellwood 2015; Herpich et al. 2015b) and galaxies forming in a cosmological context (Katz 1992; Navarro and White 1994; Sommer-Larsen et al. 1999, 2003; Governato et al. 2004; Robertson et al. 2004; Okamoto et al. 2005; Governato et al. 2007; Guedes et al. 2011; Stinson et al. 2013). Berrier and Sellwood (2015) showed that any local feature in the radial profile of stellar disks is erased by spiral activity (see also section 1.7). They find that the disks approach a smooth and near-exponential profile within a few orbital times. Any of their attempts to produce a lasting feature failed. They conclude that spiral activity will eventually turn any unrealistic disk configuration into a smooth and realistic profile, and thus contributes to the formation of exponential profiles. The work of Berrier and Sellwood (2015) potentially explains why many of the simulated disks with near-exponential profiles have birth configurations, which are far from being exponential (Debattista et al. 2006; Roškar et al. 2008a, 2012; Minchev et al. 2012; Herpich et al. 2015a,b).

The stellar mass to light ratio $Y = M_\star/L$ is observed to be constant (Gerssen et al. 1997, 2000) in the *K*-band where $M_\star$ is the stellar mass and $L$ is the luminosity. Hence, based on the results of Freeman (1970), the radial mass distribution is expected to follow an exponential surface density profile $\Sigma_\star(R)$:

$$\Sigma_\star(R) = \Sigma_0 \exp(-R/R_\mathrm{d}) \tag{1.4}$$

with the disk scale length $R_\mathrm{d}$ and central surface density $\Sigma_0$. The vertical mass distribution of disks is often approximated by an exponential function as well. The exponential scale height $h_z$ is observed to be independent of galactocentric radius $R$ (van der Kruit and Searle 1981a,b, 1982), which allows for the three-dimensional stellar mass-density distribution of disks to be separated:

$$\rho_\star(R,z) \propto \Sigma_\star(R) \exp\left(-|z|/h_z\right). \tag{1.5}$$

## 1.6.2 Disk Truncations and Breaks

Deeper observations of edge-on spiral galaxies revealed a radial cutoff at a few radial disk scale lengths (van der Kruit 1979; van der Kruit and Searle 1981a,b). As

the sensitivity of observations had increased and, due to the increased accuracy of photometric results with the help of charge coupled devices (CCDs), this result could qualitatively be confirmed by Pohlen et al. (2002). The profiles are best described by a continuous two-component exponential profile with a well defined break radius (Pohlen et al. 2002). However, they found significantly shallower outer profiles (scale lengths of ≈2 kpc) than van der Kruit and Searle (1981a, <1 kpc). The studies modify the picture of exponential disk profiles not to hold out to arbitrary radii.

A number of studies tried to establish a correlation between the position of the break and the scale length of the exponential profile in edge-on (van der Kruit and Searle 1981a,b; Barteldrees and Dettmar 1994; Pohlen et al. 2000; de Grijs et al. 2001; Pohlen et al. 2001; Kregel et al. 2002) and face-on (van der Kruit 1988; Pohlen et al. 2002) observations. They found the position of the breaks (truncations) to be roughly at three to five times the exponential scale length. However, there is significant scatter within and among each of the studies.

Erwin et al. (2005) found breaks in the radial profile of barred disk galaxies with the opposite behavior. Outside the break, the profile continues with a shallower slope than inside.

The cases described above comprise the three main classes of disk profiles:

**Type-I:** purely exponential profiles

**Type-II:** truncated or down-bending profiles

**Type-III:** anti-truncated or up-bending profiles.

A more refined classification scheme for Type-II and Type-III profiles exists. For Type-II disks this states whether or not the break occurs inside the end of a possible central bar. If it is outside of a bar, there is a further distinction between classical truncations of the disk and breaks related to an outer Lindblad resonance (OLR, see section 1.7). Type-III disks can be further distinguished by the morphology of the outer regions. If it is similar to that of the inner disk, it is considered to be part of the disk (Type-III-d). If the outer isophotes are rounder, they are usually attributed to a spheroidal component that is not part of the disk (Type-III-s). For the purpose of this thesis we are generally concerned about the classical truncations for Type-II disks. These also make up the vast majority of observed Type-II disks (Gutiérrez et al. 2011). Type-III-s disks are rare in spiral galaxies (Maltby et al. 2012b) but their contribution increases up to 50 % in S0 galaxies (Maltby et al. 2015).

The exact demographics of disk-break types are still under debate, in particular their dependence on the cosmological environment of the galaxies. It is quite certain that they vary with morphological type (Pohlen and Trujillo 2006; Erwin et al. 2008;
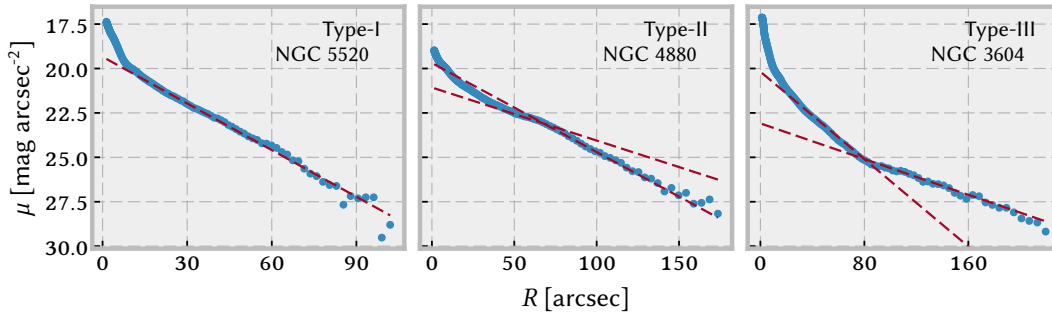
**Figure 1.3:** The three panels show *R*-band surface brightness profiles of prototypical galaxies for the three main profile types: purely exponential (Type-I, left panel), truncated profiles (Type-II, middle), and anti-truncated profiles (Type-III, right). The data are taken from Gutiérrez et al. (2011), which are available online. Overplotted are the fit results for the respective components from Gutiérrez et al. (2011).

Gutiérrez et al. 2011; Maltby et al. 2012a, 2015). Type-II disks are most frequent among late-type spiral galaxies (80 %) and rather rare among S0 galaxies (25 % Gutiérrez et al. 2011). Comparing the abundance of Type-II among spiral and S0 galaxies, Maltby et al. (2012b, 2015) qualitatively confirm this trend with morphological type. The frequency of Type-III disks shows a weaker dependence. Most galaxy samples reported in the literature show that Type-I disks are rather rare (<25 %).

None of the above studies find a significant dependence of the break type on environment. Head et al. (2015) also find no dependence of galaxy structure on their cluster-centric radius for cluster galaxy and state that most broken disks are found in barred galaxies despite a low bar fraction in their overall sample. Contrary, Erwin et al. (2012) find that no S0 galaxy in the Virgo cluster has a Type-II disk break while the three break types are found to be roughly equally distributed among S0 galaxies in the field. The difference in the Virgo cluster is almost entirely compensated for by Type-I disks. Recent work by Clarke et al. (2017) explains this difference by a transformation of a Type-II disk to a Type-I disk in a simulated S0 galaxy via tidally induced spiral activity. Roediger et al. (2012) find a qualitatively similar trend among spiral galaxies. The global frequency of Type-II breaks is reduced in cluster environments in favor of an enhanced population of Type-I disks. For disk galaxies in clusters they find all three types to be roughly equally abundant. The outer disks of Type-III galaxies are found to depend on the tidal interaction strength (Laine et al. 2014).

### 1.6.3 Disk Formation Theories

Eggen, Lynden-Bell, and Sandage (1962) were the first to conclude that the Milky

Way must have formed from a collapsed gas cloud. Due to conservation of angular momentum the gas settles in a thin disk that is in centrifugal equilibrium, e. g. its own rotation balances gravity. The bulk of the stars in the Galaxy have formed from this settled disk. The oldest stars show more eccentric orbits, which are less co-planar than younger stars. Hence, they may have formed before the gas disk was fully settled. Sandage, Freeman, and Stokes (1970) extend this picture to all disk galaxies and find that the morphological type of a galaxy is determined by the gas dynamics at the final stages of its initial collapse and their primordial angular momentum distribution. Mestel (1963) considers the above scenario and, additionally, requires detailed angular momentum conservation of individual gas particles to derive his famous *Mestel disk* which allows for a flat rotation curve. Freeman (1970) notes that a self-gravitating exponential disk with a flat rotation curve has an angular momentum distribution that is very similar to that of a uniformly rotating sphere with a uniform mass distribution. All of these studies do not yet account for the existence of DM halos.

Fall and Efstathiou (1980) apply this mechanism to the collapse of gas in a DM halo. In addition to the conservation of the angular momentum distribution, they assume that the normalized angular momentum distribution of the disk material is inherited from that of the halo. Their model reproduces the observed flat rotation curves of spiral galaxies. Gunn (1982) shows that these assumptions yield approximately exponential disks. Additionally, van der Kruit (1987) predicts radial cutoffs at 4.5 scale lengths. Dalcanton et al. (1997) use the same basic picture to explain the population of low- and high-surface brightness galaxies. They propose that the observed limit of central surface brightnesses (see section 1.6.1) is related to disk instabilities which impose a natural upper limit on central disk mass. Their model also naturally gives rise to exponential surface density profiles and flat rotation curves. Dalcanton et al. (1997) and Mo et al. (1998) establish that the scale length of galactic disks is positively correlated with the host halo's angular momentum and negatively correlated with the disk mass fraction. Hence, disks with low mass and high angular momentum are expected to form extended LSB galaxies.

Numerical simulations initially failed to produce realistic disks due to spurious numerical angular momentum loss (Navarro and Benz 1991; Navarro and White 1994; Navarro and Steinmetz 1997, 2000). The gas particles transfer a large fraction of their angular momentum to the DM halo via dynamical friction. This problem could be solved with very high numerical resolution (Kaufmann et al. 2007; Mayer et al. 2008).

All the studies mentioned above have in common that they reproduce (near-)exponential disks as a reflection of the initial angular momentum distribution, i. e. as a consequence of the initial conditions of galaxy formation. However, more recent numerical results suggest that exponential disks may form from any initial configuration

(see section 1.5.1).

Lin and Pringle (1987) provide the first model to explain exponential disks, which does not rely on initial conditions. They find that viscosity in a star forming gaseous galactic disk cause the resulting surface density profile to be exponential—provided that the time scale of star formation is comparable to the viscous time scale. A better analytic understanding of these processes is provided by Yoshii and Sommer-Larsen (1989) who also show that the assumption of equal time scales for star formation and viscosity can be slightly relaxed. Ferguson and Clarke (2001) extend the model to include the effects of cosmological accretion.

More recent attempts to explain the production of exponential profiles are based on stellar scattering off of transient clumpy perturbations. In simple simulations (Elmegreen and Struck 2013) and an analytical description (Struck and Elmegreen 2017) of these processes, exponential profiles arise naturally and for certain subsets of the available parameter space broken profiles are produced. A stochastic description of scattering processes produces near-exponential profiles given that scattering is biased towards the galactocentric direction (Elmegreen and Struck 2016).

The formation of broken-exponential disk profiles has received some attention in simulations. While the inside-out formation scenario or star formation thresholds (see section 1.5.1) provide natural explanations for sharp cutoffs in the radial profiles they may not explain the continued steeper exponential profiles outside the breaks in Type-II disk profiles. These were reproduced in the numerical simulations of Roškar et al. (2008a). They show that the position of the break is set through the maximum angular momentum of cooled gas, which is consistent with the picture of inside-out growth. They find that the outer exponential part of the profile is populated with stars that formed on near-circular orbits inside of the break region and moved outward via radial migration. During this migration process they maintain their orbital circularity. I describe the mechanism of radial migration in more detail in section 1.7.2.

A consequence of the mechanism proposed by Roškar et al. (2008a) is that the disk outskirts are populated by predominantly old stars, which had a lot of time to migrate large distances. In their simulations this manifests as "U-shaped" age profiles. The minima of these age profiles spatially coincide with the break. The existence of such age profiles has been confirmed by observed color profiles (Azzollini et al. 2008; Bakos et al. 2008), spectroscopic observations of NGC 6155 (Yoachim et al. 2010), and by resolved stellar populations (Radburn-Smith et al. 2012). Recent work by Ruiz-Lara et al. (2015) found that positive age gradients in galaxy outskirts are not unique to Type-II discs. They claim that these age profiles are not linked to Type-II profiles but do not rule out stellar migration as a possible mechanism to populate the regions beyond the disc break.

An alternative explanation is provided by Minchev et al. (2012). They find that

the break in Type-II disks is associated to extensive radial redistribution by multiple co-existing spiral or bar perturbations of different multiplicities. A qualitatively similar claim has been made before by Debattista et al. (2006) and (Foyle et al. 2008). When they add gas-accretion to their simulations, Minchev et al. (2012) find that Type-III profiles form with large stellar velocity dispersion beyond the disk break. Other explanations of Type-III disk profiles rely on tidal forces mediated through external factors like mergers or fly-bys (Younger et al. 2007; Kazantzidis et al. 2009; Roediger et al. 2012; Borlaff et al. 2014).

### 1.6.4 Disk Instabilities, Spirals and Bars

As implied by their name, an ubiquitous feature of spiral galaxies is spiral structure and many disks also have a central bar. While bars have an azimuthal multiplicity of $m = 2$ spirals may in general take any positive non-zero integer value for $m$. Both types are non-axisymmetric structures that rotate with a global angular pattern speed. The pattern speed may change with time. The origin of these structures, in particular spiral structure, is not yet fully understood. In this section, I review our current understanding of the formation of these features, which is based mostly on the review paper by Sellwood (2014).

Stellar disks are self-gravitating objects, and hence subject to gravitational instabilities. Toomre (1964) derived his famous local stability criterion for axisymmetric instabilities:

$$Q \equiv \frac{\sigma_R \kappa}{3.36 G \Sigma} > 1 \tag{1.6}$$

where $\sigma_R$ is the radial velocity dispersion, $G$ is Newton's gravitational constant, $\Sigma$ is the mass surface density and $\kappa$ is the epicycle frequency, i. e. the frequency at which a particle, which is radially displaced from a circular orbit, will oscillate about its home radius. This criterion does not apply to non-axisymmetric perturbations for which no stability criterion is known (Sellwood 2014).

Goldreich and Lynden-Bell (1965) and Julian and Toomre (1966) described the process of *swing amplification*, which describes the amplification of initial non-axisymmetric perturbations in stellar disks. These perturbations play a vital role in theories of spiral and bar formation.

Disks may also be globally unstable. In the linear regime these instabilities manifest themselves as two-armed spiral modes that vanish in the outer disk. In the inner disk they are usually absorbed by the inner Lindblad resonance (ILR see section 1.7 for a definition). However, for $m = 2$ modes and central potentials that give rise to linearly rising rotation curves the perturbation may never encounter the ILR and it straightens to form a bar when the perturbation becomes non-linear. Bars may also

be formed through gradually self-reinforced trapping of non-circular orbits in the center. This process may play an important role for the formation of tidally triggered bar formation (Sellwood 2014, and references therein).

Spirals are gravitationally driven density waves in the stellar disk. Simulations show that they are usually rather short lived and disperse within a few rotational periods of the host disk. Spectral analysis showed that very quickly changing spiral patterns may be caused by the superposition of multiple underlying waves that exist on larger time scales (e. g., Grand et al. 2012; Minchev et al. 2012; Roškar et al. 2012). Moreover, the spiral patterns have a constant shape and rotate at a constant angular rate. Once formed, the spiral features are transported radially until they get absorbed at the inner and outer Lindblad resonances (Lynden-Bell and Kalnajs 1972). These interactions with the Lindblad resonance trigger new instabilities that lead to subsequent spiral patterns (Sellwood 2012; D'Onghia et al. 2013).

Prerequisites for spiral triggering instabilities are the presence of shear in the disk and a dynamically cool disk, i. e. low radial velocity dispersion, as required by Toomre's stability criterion (equation (1.6)). As we will see in the following section spiral activity gradually heats a stellar disk and prevents the formation of subsequent spirals. Hence, for sustained recurring spiral activity of a stellar disk it must stay dynamically cool. A possible source of dynamically cool disk material are young stars that form from the settled gas disk. As gas is pressurized, it generally orbits with very small global velocity dispersion. These dynamical properties are inherited by the stars that are formed. As long as there is ongoing star formation, spiral activity can be sustained (Sellwood and Carlberg 1984). This is also a plausible explanation for the lack of spiral features in S0 galaxies that are usually gas depleted, contrary to the rich structures in the gas rich spiral galaxies (Sellwood 2014).

## 1.7 Radial Mixing in Disks

### 1.7.1 Non-Axisymmetric Perturbations and their Resonances

Bars and spiral structure have profound effects on the dynamics of stellar disks. They are non-axisymmetric time-dependent perturbations in the mass distribution and consequently cause perturbations of the galactic potential, which have similar properties. These give rise to substantial radial mixing. Recent numerical work suggests that this radial mixing process is responsible for smoothing rotation curves and radial mass distributions and may be a key driver of the formation of exponential disks (Sellwood 2014, and references therein). In this section I describe the physics that govern stellar dynamics in such potentials.
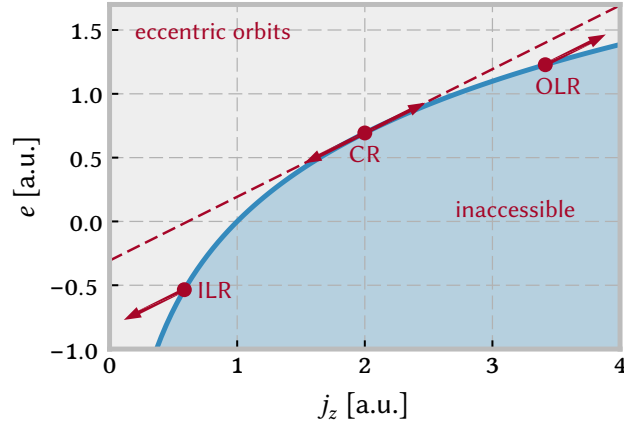
**Figure 1.4:** A classical Lindblad diagram for a flat rotation curve. It illustrates the orbit evolution in a spherical potential, perturbed by a rotating non-axisymmetric $m = 2$ mode with pattern speed $\Omega_p$. The solid blue line indicates the locus of circular orbits. Orbits below that curve are impossible. The distance of orbits from this curve is a measure of the radial action $J_R$. The red dashed line is the tangent to the circular orbit curve at the CR. Its slope is $\Omega_p$. The resonances (CR, ILR, OLR) are indicated by red dots along with possible evolutionary trajectories of resonant orbits (arrows).

A key quantity for studying the dynamical effects in non-axisymmetric potentials, which rotate with a pattern speed $\Omega_p$, is the Jacobi integral $e_J$ of particle orbits:

$$e_J = e - \Omega_p j_z \tag{1.7}$$

where $e$ and $j_z$ are the total specific energy and the $z$-component of the specific angular momentum vector of the orbit, respectively. $e_J$ is an integral of motion in rotating potential, and hence it is constant ($de_J/dt = 0$, Binney and Tremaine 2008). For a perturbation with constant $\Omega_p$, it immediately follows that any change in $e$ is proportional to the change in $j_z$ (Binney and Tremaine 2008):

$$\Delta e = \Omega_p \Delta j_z. \tag{1.8}$$

This confines the trajectories in the Lindblad plane ($e$-$j_z$) to lines with a slope of $\Omega_p$, which is illustrated in figure 1.4. This follows from the relation $de/dj_z = \Omega(J_z)$, which is valid for circular orbits.

The radial action $J_R$, which is a measure of radial kinetic energy, obeys

$$\Delta J_R/m_\star = \frac{\Omega_p - \Omega}{\omega_R} \Delta j_z, \tag{1.9}$$

where $\Omega$ and $\omega_R$ are the azimuthal and radial frequency of the affected orbit, respectively, and $m_\star$ is the mass of that particle (Sellwood and Binney 2002). For near-circular orbits $\omega_R$ is the epicycle frequency $\kappa$. The relation (1.9) immediately implies that $J_R$ does not change to first order if $\Omega = \Omega_p$. This is the *corotation resonance* (CR). Resonances also occur when the frequency $m(\Omega_p - \Omega)$, at which a particle with angular frequency $\Omega$ experiences the perturbation, is in phase with the radial frequency $\omega_R$. These are the inner ($\Omega > \Omega_p$) and outer ($\Omega < \Omega_p$) Lindblad resonances. At these resonances

$$\Delta J_R / m_\star = \mp \frac{1}{m} \Delta j_z \tag{1.10}$$

where the upper and lower sign apply to the ILR and OLR respectively. Therefore, particles at Lindblad resonances do experience a change in radial action. We further have $\Delta j_z < 0$ and the ILR and $\Delta j_z > 0$ at the OLR (Lynden-Bell and Kalnajs 1972). Hence $\Delta J_R$ increases at both resonances. This can also be seen in figure 1.4.

Note that for any realistic galaxy potential, the angular frequency of circular orbits decreases monotonically with radius. This allows for all these resonances of any perturbing mode with $\Omega_p$ to be mapped to a specific radial position in the disk.

## 1.7.2 Radial Migration

Stellar orbits do not experience any enduring changes when they are not in any of the resonances (Lynden-Bell and Kalnajs 1972). In their seminal paper, Sellwood and Binney (2002) find that changes in the angular momentum of stellar particles, which are in CR with transient spiral modes, dominate over those of particles in Lindblad resonances. Additionally, they find that particles on near-circular orbits are more likely to experience substantial changes in their orbital angular momentum than those on eccentric orbits. As a result, they find that changes in angular momentum of particles in a stellar disk are dominated by near-circular orbits that are in CR with a succession of transient spiral modes. Due to the lack of radial heating, they stay on near-circular orbits.

This mechanism is dubbed *radial migration* or *churning* (Schönrich and Binney 2009; Sellwood 2014). I use the two terms interchangeably throughout this thesis to describe changes in stellar angular momentum of orbits in CR with rotating potential perturbations.

Radial migration can cause stars to migrate over very large distances across the disk. At the same time, they retain their circularity as radial heating at the CR is negligible (equation (1.9)). Churning is found to be effective in many subsequent studies (e. g., Roškar et al. 2008a, 2012; Solway et al. 2012). Solway et al. (2012) also find that the efficiency is larger for thin disks and does not increase vertical motions.
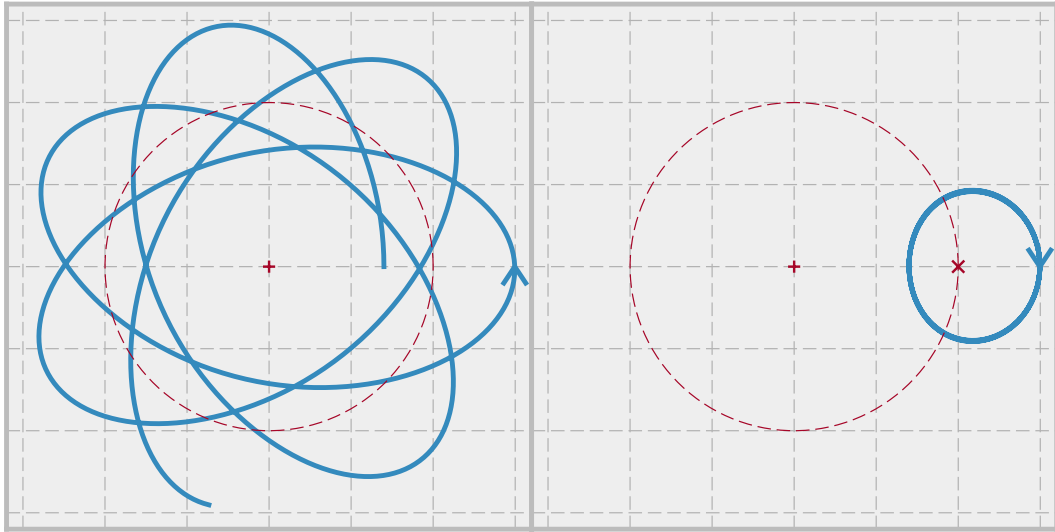
**Figure 1.5:** The left panel shows an eccentric orbit in a static axisymmetric potential (blue). The right panel shows the same orbit in a frame corotating with the orbit's guiding center (red cross). This is a closed orbit around the star's guiding center and illustrates the decomposition of a stellar orbit into a circularly rotating guiding center (dashed red line) and an epicycle (blue line) which does not need to be circular. The sense of rotation in the respective frame is indicated by the blue arrow.

Nevertheless, there is some amount of radial heating at the Lindblad resonances (equation (1.10)) but stars, which are affected by these resonances, do not experience a comparable amount of angular momentum evolution, and hence do not migrate as far (Sellwood and Binney 2002).

In order to illustrate the different effects of radial migration and heating of orbits it is useful to consider the concept of an orbit's guiding center. In general an orbit in steady axisymmetric potentials is a rosette. It can be decomposed into a circular motion of a guiding center and an epicycle orbit. In the corotating frame, that epicycle orbit rotates about the guiding center in a retrograde sense. It is generally not circular but is elliptic for near-circular orbits. This decomposition is illustrated in figure 1.5. Radial migration changes the radius of the guiding center rotation. Depending on the sign of the change in angular momentum, experienced at the CR, it will decrease (−) or increase (+). To first order, no energy is added to the epicycle motion. Heating, on the other hand, does not only change the guiding center radius but adds energy to the epicycle motion. Hence, the orbits gain in eccentricity. This is what happens at Lindblad resonances. Stars that already are on eccentric orbits may also cool at Lindblad resonances.

If a perturbing spiral mode was permanent, stars could be *trapped* at the respective

CR. These stars' guiding center radii perform oscillations about the radius of the CR. They are precisely those stars, which experience the largest changes in guiding center radius for a specific perturbation. However, they periodically return to their initial orbit. Hence, for lasting changes to the orbits to occur, the perturbation has to be transient and its duration must be of order of about half the oscillation period of the trapped stars' guiding center radii (Sellwood and Binney 2002). Spiral perturbations that form in numerical simulations usually meet these criteria (Sellwood and Binney 2002; Roškar et al. 2012).

If there are no extreme gradients in the radial mass distribution the amount of stars that move from inside the radius of the CR of a single perturbation to the outside is approximately balanced by the amount of stars moving the opposite direction. As a result the global radial mass distribution remains unchanged (Sellwood and Binney 2002). Moreover, radial migration preserves the global angular momentum of a stellar disk (Sellwood 2014).

Stars that are in CR with a succession of transient spiral perturbations experience a random walk of their guiding center radius. The step size may be as large as 2 kpc (Sellwood 2014). As a result, stars in a disk with frequent spiral activity may migrate very efficiently in the radial direction without being dynamically heated (e. g., Sellwood and Binney 2002; Roškar et al. 2012).

The inside-out formation model of disk galaxies (see section 1.5.1) predicts rather strong radial age and chemical abundance gradients in galactic disks. The process of radial migration weakens these gradients (Sellwood and Binney 2002) and sometimes even reverses them locally (Roškar et al. 2008a). Radial migration is a mechanism that is capable of reproducing observed radial gradients in disks (Roškar et al. 2008a; Schönrich and Binney 2009; Minchev et al. 2013).

As of now, evidence for and against radial migration have been reported from studies of the Milky Way stellar disk (section III.C.5 in Sellwood 2014, and references therein). Recent studies strongly support the presence of radial migration. At given radii in the Milky Way, the dispersion of the radial [Fe/H] profile increases with the age of the stars (Genovali et al. 2014; Ness et al. 2016). Sellwood and Binney (2002) argue in favor of radial mixing on the basis of the existence of very low metallicity (compared to Solar) molecular clouds in the Solar neighborhood. In the Sc galaxy GC6754, Sánchez-Menguiano et al. (2016) find azimuthal variations in chemical abundances along the spiral arms. These are consistent with the predictions of the imprint of large-scale radial migration (Di Matteo et al. 2013; Grand et al. 2015, 2016; Baba et al. 2016).

### 1.7.3 Bar-Induced Radial Mixing

Bars are known to cause considerable radial mixing (Hohl 1971). Unlike radial migration, bar-induced mixing dynamically heats stars (Hohl 1971) and gas (Friedli et al. 1994). Hohl (1971) also found that a bar has a strong effect on the radial mass distribution.

When the OLR of a bar and the CR of a spiral perturbation overlap, the affected orbits evolve in a non-linear or chaotic manner (Quillen 2003). The resulting radial redistribution may be even more efficient than with churning (Minchev and Famaey 2010; Minchev et al. 2011). Bars have also been linked to the formation of outer rings (Romero-Gómez et al. 2006, 2007; Athanassoula et al. 2009) indicating that they can drive radial redistribution. However, the formation of outer rings is generally believed to be caused by gas that is driven to the OLR by bars (Mo et al. 2010).

## 1.8 Scope of this Thesis

In this thesis, I present a suite of numerical simulations of isolated galaxies without any external cosmological influences which reproduce the three observed types of radial disk profiles (fully exponential, truncated and antitruncated). The type of disk profile that emerges depends on the amount of low-angular momentum gas that is present in the disk as I show in chapter 2. This work was peer reviewed and published (Herpich et al. 2015a).

Owing to the fact that there is no evidence that the formation of Type-II disks in these simulations is inconsistent with the mechanism found by Roškar et al. (2008a, see section 1.6.3), I turn to a more detailed analysis of one of the simulations that formed a Type-III break. These results are presented in chapter 3 and show that such breaks may be a signature of the formation of a strong bar. The corresponding paper is still in the peer-reviewing process but the initial draft is already available as a preprint (Herpich et al. 2015b).

Based on the assumption that radial migration is very efficient in galactic disks we developed an analytical model for radial disk profiles through maximizing a suitably defined entropy in angular momentum space. Hence, this model does not resort to a reflection of the initial conditions of galaxy formation but rather on the secular evolution of galactic disks. The resulting profiles are near-exponential, and hence provide a potential explanation for the ubiquitous observations of exponential disk profiles (Freeman 1970). Testing this model against observed data gives fair agreement, testing against simulations gives very good agreement. This work was also peer reviewed and was accepted for publication recently (Herpich et al. 2017).

I conclude this thesis by briefly reviewing my results and relating the individual projects to each other. Then I discuss their implications for the theory of galaxy formation and cosmology. Finally, I identify open issues and lay out potential follow-up studies.

# 2 Radial Breaks in Disk Profiles and Halo Spin

This chapter has been published in a peer reviewed journal (Herpich et al. 2015a). I am first author of that paper and have written it myself. All of the presented research has been conducted by me. Additionally, I present an analysis of another suite of simulations which add to the interpretation of the results in the paper (section 2.2.2). I also describe more details on the initial conditions of the simulations than in the paper (section 2.1.2).

The subject of this chapter is the relation between the initial conditions of galaxy formation and the formation of breaks in the radial surface density profiles of stellar disks (see section 1.6.2). It is explored by means of numerical hydrodynamic simulations of isolated galaxy formation.[1] This allows for the physics of these simulations to be unambiguously interpreted as secular. However, the angular momentum distribution in the initial conditions is cosmologically motivated.

## 2.1 The Simulations

### 2.1.1 The Simulation Code CHaNGa

The simulations are carried out with a modified version of the publicly available treeSPH code CHaNGa (Jetley et al. 2008, 2010; Menon et al. 2014)[2]. They are evolved for 8 Gyr. This corresponds to the time between $z \sim 1.5$, when the last major merger era was coming to an end (Zentner and Bullock 2003), and $z = 0$. Examinations of cosmological simulations show that they behave similarly to isolated spheres after their last major merger (Zentner and Bullock 2003).

The CHaNGa code is derived from the treeSPH code GASOLINE (Wadsley et al. 2004). It uses a modified version of SPH which employs a pressure averaged force

---

[1]In this thesis the term *isolated galaxy* refers to a simulated galaxy that is in total isolation, i. e. without any cosmological context. It does not refer to isolated galaxies in the sense of field galaxies without recent interactions with other galaxies.

[2]Available at `http://www-hpcc.astro.washington.edu/tools/changa.html`

calculation (Ritchie and Thomas 2001; Hopkins 2013; Keller et al. 2014). CʜᴀNGᴀ includes stochastic star formation (Stinson et al. 2006, $c_\star = 0.1$) based on a Kennicutt-Schmidt law (Kennicutt 1998), radiative metal line cooling (Shen et al. 2010), metal diffusion, and pre-supernova stellar wind feedback (early stellar feedback, Stinson et al. 2013). The feedback follows Dalla Vecchia and Schaye (2012) in which the energy output from supernova explosions of a stellar population is released at one time all together. The energy released per supernova is $E_{SN} = 1.0 \times 10^{51}$ erg. First tests of this implementation produced realistic disk galaxies in cosmological simulations in the mass range I consider here (Keller et al. 2015, 2016).

As CʜᴀNGᴀ is a SPH code, it is Lagrangian and follows the evolution of a set of particles, i. e. their 6-dimensional phase-space coordinates, their mass and in the case of gas particles their temperature $T$ and metallicity $Z$.

## 2.1.2 The Initial Conditions Code ᴘʏICs

I begin this section with a short note on the adopted notation for radii in this thesis. I refer to the galactocentric radius in spherical symmetry with a lower-case $r$. The distance to the rotational axis in cylindrical coordinates is denoted by an upper-case $R$.

The initial conditions for the simulations were created using the publicly available open-source initial conditions code ᴘʏICs[3]. I wrote this code specifically for the simulations in this thesis. The resulting initial conditions are very similar to those used by Roškar et al. (e. g. 2008a). It creates completely isolated (i. e. not cosmological) spherical halos of DM and gas. The gas in the initial halo rotates about the $z$-axis obeying a given angular momentum distribution. The DM and the gas are in dynamical and hydrostatic equilibrium, respectively. In this section, I give a brief introduction to the code and present the parameters used for the initial conditions of the simulated suite of galaxies in section 2.1.3.

The ᴘʏICs code can realize arbitrarily defined radial density profiles of the halo and angular momentum distributions. Here I introduce its default profiles, which I used for the simulations carried out for this thesis.

The default density profile $\rho(r)$ for the DM halos in ᴘʏICs is the $\alpha\beta\gamma$-profile (Hernquist 1990)[4] with an exponential cutoff outside the virial radius $R_{200}$ following Springel and White (1999) and Kazantzidis et al. (2004) for otherwise diverging mass profiles

---

[3]Available at `https://github.com/jakobherpich/pyICs`

[4]The parametrization in the original paper differs slightly from the one commonly used and implemented in the code.

(i. e. when $\beta \leq 3$):

$$\rho(r) \propto \begin{cases} x^{-\gamma}(1 + x^{\alpha})^{-(\beta-\gamma)/\alpha} & \text{if } x < c \text{ or } \beta > 3 \\ \exp\left[-\frac{x-c}{fc}\right]\left(\frac{x}{c}\right)^{\epsilon} c^{-\gamma}(1 + c^{\alpha})^{-(\beta-\gamma)/\alpha)} & \text{if } x \geq c \text{ and } \beta \leq 3 \end{cases} \qquad (2.1)$$

with the rescaled radius $x = r/R_s$, the scale radius $R_s$, and the halo concentration parameter $c = R_{200}/R_s$. $f$ sets the scale of the cutoff and $\epsilon = -\frac{\gamma+\beta c^{\alpha}}{1+c^{\alpha}} + \frac{1}{f}$. The virial radius $R_{200}$ is defined to be the radius at which the mean density of the halo drops below 200 times the critical density of the universe. The initial density profile of the DM $\rho_d$ and the gas $\rho_g$ are identical to a normalization factor: $\rho(r) = \left(f_{bary}\right)^{-1} \rho_g(r) = \left(1 - f_{bary}\right)^{-1} \rho_d(r)$ where $0 < f_{bary} < 1$ is the fraction of baryons in the initial halo. The velocities of the DM particles obey the ergodic equilibrium distribution function $f(E)$ of spherical (i. e. non-rotating) systems following the procedure of Kazantzidis et al. (2004), which is described in detail in section 4.3 of Binney and Tremaine (2008). $E$ is the relative energy as defined in equation (4.41) of Binney and Tremaine (2008). PYICS calculates $f(E)$ for a given halo density profiles $\rho(r)$ and draws particle positions directly from the cumulative mass distribution and velocities from this distribution function via rejection sampling. The optimal interpolation intervals for sampling the distribution function were taken from an initial conditions code (Kazantzidis et al. 2004), which was kindly provided by Stelios Kazantzidis.

The velocities of gas particles are calculated in cylindrical coordinates $(v_R, v_{\varphi}, v_z)$. While the collisionless DM particles are supported against gravity through their velocity dispersion, gas is pressure supported. Therefore, the velocities of the macroscopic gas particles in SPH simulations have no velocity dispersion and I set the radial and vertical components to $v_R = v_z = 0$, since gas particles are initialized to rotate about the $z$-axis. Their tangential velocities $v_{\varphi}$ are a function of $R$ and are determined through their specific angular momentum $j$ which is also a function of $R$ only: $v_{\varphi}(R, \varphi, z) = v_{\varphi}(R) = j(R)/R$. The radial angular momentum profile $j(R)$ is constructed such that it obeys any given mass distribution of $M(< j)$ and monotonically increases with $R$. The default specific angular momentum distribution of the halo in PYICS obeys the two parameter function, which Bullock et al. (2001) found for DM halos in cosmological simulations:

$$\frac{M(< j)}{M_{200}} = \mu\frac{j/j_{max}(\lambda, \mu)}{j/j_{max}(\lambda, \mu) + \mu - 1}. \qquad (2.2)$$

$M(< j)$ is the mass of all material, which has less angular momentum than $j$, $\mu$ is the shape parameter and $j_{max}$ is the maximum specific angular momentum in the halo.

$j_{max}$ depends on the value of $\mu$ and is proportional to the spin parameter $\lambda$, which is defined as in Bullock et al. (2001):

$$\lambda = \left.\frac{J}{\sqrt{2}MVR}\right|_{R=R_{200}}.$$

(2.3)

Here $J$ and $M$ are the halo angular momentum and mass inside a sphere of radius $R$ and $V = \sqrt{GM_{200}/R_{200}}$ is the halo circular velocity at that radius. The exact definition of $j_{max}$ is given in equations (9) and (10) in Bullock et al. (2001). Its exact value is not needed for the creation of initial conditions because it only scales the angular momenta, and hence the rotational velocities of the gas particles in the initial conditions. The correct scaling of the gas velocities is applied at the end of initial conditions creation to yield the desired spin parameter of the halo.

In the initial conditions, the DM particles do not have any net rotation. They obey the equilibrium distribution function of a non-rotating spherical halo because implementing the distribution function of a rotating sphere is not straightforward (Binney and Tremaine 2008). $\lambda$ is, however, calculated under the assumption that the DM and the gas halo share the same spatial angular momentum distribution. The specific angular momentum distribution of the gas $M_{gas}(< j)$ then obeys $M_{gas}(< j) = f_{bary}M(< j)$.

Figure 2.1 shows the effects of changing $\lambda$ and $\mu$ on the initial angular momentum distribution of the gas. $\lambda$ changes the normalization and $\mu$ the functional form. Lower values for either parameter cause the amount of low-angular momentum gas to increase (see also Bullock et al. 2001).

The pressure $P$ of the gas particles obey the equation of hydrostatic equilibrium.

$$\nabla P(r) = -\rho_g(r)\nabla\Phi(r) = -f_{bary}\rho(r)\nabla\Phi(r)$$

(2.4)

where $\Phi$ is the gravitational potential. Poisson's equation links $\Phi$ to the global density profile $\rho(r)$ of gas and DM combined. Thus, $P(r)$ is fully determined by $\rho(r)$ and $f_{bary}$. PyICs computes it numerically by integrating Poisson's equation and equation (2.4).

Based on the hydrostatic pressure profile the temperature of each gas particle can be calculated. This equilibrium temperature is calculated iteratively because the mean molecular weight depends on the ionization state of the gas and, thus, on its temperature. The ionization state is approximated using the Saha equation. The code considers all possible ionization states of hydrogen and helium. This is a good approximation to primordial gas because big bang nucleosynthesis predicts primordial lithium abundances to be several orders of magnitude lower (Cyburt et al. 2016). The part of the code, which calculates the temperature of the gas particles, is
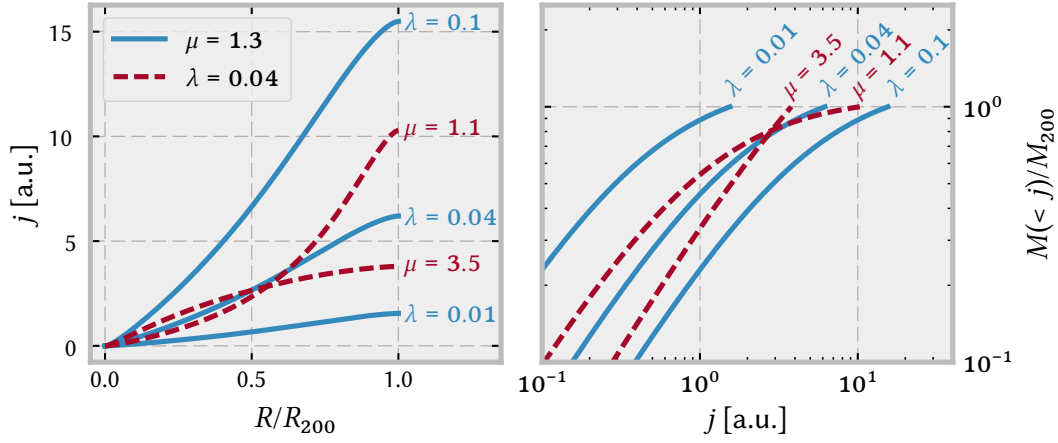
**Figure 2.1:** The initial angular momentum profiles as a function of radius (left panel) and its cumulative distribution (right) for a selection of values for $\lambda$ and $\mu$. The density profile of the halo is an NFW profile with $c = 10$. The solid lines show the effect of different spin parameters $\lambda$ and constant shape parameter. It simply sets the normalization of the radial angular momentum profile. The dashed lines show the effect of different shape parameters $\mu$. The functional form looks significantly different for different values of $\mu$. The right panel shows that lowering $\lambda$ or $\mu$ increases the amount of low-angular momentum material.

based on a script provided by Rok Roŝkar. I improved the iteration algorithm of this script to prevent it from getting stuck in infinite loops.

The resulting initial conditions files hold the following information on the initial halo: the mass and the 6-dimensional Cartesian phase-space coordinates of all (DM and gas) particles and the temperature and metallicity of the gas particles. The initial metallicity is set to $Z = 0$ which mimics unenriched primordial gas. These quantities encode all information that is needed for the simulation code CHaNGa (see section 2.1.1) to evolve the halo. All other intermediate quantities (e. g. $P$) are discarded.

The pyICs code depends on the PYTHON Nbody analysis code PYNBODY (Pontzen et al. 2013) because it employs the PYNBODY functionality of creating, modifying and saving simulation snapshot files.

## 2.1.3 Initial Conditions

For the simulations the only parameters that I vary are $\lambda$ and $\mu$. All other parameters are identical for every simulation and take the following values. The density of the halos follow an NFW profile (Navarro, Frenk, and White 1997), i. e. $(\alpha, \beta, \gamma) = (1, 3, 1)$ (equation (2.1)), with a virial mass of $M_{200} = 10^{12}\,\mathrm{M_\odot}$ which corresponds to a virial

**Table 2.1:** Overview of all simulations and their properties. $\lambda$ is the initial spin parameter, $\mu$ the shape parameter of the angular momentum distribution, $M_{\mathrm{gas}}$ and $M_\star$ are the amount of gas and stars in the disk region ($R < 30\,\mathrm{kpc}, |z| < 3\,\mathrm{kpc}$) at $8\,\mathrm{Gyr}$.

| $\lambda$ | $\mu$ | $M_{\mathrm{gas}}$ $(10^{10}\,M_\odot)$ | $M_\star$ $(10^{10}\,M_\odot)$ |
|---|---|---|---|
| 0.02 | 1.3 | 0.34 | 3.14 |
| 0.03 | 1.3 | 0.56 | 2.91 |
| 0.035 | 1.3 | 0.67 | 2.64 |
| 0.04 | 1.3 | 0.95 | 2.53 |
| 0.045 | 1.3 | 1.13 | 2.42 |
| 0.05 | 1.3 | 1.24 | 2.36 |
| 0.055 | 1.3 | 1.31 | 2.30 |
| 0.06 | 1.3 | 1.34 | 2.25 |
| 0.1 | 1.3 | 1.44 | 1.96 |
| 0.04 | 1.04 | 0.13 | 3.20 |
| 0.04 | 1.9 | 1.18 | 2.36 |
| 0.04 | 3.5 | 1.38 | 2.24 |

radius of $R_{200} = 206\,\mathrm{kpc}$ for the adopted value of $h = 0.7$ for the Hubble constant.[5] The halo concentration is $c = 10$ and the cutoff scale $f = 0.1$. The full simulation file hosts a total of $10^6$ DM and $10^6$ gas particles. The mass resolution of the DM and gas particles is $m_{\mathrm{DM}} = 1.09 \cdot 10^6\,M_\odot$ and $m_{\mathrm{gas}} = 1.21 \cdot 10^5\,M_\odot$ respectively. This corresponds to a baryon fraction of $f_{\mathrm{bary}} = 0.1$. This value is significantly smaller than the cosmic baryon fraction ($\approx 0.16$ Planck Collaboration et al. 2016) and reflects the fact that the first stars may remove significant portions of gas from the shallow potential wells of early DM halos. The gravitational softening length is $\epsilon = 227\,\mathrm{pc}$. The SPH smoothing length is variable and set such that the smoothing kernel covers 50 particles.

Two different suites of simulations are considered for this thesis. They are summarized in table 2.1. First, the shape parameter is held constant at $\mu = 1.3$ and the initial halo spin $\lambda$ is varied and vice-versa for the second suite ($\lambda \equiv 0.04$). The fixed values for either of the suites are typical for DM halos in cosmological simulations (Bullock et al. 2001).

---

[5] $H_0 = 100\,h\,\mathrm{km\,s^{-1}\,Mpc^{-1}}$

## 2.2 The Formation of Breaks in the Radial Surface Density Profile

### 2.2.1 The Effect of the Initial Halo Spin

Here I present the results for the first suite with fixed shape parameter $\mu = 1.3$. These results have been published and peer-reviewed (Herpich et al. 2015a).

Figure 2.2 shows mock observational images of the simulated galaxies. There is a strong trend from red and compact galaxies at low initial spin to extended blue galaxies at high spin. The edge-on projections show that all simulated galaxies are disk-like with a thin young disk (blue) and a rather thick old disk (red).

I am now interested in the surface density profiles of these simulated galaxies. After evolving the simulations for 8 Gyr, I extract the stellar surface density $\Sigma_\star(R)$ in 60 axisymmetric radial bins. These stellar surface density profiles include all star particles up to 3 kpc above and below the plane and inside a cylinder with a radius of 30 kpc. The errors on the stellar surface density are approximated to be Poissonian: $\delta\Sigma_\star = \Sigma_\star/\sqrt{N}$ where $N$ is the number of star particles in the respective radial bin.

I model the surface density profiles with a superposition of a "broken-exponential disk" $\Sigma_d$ surrounding an exponential bulge, which is a very good parametrization of the data (see Figure 2.3):

$$\Sigma_\star(R) = \Sigma_k \exp\left(-\frac{R}{R_k}\right) + \Sigma_d(R) \tag{2.5}$$

where

$$\Sigma_d(R) = \Sigma_0 \times \begin{cases} \exp\left(-\frac{R}{R_i}\right) & \text{if } R < R_b \\ \exp\left(-\frac{R_b}{R_i}\right)\exp\left(-\frac{R-R_b}{R_o}\right) & \text{else.} \end{cases} \tag{2.6}$$

Here $\Sigma_k$ and $\Sigma_0$ are normalization factors for the bulge and disk component respectively. $R_i$ and $R_o$ represent the inner and outer disk scale length, $R_k$ the scale length of the bulge component, and $R_b$ the radius of the break. The posterior probability distribution function (PDF) of the fit parameters for the given surface density profiles is obtained via Bayesian inference using the Monte Carlo Markov Chain (MCMC) algorithm EMCEE (Foreman-Mackey et al. 2013)[6]. With this algorithm, 2000 samples are drawn from the posterior PDF $p(\theta|\{R_n; \Sigma_{\star,n}; \delta\Sigma_{\star,n}\})$ of the model parameters $\theta$ given the data $\{R_n, \Sigma_{\star,n}, \delta\Sigma_{\star,n}\}$. The likelihood function is constructed following a

---

[6]A standard $\chi^2$ minimization procedure is not used because it gives unstable results.
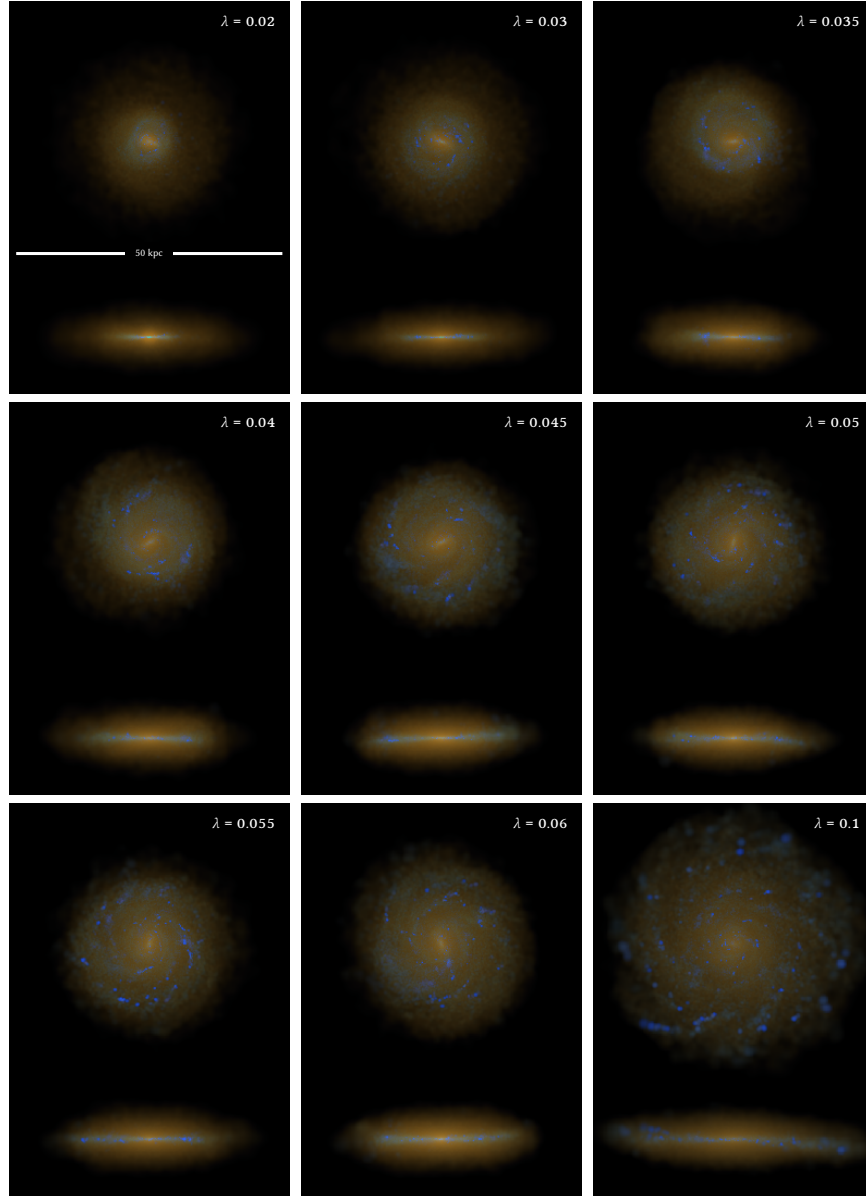
**Figure 2.2:** Mock observational images of the simulated galaxies with constant $\mu = 1.3$. The image shows face-on and edge-on images of all simulated galaxies from low spin ($\lambda = 0.02$) in the top left to high spin ($\lambda = 0.1$) in the bottom right. Each panel is $50\,\mathrm{kpc}$ across. These are multiband images generated via the stellar population synthesis models implemented in the PYNBODY code (Pontzen et al. 2013) and do not consider galactic extinction. They are based on the models by Marigo et al. (2008) and Girardi et al. (2010). The $i$, $v$ and $u$-bands are shown in red, green and blue colors, respectively. The low-spin galaxies are compact and red but they do have a young (blue) disk component which is clearly visible in the edge-on view. The edge-on views also reveal an old (red) massive central bulge for the lowest-spin simulations. As the initial spin increases the galaxies get more and more radially extended and less centrally concentrated. All galaxies with $\lambda > 0.04$ show signs of spiral structure in the blue components. In all cases the disks are rather thick. This figure is a modified version of figure 1 from Herpich et al. (2015b).
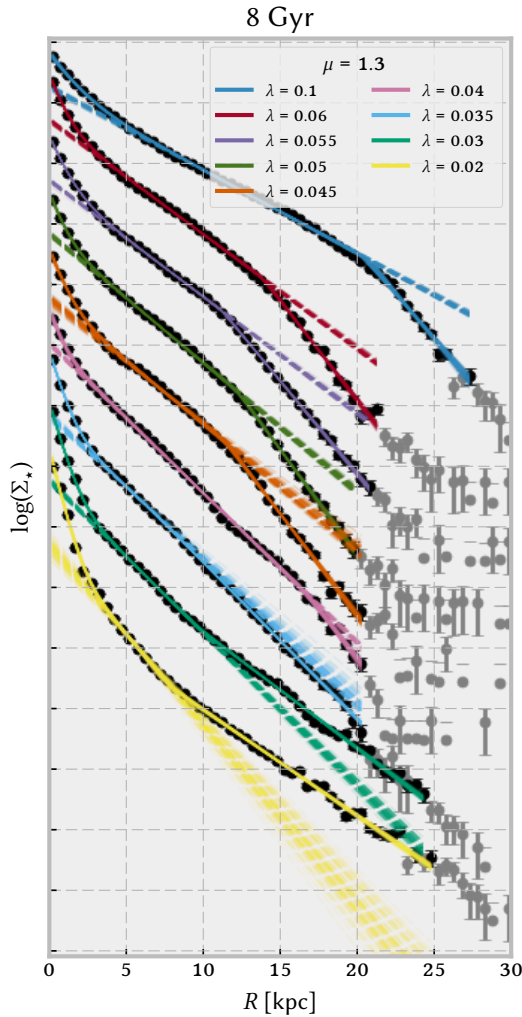
**Figure 2.3:** The radial stellar surface density profiles. Presented are the stellar surface density as a function of axisymmetric radius of the individual halos at $t = 8\,\mathrm{Gyr}$ (black points). The errors are estimated as Poisson noise. The individual profiles are offset by one dex (i. e. one tick mark) each for clarity as I am not interested in the normalization. The gray data points correspond to radial bins with $\leq 9$ particles, which were ignored in the parameter estimation. The colored lines show the model for 100 parameter sets drawn from the posterior PDF. The dashed lines are an extrapolation of the inner exponential part ($\Sigma_0 \exp(-R/R_\mathrm{i})$) to make the break in the profile more easily visible. The figure qualitatively shows that there is a trend from Type-III disks for galaxies in low spin halos to Type-II disks in high spin halos.

tutorial in the EMCEE user guide.[7] I use an uninformed (i. e. flat) prior PDF with very conservative limits on the available parameter space.

Figure 2.3 shows the stellar surface density profiles (black points) for all simulations at 8 Gyr overplotted by 100 models sampled from the obtained posterior PDF (colored lines). The gray data points show data for radial bins with 9 or fewer star particles. These points are omitted in the calculation of the likelihood function.

Figure 2.3 shows that the type of the disk profiles change with $\lambda$. In the lowest-spin simulations ($\lambda \leq 0.03$) the profile is antitruncated (Type-III), i. e. $R_\mathrm{o} > R_\mathrm{i}$. The models with high spin parameters ($\lambda \geq 0.045$) clearly show a truncated break (Type-II). At

---

[7] http://dan.iel.fm/emcee/current/user/line/
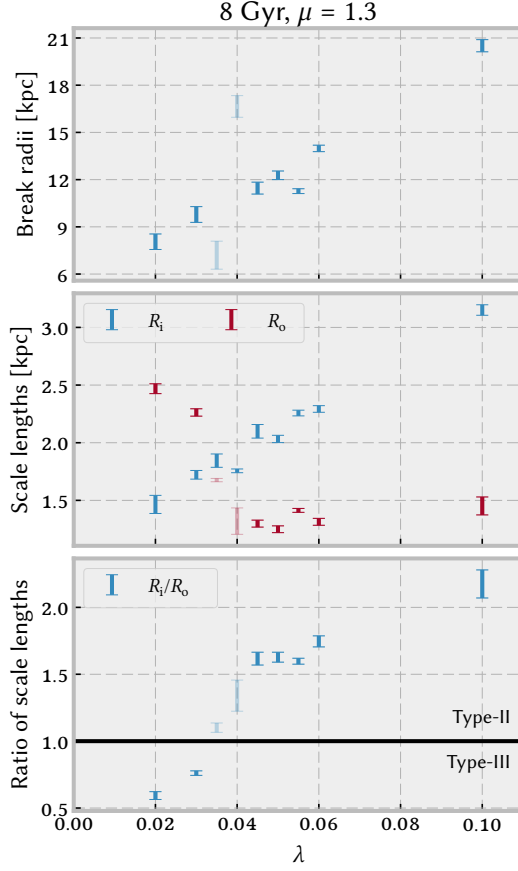
**Figure 2.4:** Systematic variation of the parameters for the broken-exponential disk profile (equation (2.6)) as a function of $\lambda$. The top panel shows the break radii. The estimates of some parameters for $\lambda = 0.035, 0.04$ are plotted fainter since they are somewhat ill-defined in these cases (see text). The middle panel shows the estimated inner (blue) and outer (red) scale lengths. The bottom panel shows the ratio of the inner and outer scale lengths. The horizontal line indicates unity, that is the separation between the up- (Type-III, below the line) and down-bending regime (Type-II, above) and the locus of perfectly exponential (Type-I) profiles. The errorbars indicate the range between the 16-th and the 84-th percentile. The figure shows a clear trend from Type-III to Type-II profiles as $\lambda$ increases and a transition (Type-I) at $\lambda \approx 0.035$.

intermediate spin ($\lambda \approx 0.035$), the profiles are almost completely exponential (Type-I).

Figure 2.4 quantifies these trends in terms of the fit parameters. The middle panel shows the fitted inner (blue) and outer (red) scale lengths as a function of $\lambda$. The inner scale length $R_i$ increases linearly with $\lambda$. The outer scale length $R_o$ has its maximum at low $\lambda$ and decreases as $\lambda$ increases until it approaches a constant lower value for $\lambda \gtrsim 0.04$. The bottom panel of figure 2.4 shows the ratios of the inner and outer scale lengths $R_i/R_o$ as a function of $\lambda$. There is a transition from Type-III ($R_i/R_o < 1$) to Type-II ($R_i/R_o > 1$) disk breaks at $\lambda \approx 0.035$.

The top panel in figure 2.4 shows the estimated break radii $R_b$ as a function of $\lambda$. Except for the $\lambda = 0.035, 0.04$ cases, $R_b$ shows a linear dependence on $\lambda$.

Between the up- and down-bending regime ($\lambda = 0.035 – 0.04$) the disk profiles are very close to exponential over a range that exceeds the typical position of disk breaks (8-10 kpc) for other spin parameters. In such cases the fitting function from equations (2.5) and (2.6) is overfitting the data as $R_b$, $R_i$ and $R_o$ are degenerate. If the parameter
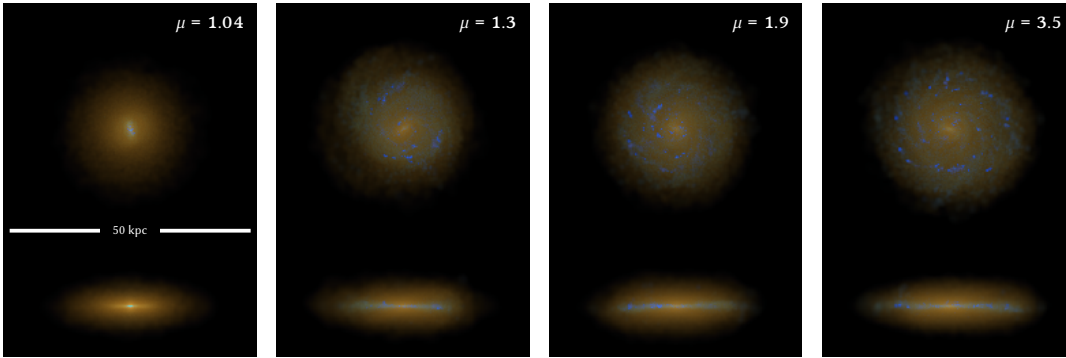
**Figure 2.5:** The same as figure 2.2 but for the second suite of simulations with constant $\lambda = 0.04$.

sampling in these cases converges at all it usually only probes a local maximum of the posterior PDF. In most cases two of the degenerate parameters cannot be constrained properly by the parameter estimation. Here, I opt for a realization that constrains $R_i$. Thus, the values for the unconstrained parameters $R_o$ and $R_b$ usually have large scatter and are plotted fainter in figure 2.4.

In the $\lambda = 0.04$ case, the best fit for $R_b$ is at the end of the disk. Therefore the fitted break radius exceeds the otherwise linear relation with $\lambda$ as can be seen in the middle panel of figure 2.4. In the $\lambda = 0.035$ case, the best fit for $R_b$ is at a minor wiggle in the profile. The result is that $R_b$ does not fit the relation with $\lambda$ either but here it falls short.

## 2.2.2 The Effect of the Angular Momentum Distribution

Here I present the results for the second suite with fixed halo spin parameter $\lambda = 0.04$. These results have not been published but complement the results published in Herpich et al. (2015a, see also section 2.2.1).

The figures 2.5, 2.6 and 2.7 show the equivalent data to the figures 2.2, 2.3 and 2.4 for the second suite of simulations. Note that the $\mu = 1.3$ simulation is the exact same simulation than the $\lambda = 0.04$ simulation from the first suite. The profiles show the same qualitative dependence on $\mu$ than on $\lambda$: low values of $\mu$ lead to Type-III and high values to Type-II disks. However, the transition between the two regimes is not as sharp as it is when $\lambda$ is varied. This may be due to the lower number of actual simulations in this suite.
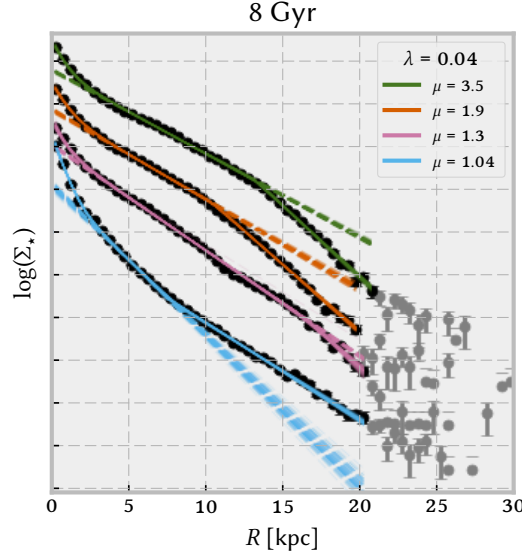
**Figure 2.6:** The same as figure 2.3 but for the second suite of simulations with constant $\lambda$ = 0.04. The figure qualitatively shows that there is a trend from antitruncated (Type-III) disk profiles for galaxies with a small value for the shape parameter to truncated (Type-II) profiles for high values.

## 2.3  Radial Redistribution

In this section I briefly lay out a possible mechanism that may be the cause for systematic changes of the disk profile with $\lambda$. Figure 2.8 compares the final stellar surface density profile to the density profile of stars at birth, irrespective of their actual time of birth. Hereafter, I refer to these as the *final* and *formation* profiles respectively.

The two panels in figure 2.8 show profiles for two different simulations, one with a spin parameter below the transition region between up- and down-bending disks ($\lambda$ = 0.03, left panel) and one above ($\lambda$ = 0.06, right). In the $\lambda$ = 0.03 case we see that stars are formed with a very concentrated profile (red) that has a core in the center. This core might be artificial due to centering issues. What is evident without doubt is that practically all stars formed in the inner $\approx$ 8 kpc of the disk, while the final profile (blue) extends all the way out to $\approx$ 30 kpc.

The figure shows that in the range $2\,\text{kpc} \lesssim R \lesssim 5\,\text{kpc}$ the formation profile significantly exceeds the final profile. Inside and outside that range the opposite is the case. This is because the integrated mass of the current and formation profiles are identical. It follows that a substantial amount of stellar redistribution has occurred
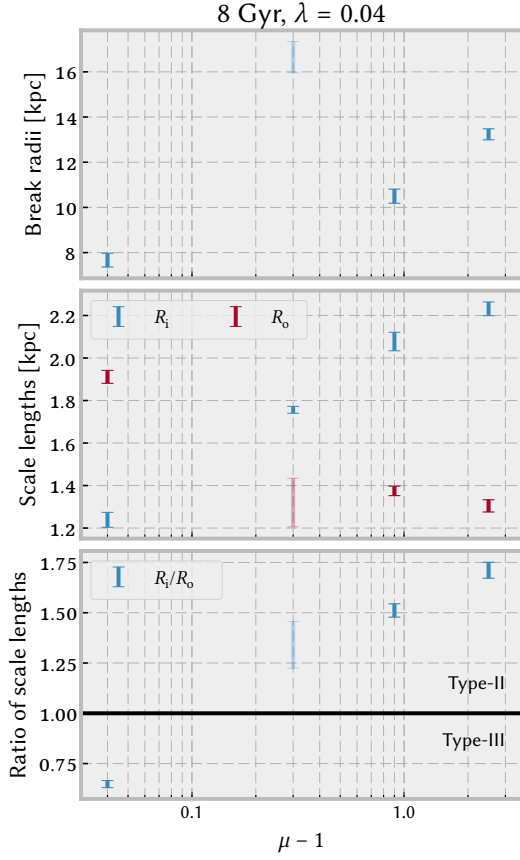
**Figure 2.7:** The same as figure 2.4 but for the second suite of simulations with constant $\lambda = 0.04$ and as a function of $\mu$. The estimates for some parameters for $\mu = 1.3$ are plotted fainter since they are somewhat ill-defined in these cases (see text). The figure shows a clear trend from Type-III to Type-II profiles as $\mu$ increases and a transition (Type-I) at $\mu \approx 1.3$.

from $2\,\mathrm{kpc} \lesssim R \lesssim 5\,\mathrm{kpc}$ outwards as well as inwards.

For $\lambda = 0.06$ the same qualitative effect can be observed but there are two striking differences with important implications. First, star formation extends to much larger radii ($\approx 13\,\mathrm{kpc}$). Second, despite the same qualitative trend, the differences between the formation and final profiles are much smaller. The final profile closely follows the formation profile out to $\approx 10\,\mathrm{kpc}$ and there is no central core in the formation profile. There is a steeply declining tail of stars that have reached large radii, leading to the down-bending profile. Therefore the amount of stellar redistribution that took place in this *high-spin* case is much less than in the *low-spin* case. This simple qualitative analysis of radial mass redistribution is restricted to these two simulations. The intermediate cases show a monotonic trend between those shown in figure 2.8. In section 3.1.2, I present a more quantitative analysis of this effect.
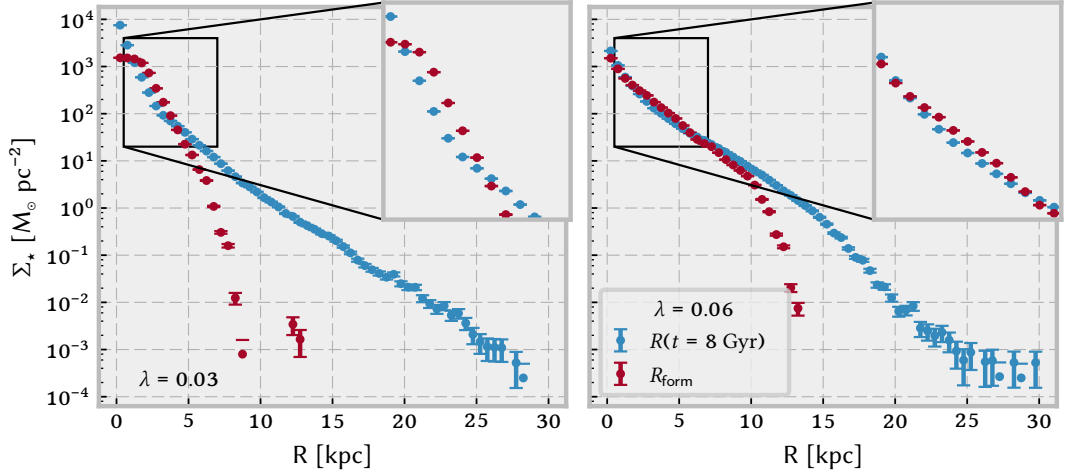
**Figure 2.8:** Comparison of stellar surface density profiles with respect to the current position of star particles (blue) and to their position at the time of formation (red). The left and right panels show the results for $\lambda = 0.03$ and $\lambda = 0.06$ respectively. The insets show a zoom of the profiles in the central region. The figure clearly shows that the amount of radial redistribution of stellar mass is much more pronounced for the case with small $\lambda$.

## 2.4 Summary

Using numerical models of disk galaxy formation I find a correlation between the initial spin of the host halo and the shape of the radial profile of the stellar disk. I also find a similar correlation with the shape of the angular momentum distribution and comment on the implications of the similar behavior of the two suites of simulations at the very end of this chapter.

I find that the simulated galaxies with an initial spin parameter $\lambda \leq 0.03$ form an antitruncated (Type-III) disk profile while larger values ($\lambda \geq 0.045$) yield truncated (Type-II) disks. Purely exponential (Type-I) disks occur only right at $\lambda \approx 0.035$ which coincides approximately with the median of the $\lambda$ distribution in cosmological simulations ($\lambda = 0.031$, Macciò et al. 2008). Thus, the model explains why only some late-type galaxies exhibit purely exponential disk profiles, while the majority of them show breaks in the outer disk profiles. As the transition between Type-III and Type-II disk profiles ($\lambda = 0.035$) in the model coincides with the median of the $\lambda$ distribution, one would expect roughly equal abundances of up- and down-bending profiles which is comparable but not equal to observational results (30 % and 60 %, Pohlen and Trujillo 2006). A possible cause for this discrepancy between the model and observations is that gas in cosmological simulations generally has larger angular momentum than the DM (Stewart et al. 2013).

Qualitatively, I find the same correlation of the type of disk break with the shape parameter $\mu$ of the initial angular momentum distribution. As shown before in figure 2.1 the values of $\lambda$ and $\mu$ are negatively correlated with the fraction of low-angular momentum gas. Therefore, a plausible conclusion is that Type-III profiles form when large amounts of low angular momentum gas is present in a galaxy and Type-II profiles form when only little of this gas is present. This slightly modifies the conclusion we make in our paper (Herpich et al. 2015a) where I link Type-III breaks to low initial halo spin $\lambda$. I comment on this conclusion in more detail in section 3.7 in the following chapter.

# 3 Type-III breaks through Secular Evolution

The results presented in this chapter have been submitted as a paper to the astro-physical journal *Monthly Notices of the Royal Astronomical Society* and is still in the reviewing process. I carried out all the presented research myself. The initially sub-mitted version is available as an arXiv preprint (Herpich et al. 2015b). In the course of the refereeing process, the text of the initially submitted version has changed substantially including a slightly modified central conclusion. This chapter is based on the current version of the respective paper.

In this chapter, I present results of a more detailed analysis of the first suite of simulations from the previous chapter, the one with fixed shape parameter $\mu$ = 1.3 and varied spin parameters $\lambda$. I investigate the amount of stellar migration that stars in the outskirts of the simulated disks experience and how their orbit properties change. I argue that the process of formation of Type-II breaks in the high-spin disks is consistent with that found by Roškar et al. (2008a) (see section 1.6.3). Instead I focus on one of the simulations that formed a Type-III disk ($\lambda$ = 0.02). I show that the large amount of low-angular momentum gas in the initial halo promotes the formation of a massive central bar. I link the dynamics of the stars that make up the outer part of the broken Type-III disk to the formation of the bar.

## 3.1 Properties of the Simulated Disks

Throughout this chapter I, use the term *outer disk* to refer to the set of stars, which are located outside the position of the break in the radial profile in the final simulation output after 8 Gyr. Quantities denoted by the subscript *now* refer to the respective value in the final simulation snapshot after 8 Gyr.

### 3.1.1 Structure in the Disks

In figure 3.1, I present the average stellar overdensity relative to the mean density $\delta = \Sigma_\star \left( R, \varphi \right) / \langle \Sigma_\star \rangle (R) - 1$ at the respective radius in polar coordinates. In the lowest
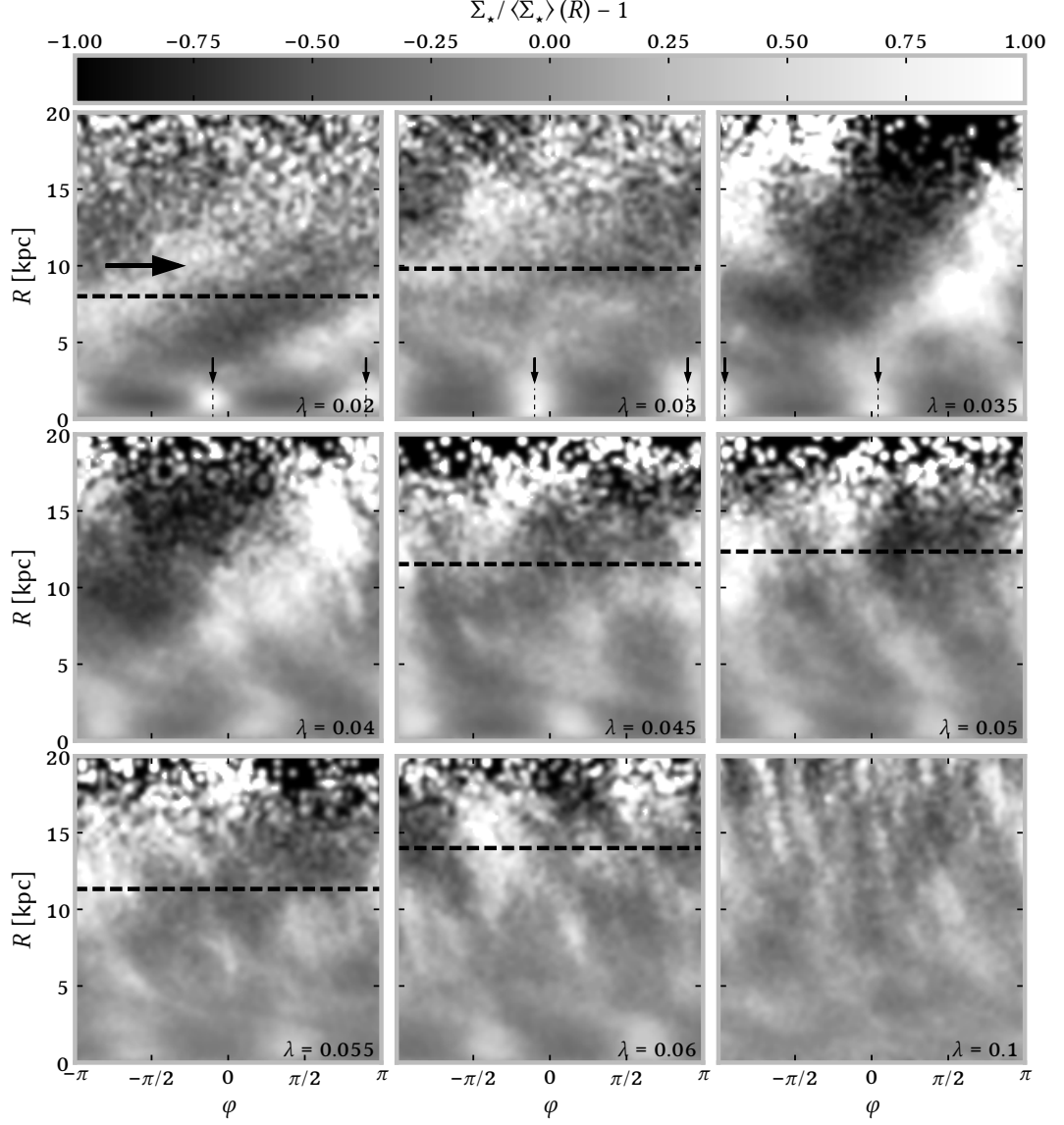
**Figure 3.1:** The plot shows the relative stellar overdensity $\delta = \Sigma_\star (R, \varphi) / \langle \Sigma_\star \rangle (R) - 1$ in polar coordinates for each simulated galaxy after $8\,\mathrm{Gyr}$. The horizontal arrow in the top left panel indicates the sense of rotation of all galaxies. The horizontal dashed lines indicate the position of the break (except for the type-I disks; for $\lambda = 0.1$ the break is located just outside the plotted range). The small vertical arrows and corresponding dotted lines in the top row indicate the position of the bar in the lowest spin simulations.

spin simulation (top left panel) there is a small but strong bar (vertical features offset by $\Delta\varphi = \pi$ indicated by the small vertical arrows). The bar signature gets weaker with increasing spin and completely disappears for the highest spin simulation. While the disks of the high spin galaxies ($\lambda > 0.04$) feature complex trailing patterns, the lowest spin galaxies exhibit a one-armed leading pattern, which is probably an indication that the galaxy is lop-sided. This is consistent with the visual impression from figure 2.2.

### 3.1.2 The Stellar Population of the Outer Disks

Based on very similar simulations, Roškar et al. (2008a) reproduced the formation of Type-II disk breaks. In their simulations, stars later found in the disk outskirts formed inside the break radius. They found no evidence for radial heating causing migration but instead resonant scattering off of transient spiral arms (Sellwood and Binney 2002) to be responsible for the outward migration of stars. An important signature of this mechanism is that the migrated stars in the outer disk are predominantly on near-circular orbits, i. e. rotationally supported (see also Roškar et al. 2012, and section 1.6.3). In this section I present evidence that the migration mechanism in my high-spin simulations is consistent with this mechanism. These are the simulations that produce Type-II disk profiles as well (figure 2.4). I also show that the low-spin simulations, which exhibit Type-III breaks, are inconsistent with this process.

I first confirm the finding of section 2.3 that all outer disk stars in all of the simulated galaxies must have migrated outward from inside the respective break radii. Additionally, I show that the outer disk stars in the disks with Type-III profiles stem from the vicinity of the galactic center, while their counterparts in the disks with Type-II profiles were born further out in the disk. This is followed by showing that the outer disk stars in the Type-III cases are on very eccentric orbits.

Figure 3.2 shows the distribution of birth radii of the stars in the outer disk. Practically all outer disk stars are born inside the respective break radius. There is a stark difference between the low- and high-spin cases. In low-spin simulations, almost all outer disk stars are born well inside the break radius, $R_{\text{birth}} < R_{\text{break}}/3$. In the high-spin cases the birth radii are located at larger galactocentric distances, $R_{\text{birth}} \approx R_{\text{break}}/2$. This difference is even more clear in absolute values as the break radii grow with $\lambda$ (figure 2.4). I summarize that in all cases the outer disk stars migrate from inside the break region and in the case of the lowest-spin simulations originate from predominantly very small radii.

Now, I characterize stellar orbits in the simulations through their circularity parameter $j_z/j_c$ ($e$). The circularity parameter is the $z$-component of a star's specific angular momentum $j_z$ normalized by the specific angular momentum $j_c$ ($e$) of a circular orbit
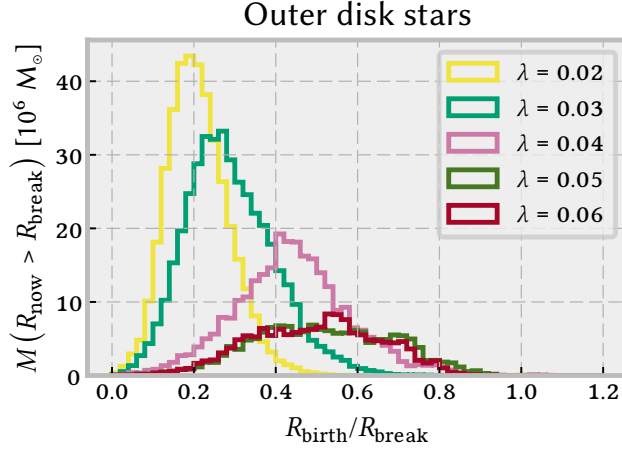
**Figure 3.2:** The distribution of birth radii for outer disk stars. The radii are normalized by the break radius in the final snapshot. Practically all stars beyond the break region were born at smaller radii. The effect is most extreme for the Type-III breaks ($\lambda \leq 0.03$).

at the same specific orbital energy $e$. By construction a particle on a perfectly circular orbit has $j_z/j_c\,(e) = 1$. Particles on perfectly radial orbits satisfy $j_z = j_z/j_c\,(e) = 0$. In practice I consider every particle with $0.8 \leq j_z/j_c\,(e) \leq 1$ to be on a near-circular orbit and particles with $j_z/j_c\,(e) \approx 0$ on radial orbits. Eccentric orbits cover the range in between these two limiting cases. Negative values correspond to counter-rotating orbits.

Figure 3.3 presents mass-weighted histograms of the distribution of $j_z/j_c\,(e)$ for outer disk stars from a selection of the simulations. For the Type-II breaks ($\lambda \geq 0.045$) the orbit distribution peaks at $j_z/j_c\,(e) > 0.8$. Most of the orbits are near-circular, and thus consistent with the mechanism proposed by Roškar et al. (2008a). The presence of complex spiral patterns in those galaxies (see figure 3.1) supports this hypothesis. The simulations with Type-III breaks ($\lambda \leq 0.03$), on the other hand, only have very few outer disk stars that are on near-circular orbits. Contrary to the higher spin simulations, the distribution of the circularity parameter drops to 0 at values of $j_z/j_c\,(e) \approx 0.8 - 0.9$ in these cases. The $j_z/j_c\,(e)$ distribution peaks roughly at $j_z/j_c\,(e) = 0.5$, which corresponds to rather eccentric orbits. This lack of near circular orbits beyond the break in the simulations with Type-III disk breaks disfavors radial migration, as described in section 1.7.2, as a possible formation mechanism because it is less efficient for eccentric orbits (Sellwood and Binney 2002).

I find no evidence that the formation mechanism of the Type-II breaks differs from that of Roškar et al. (2008a). Therefore, I focus the further analysis on the yet
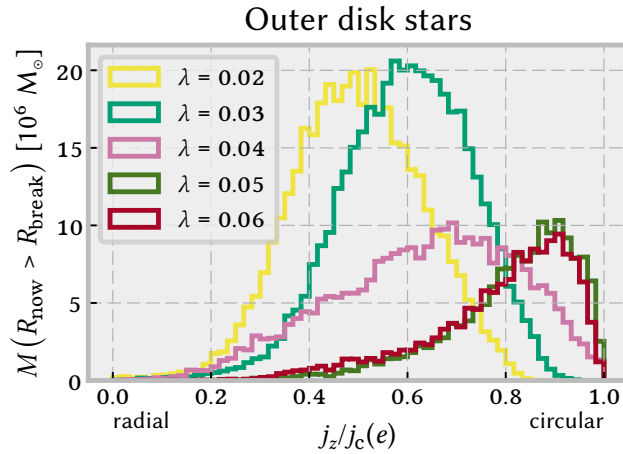
**Figure 3.3:** Circularity distribution in outer disk. The figure shows the circularity distribution of outer disk stars ($R_{now} > R_{break}$) for a selection of the simulations spanning the range from low ($\lambda$ = 0.02) to high spins ($\lambda$ = 0.06). Most orbits in the high-spin simulations ($\lambda > 0.04$) are circular while there is not a single star with $j_z/j_c$ ($e$) > 0.85 in the lowest-spin simulation. Intermediate-spin simulations show a broad circularity distribution in the outskirts ranging from completely radial ($j_z/j_c$ ($e$) = 0) to circular ($j_z/j_c$ ($e$) = 1). For purely exponential disks the "break radius" is determined from linear interpolation of the position of the break from the $\lambda$ = 0.03 and $\lambda$ = 0.05 simulations.

unexplained Type-III breaks. For that I study the stellar dynamics in the $\lambda$ = 0.02 simulation for the rest of this chapter. The break radius of this galaxy is $R_{break}$ = (8.0 ± 0.5) kpc.

## 3.2 Orbit Evolution in the Outskirts of Type-III Disks

Given the substantial radial mass redistribution in Type-III disks, I now explore what mechanism is most important in driving this redistribution. Figure 3.4 shows the distribution of the circularity parameter $j_z/j_c$ ($e$) in the outer disk (solid line) compared to the stars' $j_z/j_c$ ($e$) distribution at birth (dashed). Most of the outer disk stars were born on near-circular orbits. Thus, there must be a mechanism which transforms orbits from circular to radial and significantly increases the orbits eccentricity.

In order to figure out how orbits get transformed, I look into the time evolution of the orbit of one particular stellar particle. Figure 3.5 presents the evolution of orbital parameters of a sample star particle from the outer disk. The four panels show (from
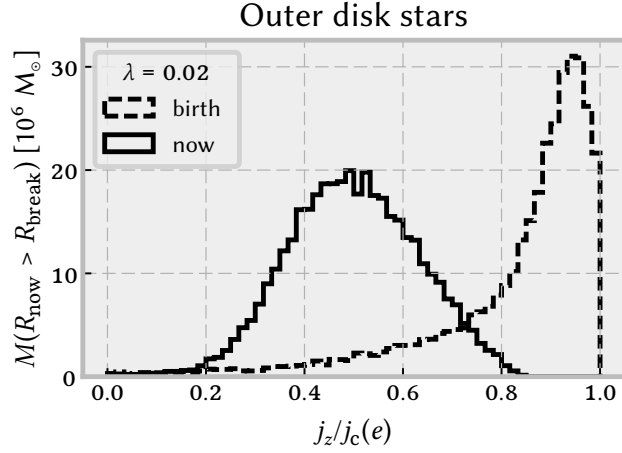
**Figure 3.4:** Circularity evolution in a low spin simulation. The figure shows the distribution of the circularity parameter $j_z/j_c$ ($e$) of the stars outside the break radius at their formation (dashed) and in the final snapshot (solid). When these stars are born, most of them are on a near-circular orbits but now almost all the orbits are eccentric.

top to bottom) the time evolution of the star's radial position $R$, specific orbital energy $e$, specific angular momentum $z$-component $j_z$ and circularity parameter $j_z/j_c$ ($e$). The times of pericenter passage are marked by vertical dashed lines.

After 4.5 Gyr the star gains or loses energy (second panel) and angular momentum (third panel) at each pericenter passage. When the star is far away from pericenter, its energy stays constant, but it loses specific angular momentum (third panel), which reduces the circularity of its orbit (bottom panel).

During this time span, the binding energy evolves approximately following a step function. The steps occur at pericenter. If the star gains energy $e$ at pericenter its orbit's semi-major axis increases and vice versa. The pericenter, however, stays more or less constant at approximately 2 kpc. The figure clearly shows that the growth of the orbit's semi-major axis is driven by a gain in specific energy $e$.

This particular star has a net gain in energy, which is not surprising as it has been selected from the outer disk in the final simulation output. In general, it is also possible for a star to have a net loss of energy. Such stars migrate towards the galaxy center and, therefore, cannot be found in the outer disk.

Before 4.5 Gyr, the star in figure 3.5 has a rather small semi-major axis (< 4 kpc) and the steps in the evolution of its binding energy are smoother and not as well defined yet. Generally, the binding energy of the star is constant when it is far away from the center and varies only near the center. Thus, I expect the source of the variation
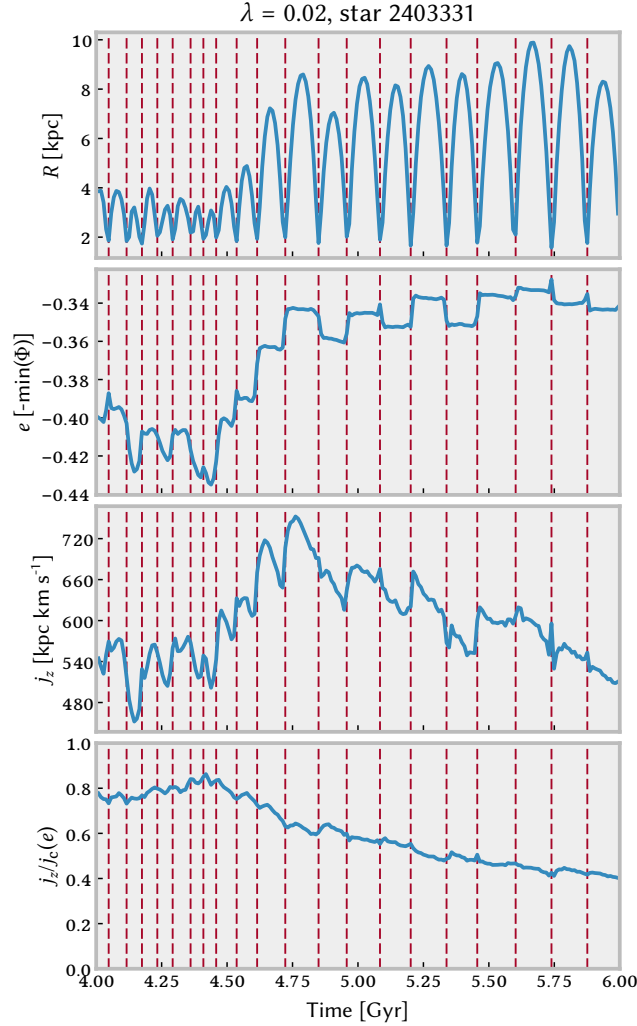
**Figure 3.5:** Orbit evolution of an individual star. The vertical dashed lines indicate the pericenter passages of that star. The top panel shows the evolution of its radial position, the second panel shows its orbital energy, the third panel shows the evolution of its $z$-component of specific angular momentum and the bottom panel shows its circularity parameter. While the star's apocenter is still small ($t \lesssim 4.5\,\mathrm{Gyr}$) its binding energy is almost permanently changing. After approximately $4.5\,\mathrm{Gyr}$ its apocenter growths significantly and the star's binding energy turns into a step function with steps occurring only at pericenters. The star particle instantaneously gains energy and angular momentum during many pericenter passages. In between these passages its energy stays constant but it looses angular momentum, which causes the particle's circularity to decrease steadily.

of binding energy to be in the center of the galaxy. As I show later (sections 3.3.1 and 3.4), the source is the central bar. I stress that the behaviour of the star, displayed in figure 3.5, is qualitatively similar to that of other stars found in the outskirts of the low-spin disks.

## 3.3 The Properties of Bars in the Simulated Type-III Disks

Particle orbits seem most affected in the center of galaxies near a possible bar. I characterize the bar using the coefficient of the $m = 2$ Fourier mode:

$$\tilde{A}_2 = \sum_j \exp\left(i2\varphi_j\right) m_j \qquad (3.1)$$

where $m_j$ and $\varphi_j$ are the mass and azimuth angle of the stars. The sum is over all stars in the considered region[1] of the galaxy. This $m = 2$ mode encodes two relevant quantities, namely the relative bar strength

$$A_2/A_0 = \frac{\left|\tilde{A}_2\right|}{\sum_j m_j} \qquad (3.2)$$

and the bar's position angle

$$\theta_2 = \frac{\arg\left(\tilde{A}_2\right)}{2} \quad \mod \frac{2\pi}{2}. \qquad (3.3)$$

Here, I calculate $\tilde{A}_2$ based on all stars in a spherical region around the center with a radius of 1 kpc. The relative bar strength and the position angle show only a weak dependence on the size of the spherical region.

In figure 3.6, I present the time evolution of the bar strength in the simulations. The lowest-spin simulation has the strongest bar. Its bar strength exceeds that of the high-spin simulations for a continuous period of 4 Gyr or more. During this period its value is remarkably constant, except for a small dip just after 3 Gyr.

The only other simulation, which exhibits a strong bar, is the one with the second lowest initial spin. Thus, the only simulations in this sample with a strong bar are also the only ones, which form a Type-III break. This correlation encouraged me to search for a possible dynamical link between bars and Type-III breaks in the simulations.

---

[1] e. g. annular bins or spherical regions of variable size
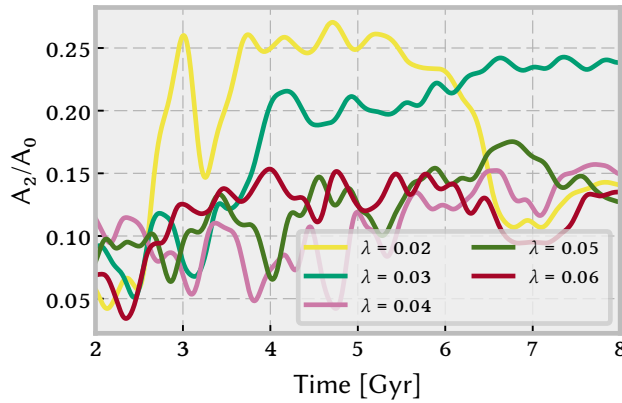
**Figure 3.6:** The figure shows the relative amplitude of the $m = 2$ Fourier mode of all stellar particles inside $1\,\mathrm{kpc}$ as a function of time. While the values for intermediate- and high-spin are rather low, there is an excess in bar strength for the lowest-spin ($\lambda = 0.02 - 0.03$) simulations for a period of about $4\,\mathrm{Gyr}$.
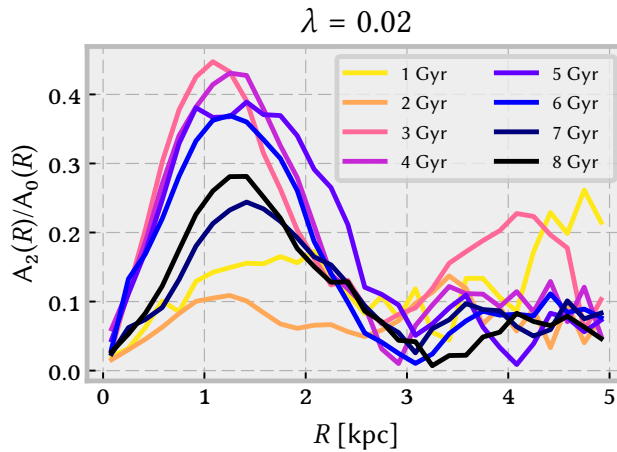


**Figure 3.7:** The plot shows the relative amplitude of the $m = 2$ mode in radial bins of the stars in the $\lambda = 0.02$ simulation at different times. The bar forms after $2$-$3\,\mathrm{Gyr}$ (see also figure 3.6) and it extends out to $2\,\mathrm{kpc}$.

Figure 3.7 shows the relative bar strength in different radial bins at different output times for the $\lambda = 0.02$ galaxy. The size of the bar does not evolve significantly. It ends at $\approx 2\,\mathrm{kpc}$, so it makes sense to look for possible effects on star particles' orbits inside that region.
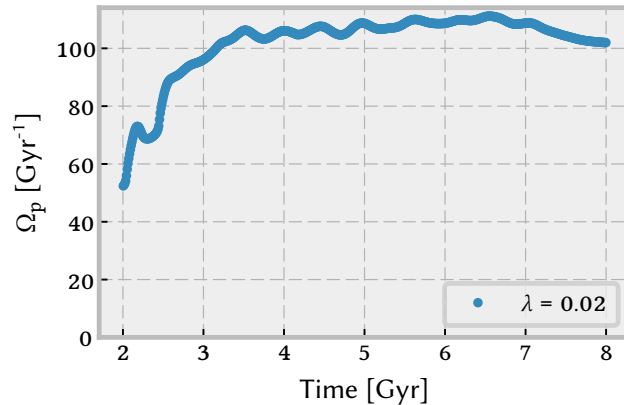
**Figure 3.8:** The figure shows the bar pattern speed of the $\lambda = 0.02$ simulation as a function of time. Before its formation ($\approx 3\,\mathrm{Gyr}$, see figure 3.6) it varies but later on it is fairly constant.

The pattern speed $\Omega_p$ of the bar is the time derivative of the bar's position angle $\theta_2$ (equation 3.3). A more robust method to determine the bar's patterns speed is to calculate the Fourier transform of the time evolution of the complex $m = 2$ Fourier coefficients $\tilde{A}_2$. A very comprehensive description of the procedure is presented in Quillen et al. (2011).

Figure 3.8 presents the pattern speed of the bar in the low-spin ($\lambda = 0.02$) simulation as a function of time. Once the bar has formed, its pattern speed is remarkably constant, which is important when I discuss the interaction of stellar particles and the bar in section 3.3.1.

To summarize, low angular momentum simulations develop strong and long-lived bars that have a stable pattern speed over a number of Gyrs. When the bar forms it may trap particles at its resonances. These stars are expected to oscillate radially (Sellwood and Binney 2002) but stay bound to the bar. Note, that such strong bars are known to cause considerable heating of stellar orbits (Hohl 1971).

### 3.3.1 The Signature of the Strong bar in a Simulated Type-III Disk

The top row of figure 3.9 shows the current position of the star particle from figure 3.5 during one direct interaction with the bar that significantly increases its binding energy $e$ and semi-major axis.

The panels in the top row of the figure show that the star and the bar have the same sense of rotation and that the azimuthal phase of the star lags behind that of the bar.
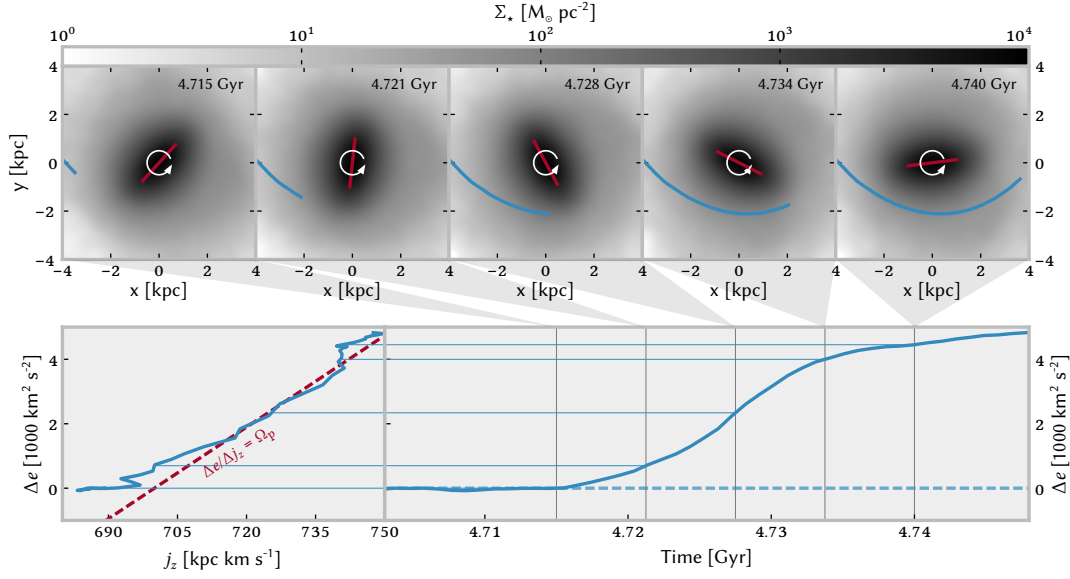
**Figure 3.9:** The panels in the top row show the trajectory of an individual star in the $\lambda$ = 0.02 simulation during one pericenter passage. The stellar surface density is projected as a gray-scale in logarithmic scaling. The bar's orientation is indicated by the red line. Its sense of rotation is indicated by the white arrow. The star is the same as that in figure 3.5. The bottom left panel shows the star's trajectory in the Lindblad diagram (blue line). The slope of the red dashed line in the bottom left panel is the bar's pattern speed $\Omega_p$ indicating the trajectories of constant Jacobi energy. The bottom right panel shows its specific orbital energy $e$ as a function of time. The value of $e$ is given relative to its value before the encounter which is indicated by the blue dashed line. The corresponding time of each panel in the top row is indicated by a vertical line in the bottom right panel. The figure shows that significant evolution of the star's orbital energy occurs during pericenter passage. The slope of its trajectory in the Lindblad diagram is very similar to the bar's pattern speed. This indicates that the bar-induced potential perturbation is responsible for the energy gain.

During the period that is shown in these images, the star gains a significant amount of binding energy $e$ (bottom right panel). The slope of the star's trajectory in the Lindblad diagram (bottom left panel, blue) is remarkably similar to $\Omega_p$, particularly for 4.721 kpc < $t$ < 4.734 kpc (the three panels in the center of the top row), which is the time period during which the evolution of the binding energy $e$ is the strongest (bottom right panel). According to equation (1.8), this is the expected trajectory from the interaction of a star with the bar, given its constant pattern speed. Taking into account that the orbital binding energy only changes in the vicinity of the bar (see figure 3.5), I interpret this as a clear signature of the bar as the dominant driver of the star's energy gains (losses).

The encounter of the star and the bar are analogous to a *swing-by*. The star is
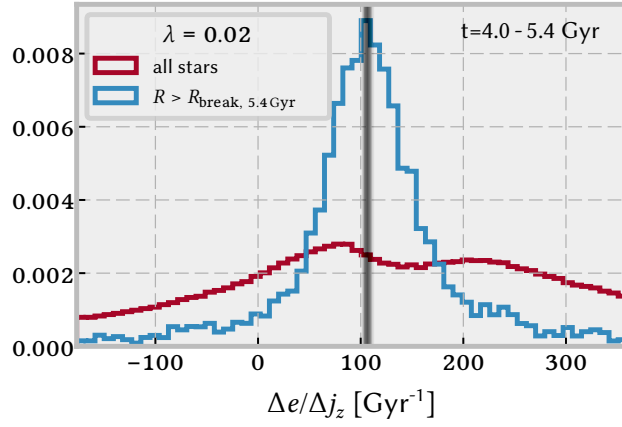
**Figure 3.10:** Mass weighted distribution of $\Delta e/\Delta j_z$ of stars located outside the break radius at $5.4\,\mathrm{Gyr}$ (blue) and all stars (red) of the lowest-spin simulation ($\lambda = 0.02$). The time range ($4.0\text{-}5.4\,\mathrm{Gyr}$) was chosen to coincide with the times where the bar is both, at its peak strength and its pattern speed is approximately constant. The vertical gray bar indicates the range of measured values of the bar pattern speed in the respective time span. It coincides remarkably well with the peak of the distribution for the outer disk stars. The peak is not present in the global distribution.

exposed to an extended period of acceleration due to the moving potential well of the bar—it is *surfing* in the bar's potential.

So far I investigated the behavior of a single star. However, finding a mechanism that drives a single star's migration out into the outer disk does not explain the formation of the Type-III profile of this disk. In order to show that the behavior of that star is typical, I show that there is a prominent signature of the bar in the outer disk stars' orbit evolution[2]. I use equation (1.8) which implies that the ratio of $\Delta e$ and $\Delta j_z$ equals the bar's pattern speed $\Omega_p$.

Figure 3.10 shows the normalized mass-weighted distribution of $\Delta e/\Delta j_z$ of stars in the $\lambda = 0.02$ simulation. It covers the time range from 4.0-5.4 Gyr when the bar is both, strong and has a constant pattern speed (see Figures 3.6 and 3.8). The blue histogram considers stars, which are located outside the break radius at 5.4 Gyr into the simulation. The break radius at this time was $R_{\mathrm{break},\,5.4\,\mathrm{Gyr}} = 7.6\,\mathrm{kpc}$. The red histogram shows the same for all stars in the simulation, which were born before 4.0 Gyr. Stars from outside the profile break show a clear peak in their orbit evolution of $\Delta e/\Delta j_z$ which coincides remarkably well with the bar's pattern speed $\Omega_p$ (vertical

---

[2]This signature can also be caused by different non-axisymmetric perturbations, which are rotating with the same pattern speed. However, the only such perturbation that was found in the simulation is the bar.

bar). There is a small feature in the global distribution (red) but it is offset from $\Omega_p$ and much less prominent. Given the constant pattern speed of the bar, this agreement for the stars in the outskirts matches the prediction of equation (1.8) for the imprint of the bar on stellar orbits. Thus, it suggests that the bar is the dominant driver of the outward migration happening in the simulations.

## 3.4 A Toy Model for the Orbit Evolution in Disks with Strong Bars

I set up a very simple toy model to illustrate that the proposed mechanism is indeed capable of increasing the semi-major axes of stellar orbits. Here, the only asymmetry is a bar-like, rotating, non-axisymmetric perturbation in an otherwise axisymmetric potential. Its purpose is to support the above interpretation of the dynamics of outer disk stars. I show that the interactions of test particles with a bar-like perturbation can reproduce the qualitative behavior of stellar particles in the outer disk of the simulation. Thus, other effects are not necessary to qualitatively reproduce the kinematics of outer disk stars. This supports the result that the bar is the main driver in the formation of Type-III disk profiles.

### 3.4.1 The Toy Model Setup

This toy model is restricted to the galactic plane where the vertical spatial coordinate satisfies $z = 0$ for simplicity. Hence, the notation for 2- and 3-dimensional distances $R$ and $r$ are indistinguishable.

In this model, test particles move in a NFW potential (Navarro, Frenk, and White 1997)

$$\Phi_0\left(|\mathbf{r}|\right) = \Phi_{\min} \frac{\ln\left(1 + |\mathbf{r}|/s\right)}{|\mathbf{r}|/s} \tag{3.4}$$

with a rotating non-axisymmetric Gaussian perturbation

$$\Phi_p\left(\mathbf{r}, t\right) = f\Phi_{\min} \exp\left[-0.5\left(\frac{x'(t)^2}{\sigma_x^2} + \frac{y'(t)^2}{\sigma_y^2}\right)\right] \tag{3.5}$$

in the center, where

$$\begin{pmatrix} x'(t) \\ y'(t) \end{pmatrix} = \begin{pmatrix} \cos\varphi(t) & -\sin\varphi(t) \\ \sin\varphi(t) & \cos\varphi(t) \end{pmatrix} \begin{pmatrix} x \\ y \end{pmatrix} \tag{3.6}$$

and

$$\varphi(t) = -\Omega_{\mathrm{p}} t - \varphi_0. \tag{3.7}$$

In the above equations $\Phi_{\mathrm{min}}$ is the minimum unperturbed potential, $r_{\mathrm{s}}$ the scale radius of the NFW potential, $f$ the relative strength of the perturbation, $\sigma_{x,y}$ the extent of the perturbation in $x$ and $y$ direction[3], $\Omega_{\mathrm{p}}$ the perturbation's pattern speed and $\varphi_0$ the initial phase of the perturbation's position angle. The total potential then is

$$\Phi(\boldsymbol{r}, t) = \Phi_0(|\boldsymbol{r}|) + \Phi_{\mathrm{p}}(\boldsymbol{r}, t). \tag{3.8}$$

This yields a static NFW potential superimposed with a 2D-Gaussian perturbation that is rotating with an angular speed of $\Omega_{\mathrm{p}}$ in the positive sense of rotation. Note, that the particles in this model are *not* self-gravitating. Therefore, gravitationally driven instabilities, as described in section 1.6.4, are impossible here.

I set up a stellar disk with an initially exponential surface density profile and follow the evolution of the stars in this disk in two realizations of the above potential with different perturbation strengths: $f = 0.01, 0.05$. I refer to them as the *weak* and *strong* model, respectively. The initial velocities are set such that the orbits would be circular in the azimuthally averaged potential. The values of the model parameters are given in table 3.1.

The test particles' coordinates are evolved with a Leap-Frog integration scheme with a time step of $10^{-3}\,\mathrm{kpc\,s/km} \approx 10^{-3}\,\mathrm{Gyr}$. The relative error of the Jacobi-integral is of order $O(10^{-4})$ except for a few particles with very small initial radii ($\lesssim 0.02\,\mathrm{kpc}$).

## 3.4.2  Qualitative Comparison to Orbit Evolution of Type-III Disks

In figure 3.11, I compare the evolved surface density profile of the weak (red) and the strong (blue) model to the initial (purple) profile. In the weak case there is no significant evolution of the surface density profile. There is merely a small feature at the location of the OLR (3.4 kpc). This is consistent with the results of Sellwood and Binney (2002).

The profile of the strong model has a dip at the position of the CR and just inside the OLR as well as an excess outside the OLR. This indicates that there is significant outward migration from the CR and the OLR. Note that the determination of the position of the CR and OLR is somewhat dubious because it is based on the existence of nearly circular orbits. In a strict sense, such orbits cannot exist in a strongly non-axisymmetric potential. When I calculate the location of the resonances, I use

---

[3]Note that non-axisymmertry requires $\sigma_x \neq \sigma_y$.

**Table 3.1:** Toy model parameters. $N$ is the number of test particles and $\epsilon_{\text{init}}$ their initial orbit eccentricity. $R_{\text{exp}}$ is the scale length of the initial exponential surface density profile. All other quantities correspond to those in equations (3.4)-(3.7).

|  | Units | Model | |
|---|---|---|---|
|  |  | weak | strong |
| $f$ |  | 0.01 | 0.05 |
| $\Phi_{\text{min}}$ | $[\text{km}^2\,\text{s}^{-2}]$ | $-3 \times 10^5$ | |
| $r_s$ | $[\text{kpc}]$ | 10 | |
| $\sigma_x$ | $[\text{kpc}]$ | 2 | |
| $\sigma_y$ | $[\text{kpc}]$ | $\sqrt{2}$ | |
| $\Omega_{\text{p}}$ | $[\text{rad}\,\text{Gyr}^{-1}]$ | 100 | |
| $\varphi_0$ | $[\text{rad}]$ | random | |
| $R_{\text{exp,init}}$ | $[\text{kpc}]$ | 1 | |
| $\epsilon_{\text{init}}$ |  | 0 | |
| $N$ |  | $10^5$ | |
| $t_{\text{final}}$ | $[\text{Gyr}]$ | 4 | |
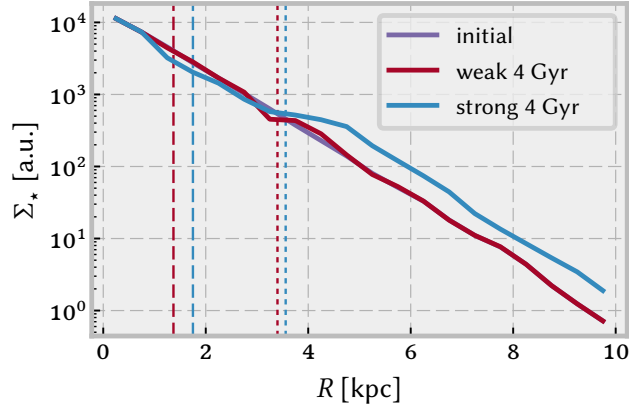


**Figure 3.11:** The surface density profiles after $4\,\text{Gyr}$ of the weak (red) and strong (blue) model compared to the initial profiles (purple). A substantial part of the purple line is not visible because it is hidden behind the red line. The dashed and dotted vertical lines represent the location of the CR and OLR, respectively. While the strong model shows a dip at CR and an excess of particles outside of the OLR, the profile of the weak model remains mostly unchanged except for a small wiggle at the OLR.
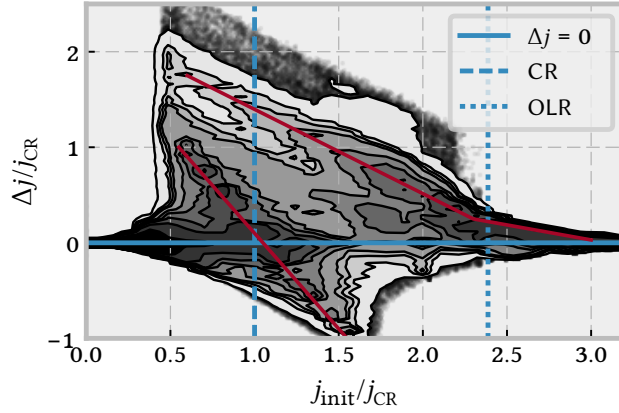
**Figure 3.12:** The change in specific angular momentum $j$ of the test particles in the strong model after $4\,\mathrm{Gyr}$ as a function of their initial specific angular momentum. The horizontal solid line indicates the locus of zero change in $j$. It separates outward migration ($\Delta j > 0$) from inward migration ($\Delta j < 0$). The dashed and dotted vertical lines indicate the values of $j$ that correspond to the CR and OLR respectively. The two most prominent features are highlighted by the red lines.

the azimuthally averaged potential $\langle\Phi\rangle\,(|\boldsymbol{r}|) = \int_0^{2\pi} \mathrm{d}\varphi\,\Phi\,(\boldsymbol{r})$ where $\varphi$ is the azimuth angle in polar coordinates. I show later (figure 3.12) that the resulting resonances agree well with major changes in particles' angular momentum.

### 3.4.3 The Dominant Resonances for Type-III Disk Formation in the Toy Model

I now explore where these excess particles in the strong model come from. Figure 3.12 shows the change of specific angular momentum $\Delta j$ of each test particle in the strong model as a function of its initial specific angular momentum $j_{\mathrm{init}}$. There is a strong feature that intersects $\Delta j = 0$ at the CR. A second strong feature corresponds to the OLR but does not intersect $\Delta j = 0$. Both are marked with a red line. Generally there is only moderate inward migration ($\Delta j < 0$). This can be associated with the CR. Since we can associate the two main features with the resonances, I conclude that they are the main drivers of the outward migration. It is not obvious from this figure, which of the resonances is dominant.

To determine, which of the resonances is dominant I perform a modified resimulation of the strong model. I change the initial radial distribution of test particles to be a normal distribution centered around the two resonances, CR and OLR with a standard deviation of $0.2\,\mathrm{kpc}$. I sample $10^5$ particles in each case. All other parameters are

identical to those given for the strong model in table 3.1.

Figure 3.13 shows histograms of the last peri- (top panel) and the last apocenter distance (bottom) of the test particles. The thick blue and red histograms correspond to the particles centered around the CR and OLR respectively. The thin histograms show the distribution of the corresponding initial radii. The figure shows that the pericenter positions of the particles do not significantly differ from the particles' initial radii. A large fraction of the particles' apocenter distances, however, evolve to quite large values.

At intermediate radii (4-6 kpc) particles, initially at the OLR, outnumber the particles, initially at the CR. However, this excess is biased as the particle density at the OLR and CR are the same in this toy model. In real galaxies the particle density decreases with radius. For realistic values of the disk scale length the particle density at the OLR is overestimated by no more than a factor of three. Thus, even with correcting for this, the particles in resonance with the OLR will still dominate over those from the CR at these radii. At larger radii the distribution of the last apocenter distances is clearly dominated by particles originating from the CR. I conclude that the excess of particles in the outer disk is caused by particles in resonance with the CR and the OLR. However, the CR is more efficient at scattering particles to very large radii.

Figure 3.13 also shows that a lot of particles of the strong simulation that are in CR with the perturbation have apocenter distances which are much larger than their pericenters. This means that they experience severe radial heating, indicating that the approximation of Sellwood and Binney (2002, equation 1.9) breaks down for such a strong perturbation. This is also evident in the altered radial surface density profile (figure 3.11). Sellwood and Binney (2002) showed that migrating particles in resonance with a weak perturbation exchange orbits with another particle resulting in an unchanged global profile (section 1.7.2). In the case of these toy models, only the weak case seems to agree with this result of Sellwood and Binney (2002).

I note that in the idealized toy model all the orbits stay bound to the region of the perturbation. As long as the perturbation persists, they may also return to their original orbit. In fact, the radial position of the particles show a beat pattern. These are however not synchronous among the different particles such that the global radial distribution of the particles will eventually reach an equilibrium distribution. It takes about a Hubble time for such an equilibrium distribution to be reached in this toy model.

In the simulations, the scattered outer disk stars also stay bound to the bar (top panel in figure 3.5). The situation in the simulations is more complex though, e. g. the angular momentum changes even when the stars are far away from the bar region. As a result, the star particles' orbits do not show a clear beat pattern. A consequence
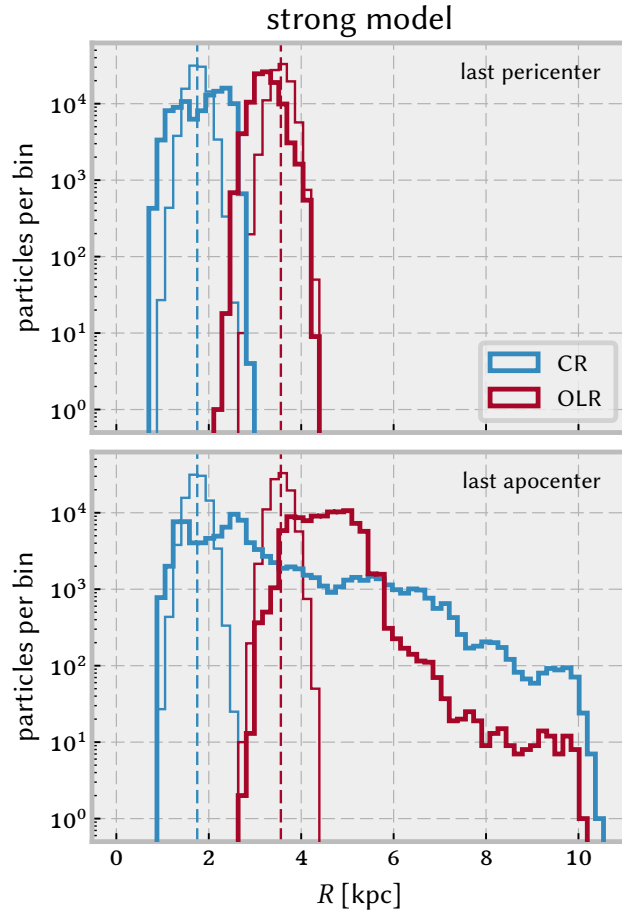
**Figure 3.13:** The distribution of last peri- (top panel) and apocenters (bottom) for the strong model. The thin histograms show the initial radial distribution of particles on a circular orbit centered around the CR (blue) and the OLR (red). The corresponding thick histograms show the respective distribution of the particles' last peri- (top) and apocenter (bottom). For a significant fraction of the particles the apocenter is much larger than the pericenter, indicating significant radial heating. At intermediate radii ($4$-$6\,\mathrm{kpc}$) the heating is dominated by the OLR, at larger radii by the CR.

is that the star's usually never return to their birth orbit.

### 3.4.4 Conclusions from the Toy Model

I demonstrate here that a strong, non-axisymmetric, steady, and rotating perturbation can cause significant radial heating at the CR. As a consequence, the radial density profile of a disk can change significantly for such a strong perturbation. This is in qualitative agreement with the properties of the low spin simulation ($\lambda = 0.02$) I analyzed in sections 3.2 and 3.3. For the weak model there is no significant change in the radial profile and only very little heating—even at the OLR. In this case, the approximation of no radial heating at the CR holds and it agrees well with the results of Sellwood and Binney (2002).

Since I treat particles as test particles and ignore their self-gravity, this toy model is not self-consistent. Due to the way I set up the potential perturbation, the additional potential well of the perturbation at the OLR is shallower than that at the CR. This may limit the extent of radial heating, caused by the OLR, and thus it is likely to be underestimated.

Despite the possible underestimation of radial heating by the OLR, I show here that particles in CR or OLR with a strong rotating perturbation in the center experience significant radial heating. It is strong enough to alter the radial surface density profile of an initially exponential disk. This is incompatible with the results of Sellwood and Binney (2002) for weak perturbations which do not significantly alter the global profile of their simulated disks.

In the present case of a strong bar, however, the approximation of a weak perturbation (Sellwood and Binney 2002) is violated. Hence, the result that particles in CR do not experience radial heating no longer holds. This approximation is based on the fact that at the CR the slope of the trajectory in the Lindblad diagram is equal to that of the circular velocity curve (figure 1.4). If the change in angular momentum due to the interaction with the perturbation is strong enough, the particle may depart from the circular velocity curve (or increase its distance to that). This results in radial heating and appears to be what happens in the strong model and in the simulations that produce Type-III disk breaks, given that these are the simulated galaxies with strong bars (figure 3.6).

Due to the lack of self-consistency and the non-axisymmetric external potential, the global angular momentum of the test particles is not necessarily conserved (see figure 3.12). This may lead to an underestimation of inward migration in the toy model which would naturally occur due to global angular momentum conservation. Nevertheless, the model does demonstrate the capability of such a perturbation to alter the global mass distribution of a stellar disk.
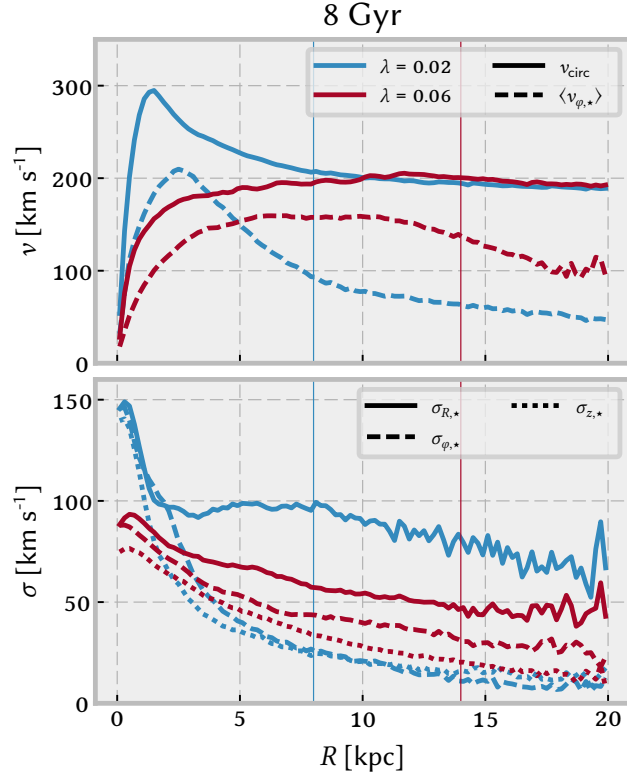
**Figure 3.14:** The upper panel shows the mean tangential velocity of stars (dashed lines) in annular bins and the circular velocity curve (solid lines). The lower panel shows the velocity dispersion in radial (solid), tangential (dashed) and vertical (dotted) direction. The vertical lines indicate the location of the breaks.

## 3.5  Observational Tests

In this section, I present some observational signatures of the mechanism described above. I compare the disk dynamics of a simulated Type-III disk (low-spin, $\lambda = 0.02$) to that of a Type-II disk (high-spin, $\lambda = 0.06$).

I show that the eccentricity distribution of the outer disks in the simulations with Type-II and III disk breaks is significantly different (cf. section 3.1.2). This leads to distinct dynamical properties of the disks that can be observed.

The upper panel of figure 3.14 shows the mean tangential velocity profile $\langle v_\varphi \rangle (R)$ of the stellar disks (dashed lines) for the low-spin ($\lambda = 0.02$, blue) and high-spin ($\lambda = 0.06$, red) galaxies. They are compared to the expected tangential velocities for

circular orbits (solid lines). As the stellar disks hosts stars on non-circular orbits, we expect the mean tangential velocity to be smaller than the circular velocity because stars at apocenter have low velocities. The effect is much stronger for the low-spin galaxy which exhibits a discrepancy by a factor of 4 in the entire outer disk. For the high-spin galaxy, the mean tangential velocity is only off by a factor of up to 2. This trend of decreasing tangential velocities in the outer disks with decreasing spin is expected as the distribution of circularity parameters shifts towards more eccentric orbits for the low-spin simulations.

The difference between the tangential velocity profile and the circular velocity curve is difficult to observe because the circular velocity curve cannot be observed easily. A better diagnostic for both types of disk breaks (Type-II and III) is the velocity dispersion profile as these can be observed. The velocity dispersion profiles in each direction are presented in the lower panel of figure 3.14. The prominent difference between both simulations is that the radial velocity dispersion in the $\lambda = 0.02$ (Type-III profile) disk is much higher than the tangential and vertical component. This is a signature of the large amount of eccentric orbits in these disks. In the disk with a Type-II break, all velocity dispersion components are comparable as it hosts a much smaller number of stars on eccentric orbits.

The resulting Type-III disk is dynamically peculiar. While it has as disk shape (figure 2.2), it is very slowly rotating and has an excess in radial velocity dispersion and, thus, the rotational contribution to support the disk is unusually small.

Observing these signatures is challenging as the outskirts of Type-III disks are very faint (>27 mag arcsec$^{-2}$). Thus, they are not observable through stellar absorption-line spectroscopy, even with integral field spectroscopy. A possible way to measure the kinematics of the outskirts of such disks would be to observe planetary nebulae. Planetary nebulae have been used previously to measure velocity dispersions of galaxies at very low surface brightness (e. g. Douglas et al. 2000; Herrmann and Ciardullo 2009) and, thus, would provide a possible tool to observe an excess of radial velocity dispersion, the smoking gun of stars surfing in the bar's potential.

## 3.6 Discussion

I presented a thorough analysis of stellar orbit evolution in one of the simulated disks from chapter 2 with a Type-III break. The goal was to identify a mechanism that produces Type-III breaks via secular evolution. I chose a simple simulation setup of disk formation within non-cosmological isolated halos to have full control over the halo spin and to facilitate the identification of secular, i. e. internal, mechanisms.

I show that the stars, which make up the outer parts of these Type-III disks, are

born on near-circular orbits well inside the final break radius (figure 3.2 and section 2.3). Furthermore, the stars in the outer parts of these disks have very eccentric orbits. Therefore, the mechanism that produces Type-III disks is inconsistent with that found by Roškar et al. (2008a). They found that the stars, which populate the truncated region of Type-II disks, have been churned there from their birth radii while retaining near-circular orbits. Instead, there has to be a mechanism that is able to drive stars to larger radii and that can turn those stars' orbits from circular to eccentric in my low-spin simulations.

I investigated the bar as a potential cause for the formation of Type-III profiles because the two simulations that form Type-III disks have significantly stronger bars than all other simulations of the sample (figure 3.6). I find that the increase of orbital radii (or more accurately their semi-major axes) is driven by an increase in orbital energy (figure 3.5) which, in turn, is driven by encounters of the stars with the bar potential at their pericenters. The main argument for the bar as the dominant cause is the fact that the ensemble of orbits of stars, that make up the outer disk, show a clear signature of the bar: the distribution of the ratio $\Delta e/\Delta j_z$ peaks at the value of the bar's pattern speed (figure 3.10). This is a clear signature that is expected from a rotating bar (equation (1.8), see also Sellwood and Binney 2002) with a constant pattern speed (figure 3.8).

Roškar et al. (2008a) found that radial migration in simulated galaxies with Type-II breaks is dominated by churning of stars on near-circular orbits. This preserves the stars' circularity, and thus does not cause significant radial heating. I find that these results are consistent with my simulations with Type-II profiles. However, in my simulated low-spin galaxies, which feature strong bars, the stars in CR with the bar may experience radial heating. This is possible because the churning mechanism is based on a first order approximation for moderate perturbations, which states that stars in CR do not experience radial heating. This first order approximation breaks down for the strong bars in my simulations. Here the stars may be driven away from the circular orbit curve while in CR with the bar. The heating of orbits by bars has been known for decades (Hohl 1971) but has never been linked to the formation of Type-III stellar disk profiles.

I confirm the interpretation of the simulations with the help of a simple toy model, which qualitatively mimics the situation in the simulations. I show that a strong bar-like perturbation may scatter stars to large radii in a very similar fashion as the bar in the low-spin simulations. An excess of stars at large radii can be reproduced in this model with a strong perturbation but not in a model with a weaker perturbation (figure 3.11), which is in qualitative agreement with the results from the simulations.

As of now, the literature only provided models that associate environmental effects (satellites, accretion) with the formation of Type-III disks. As this work presents a

mechanism that is capable of producing these disks in simulations of isolated galaxies, I show that galaxies can form Type-III disks purely via secular evolution. This does not preclude that external forces (Younger et al. 2007; Kazantzidis et al. 2009; Roediger et al. 2012; Borlaff et al. 2014) or other internal processes may also play a role.

I find that the initial halo spin matters as it locally sets the rate, at which stars form. This, in turn, determines the size of the stellar disk and its central surface density. Hence, it also sets the strength and longevity of any bar at the center. This effect cannot be explored in simulations with prepared disks (e. g. Foyle et al. 2008). For high spin parameters the gaseous disk is very extended but the gas surface density is comparatively low. This leads to more extended star formation at a rather low rate. In low-spin halos, the opposite happens. Due to the large amount of low angular momentum gas, a large portion of this gas is able to settle at low radii forming a concentrated massive gas disk with a high star formation rate (Kennicutt 1989, 1998). In this case, a massive and concentrated disk forms, which is highly susceptible to disk instabilities, and thus very prone to bar formation (Toomre 1964; Hohl 1971). Since the stellar mass density in the center is very large, the bar is also very massive. As I show in this work, this massive bar is driving the formation of Type-III disks.

In chapter 2, I reported a correlation between disk scale length and the type of truncation (middle panel of figure 2.4), i. e. the inner scale lengths increase from compact disks for type-III profiles through intermediate scale lengths for type-I profiles and extended disks for type-II profiles. While Maltby et al. (2012a) and Head et al. (2015) do not find such a correlation in their galaxy samples, Gutiérrez et al. (2011, section 5.2) report a trend that qualitatively agrees with my simulations. Gutiérrez et al. (2011) cannot rule out a common distribution for the inner scale lengths of type-I and II disks but find that Type-III disks have significantly shorter inner scale lengths compared to pure exponentials. Despite this qualitative agreement between a subset of observational data and my simulated galaxies, it is not the goal of this project to reproduce previous observational results but to take a first step to a possible explanation of the formation of Type-III disks, which relies purely on secular stellar dynamics.

It is important to stress that I do not claim the proposed mechanism to be exclusively responsible for the existence of Type-III disks. Instead, I show that the proposed mechanism is potentially capable of producing Type-III disks and characterize its dynamical signature, which can be used to observationally verify or falsify this model. The eccentric orbits of the stars in the outskirts of Type-III give rise to very unusual properties of a stellar disk: While being flat, the outer disk rotates very slowly and its velocity dispersion is dominated by the radial component. Minchev et al. (2012) find similar kinematic signatures in Type-III disks, which form through external gas accretion. This degeneracy does not undermine the potential capability of falsifying

this model if no Type-III disks with bars can be found that have a strong excess in radial velocity dispersion in their outskirts.

## 3.7  Summary

Analyzing controlled disk-galaxy simulations, I show that strong bars can form anti-truncated breaks in the radial surface density profile of stellar disks (Type-III disks). Strong bars can boost the semi-major axis of stellar orbits to very large galactocentric distances, while also changing the distribution of orbit circularity of the affected stars. The initial distribution of stars, which later comprise the outskirts of a simulated Type-III stellar disk, was initially dominated by near-circular orbits at smaller radii. In the final distribution of these stars' orbits, near-circular orbits are almost completely absent. It is dominated by very eccentric orbits. This bar-induced transformation of orbits has the capability of changing the global radial mass distribution of the stellar disk, ultimately leading to a Type-III break in the radial surface density profile.

This process is not efficient for disks with weak bars. In this case the dominant radial migration mechanism is spiral-induced churning and the disks form Type-II breaks in their radial profile. The reason is that the first order approximation of only very little or no radial heating holds only for weak but not for strong bars.

# 4 The Radial Stellar Density Profile of Maximum-Entropy Disks

The projects presented in the previous chapters show how disk breaks can be reproduced in simulations of isolated galaxy formation. In this chapter, I turn to a very different approach and try to explain why practically all stellar disks feature a near-exponential (Type-I) surface density profile (section 1.6.1 and Freeman 1970), at least of a significant radial range.

Based on an idea by my supervisor Hans-Walter Rix and our collaborator Scott Tremaine, I use a maximum-entropy approach to derive an analytic formula for stellar surface density profiles and show that the prediction agrees reasonably well with observational results and the simulations from the previous chapters. The content of this chapter has just been accepted for publication in a peer-reviewed astrophysical journal on February 6, 2017. A preprint of this paper is already available (Herpich et al. 2017). The coauthors, Scott Tremaine and Hans-Walter Rix, have done some significant text editing in the paper, especially in section 4.2.

Here, I replaced the introductory section of the paper (section 1) with a short section (4.1) in which I summarize the content of the introduction from the paper, which I did not cover in the introduction chapter of this thesis (section 1). I also omit the appendix of the paper which has been written completely by Scott Tremaine and presents work done by him that complements the content of the paper. I do refer to the appendix at the appropriate points in the text.

The rigorous derivation of the universal angular momentum distribution (equation (4.11)) was done with substantial help from my co-authors and from Matthias Bartelmann. All other results that are presented in this chapter are based on research performed by me.

## 4.1 The Fundamental Principle of the Model

When applied to self-gravitating stellar systems, the concepts from statistical mechanics have proven to be problematic. The most important reason for the failure of statistical physics to describe these systems is that a surface of constant energy in

phase-space cannot enclose a finite volume (see Binney and Tremaine 2008, section 7.3). However, here we argue that maximizing a suitably defined entropy *can* describe the angular momentum distribution of a stellar disk in an external potential. The methods to derive this angular momentum distribution are completely analogous to deriving the Boltzmann distribution for ideal gases.

The mechanism of radial migration is capable of exchanging the orbital angular momentum of particles. This can be very efficient, conserves a disk's total angular momentum and does not excite vertical or radial motions (section 1.7.2).

For the sake of simplicity we adopt very idealized but sensible assumptions that allow for a rather simple analytic treatment.

1. We assume stars to be born on perfectly circular orbits. Of course, this assumption is not perfectly satisfied in real stellar disks. Galactic gas disks are, however, fully rotationally supported and orbit with little eccentricity. Since new-born stars inherit the dynamics of their parent gaseous material, this assumption should be a good approximation.

2. Radial migration is arbitrarily efficient in shuffling the angular momenta of disk stars and may lead to a thermodynamic equilibrium state in angular momentum space.

3. The radial migration-mediated shuffling of angular momenta preserves the perfectly circular orbits.

The assumption of perfectly circular orbits allows for a bijective mapping from orbital angular momentum space to spatial galactocentric distance space of the orbits.

## 4.2  Modeling Maximum Entropy Disks

### 4.2.1  Choice of Phase-Space Variables

We work in cylindrical coordinates $\boldsymbol{r} = (R, \varphi, z)$ and use action-angle variables $(\boldsymbol{J}, \boldsymbol{\theta}) = (J_R, J_\varphi, J_z; \theta_R, \theta_\varphi, \theta_z)$ as phase-space coordinates (Binney and Tremaine 2008). Action-angle variables are canonical so $\mathrm{d}\boldsymbol{\theta}\,\mathrm{d}\boldsymbol{J} = \mathrm{d}\boldsymbol{r}\,\mathrm{d}\boldsymbol{p}$ where $\boldsymbol{p}$ is the ordinary Cartesian momentum conjugate to $\boldsymbol{r}$. Since stars are born on nearly circular, coplanar orbits and migration does not excite eccentricities or inclinations (see section 1.7.2) we may assume that $J_R = J_z = 0$. The azimuthal action $J_\varphi$ is equal to the angular momentum per unit mass along the $z$-axis, $j$, and we can restrict ourselves to the two-dimensional manifold in phase space $(J_\varphi, \theta_\varphi)$. The angle variables $\theta_\varphi$ are uniformly distributed so the state of a disk of $N$ stars is fully specified by the angular momenta $(j_1, \dots, j_N)$. Since

$N \gg 1$ and the stars interact weakly, the state of the disk is also fully described by the one-particle distribution function $F(j)$, where $F(j) \, \mathrm{d}j \, \mathrm{d}\theta_\varphi$ is the number of stars in a phase-space element $\mathrm{d}j \, \mathrm{d}\theta_\varphi$.

Since migration is driven by transient spiral arms and other structures much more massive than stars, there is no mass segregation during migration and with no loss of generality we can assume that all stars have the same mass $m$.

### 4.2.2 Defining the Entropy

The central premise of this project is that radial migration scrambles the individual angular momenta of disk stars. Ultimately, this will result in a distribution of stars in the $N$-dimensional space with coordinates $(j_1, \dots, j_N)$ that is uniform on the manifold allowed by the conserved quantities (the total number of stars and the total angular momentum; see section 4.2.3). This is simply the ergodic hypothesis that underlies the construction of the microcanonical ensemble in classical statistical mechanics. Then standard arguments show that if $N \gg 1$ and the interactions are weak, the relative probability $\Omega$ associated with the distribution function $F(j)$ is given by $\log \Omega = S + \mathrm{const}$ where [1]

$$S = - \int \mathrm{d}j \, \mathrm{d}\theta_\varphi \, F(j) \log F(j) = -2\pi \int \mathrm{d}j \, F(j) \log F(j) \tag{4.1}$$

is the Boltzmann entropy, and we have set Boltzmann's constant to unity.

Applying equilibrium statistical mechanics to this problem implicitly assumes that radial migration is efficient enough to completely scramble stellar orbits across the whole radial range of the disk, and does so on a timescale short compared to the age of the galaxy. We caution that this premise cannot be strictly true, since that would produce a stellar disk without abundance or age gradients (see also the discussion in section 4.5.2).

### 4.2.3 Conserved Quantities

**Total Number of Stars**

We assume that the number $N$ of stars in the disk is fixed, thus

$$N = 2\pi \int \mathrm{d}j \, F(j) = \mathrm{constant}. \tag{4.2}$$

---

[1] Divide the range of angular momentum $0 \leq j \leq j_{\max}$ into $K$ cells of equal width $\Delta j = j_{\max}/K$. Suppose there are $n_k$ stars in cell $k$, with $\sum_{k=1}^{K} n_k = N$. The probability of this configuration is $\Omega \propto N! / \prod_{k=1}^{K} n_k!$. Set $n_k = 2\pi F(j_k)\Delta j$ and assume $n_k \gg 1$ so the factorials can be evaluated using Stirling's approximation $\log n! = n \log n - n + \mathrm{O}(\log n)$. Finally assume $K \gg 1$ so the sums can be replaced by an integral to obtain (4.1).

In fact, ongoing star formation is present in almost all disks, which exhibit the spiral structure that drives migration. However, by focussing our attention on the distribution of older stars (e.g., by measuring the surface brightness profile at red or infrared wavelengths), we can minimize contamination by recent star formation.

### Total Angular Momentum

We also assume that the total angular momentum $J$ of the disk is fixed, thus

$$J = N m \langle j \rangle = 2\pi m \int \mathrm{d}j \, j F(j) = \text{constant}. \tag{4.3}$$

The validity of this assumption may be limited by several processes.

A central bar can exert torques on the dark halo, which drain angular momentum from the disk. Such torques can be substantial but are difficult to estimate because the dark-halo density near the center of the galaxy is poorly determined (see Sellwood 2014, for a review). Typically, however, the effects of bar-halo torques are likely to be small since (i) the angular momentum of the bar is much less than that of the disk, because it has only a small fraction of the disk mass and a smaller radius of gyration; (ii) most bars have high pattern speeds (Sellwood 2014), which suggests that they have not lost much of their original angular momentum.

Spiral structure can also transfer angular momentum from the disk to the halo (Mark 1976; Fuchs 2004) but for plausible values of the pitch angle and amplitude of the spirals, the torques are too small to modify the disk angular momentum significantly. This would be true even if (unrealistically) the strong "grand-design" spiral patterns seen in some galaxies survived unchanged for a Hubble time (Tremaine and Ostriker 1999).

Galaxy disks continuously build up angular momentum as they grow by accretion. This process violates our assumptions of mass and angular momentum conservation. However, as long as radial migration is effective on a timescale shorter than that of the total mass and angular momentum change due to late-epoch gas infall, the approximations described here remain sensible.

In section 4.5.2, I discuss the validity of these assumptions in more detail.

**Energy**

The total potential energy of the disk can be written as

$$U = 2\pi \int dR\, R\Sigma_\star(R)\Phi_h(R)$$
$$+ 2\pi^2 \int dR\, dR'\, RR'\Sigma_\star(R)\Sigma_\star(R')W(R, R'). \tag{4.4}$$

Here $\Sigma_\star(R)$ is the surface density of the disk at radius $R$, $\Phi_h(R)$ is the gravitational potential due to the DM halo, and the kernel $W(R, R')$ is the gravitational potential between two coplanar rings of unit mass at $R$ and $R'$. Two expressions for this kernel are

$$W(R, R') = -\frac{2G}{\pi(R + R')} K\left(\frac{2\sqrt{RR'}}{R + R'}\right),$$
$$= -\frac{2G}{\pi R_>} K\left(\frac{R_<}{R_>}\right), \tag{4.5}$$

where $K$ is a complete elliptic integral and $R_<$ and $R_>$ are, respectively, the smaller and larger of $R$ and $R'$. The gravitational potential in the disk plane is

$$\Phi(R) = \Phi_h(R) + 2\pi \int dR'\, R'\Sigma_\star(R')W(R, R') \tag{4.6}$$

and the kinetic energy of the disk is

$$T = \pi \int dR\,\Sigma_\star(R)R^2 \frac{d\Phi}{dR}. \tag{4.7}$$

The surface density is related to the distribution function by

$$\Sigma_\star(R) = \frac{m}{R}F(j)\frac{dj}{dR}, \tag{4.8}$$
$$j^2(R) = R^3 \frac{d\Phi}{dR}. \tag{4.9}$$

We have chosen not to include a constraint that the total disk energy is conserved, for two reasons. First, spiral structure requires gas in the disk and hence dissipation. Without dissipation, transient spirals heat the disk and quench the formation of further spirals (Sellwood 2014). Thus we do not expect the energy of migrating disks to be conserved. Second, an energy constraint would add an extra free parameter to

our models and our intent is to explore the simplest possible models for maximum-entropy disks.

Nevertheless, the disk's total energy does play an important role. Maximum-entropy disks are a possible end-state of migration only if they have lower energy than other disks with the same mass and angular momentum. Scott Tremaine showed that this is likely to be the case. The corresponding arguments are presented in Appendix A of Herpich et al. (2017).

### 4.2.4  A Universal Angular Momentum Distribution

The maximum-entropy state, consistent with a fixed number of stars $N$ and fixed total angular momentum $J$, can be determined with the concept of Lagrange multipliers through the variational equation

$$
\begin{aligned}
0 = {} & \delta S - \alpha \delta N - \beta \delta J \\
= {} & -2\pi \int \mathrm{d}j \, \delta F(j) \left[ \left(1 + \log F(j)\right) + \alpha + \beta j \right],
\end{aligned}
\tag{4.10}
$$

where $\alpha$ and $\beta$ are the Lagrange multipliers. $F(j) = \exp(-1 - \alpha - \beta j)$ solves this equation. Substituting back into equations (4.2) and (4.3), it is straightforward to determine $\alpha$ and $\beta$ and rewrite the distribution function as

$$
F(j) = \frac{N}{2\pi\langle j\rangle} \exp\left(-j/\langle j\rangle\right),
\tag{4.11}
$$

where $\langle j\rangle$ is the mean specific angular momentum. Equation (4.11) encapsulates a remarkable result: given our assumptions, the maximum-entropy distribution of specific angular momentum of a stellar disk is always exponential, independent of the actual gravitational potential that determines the rotation curve. I now translate this distribution into surface density profiles.

## 4.3  The Surface Density Profile of Maximum Entropy Disks

To compare the maximum-entropy distribution function (4.11) to observations for a given rotation curve $v_\mathrm{c}(R)$, I need to relate the surface density $\Sigma_\star(R)$ to the distribution function $F(j)$. Circular orbits are stable if, and only if, the angular momentum increases with radius, so $v_\mathrm{c}(R)$ defines a bijective mapping between $j_z$ and $R$ through the equation

$$
j_z(R) = R v_\mathrm{c}(R).
\tag{4.12}
$$

Moreover, rotation curves are generally smooth (Berrier and Sellwood 2015) so the mapping is well-behaved.

I can then compute the surface density profile from equations (4.8) and (4.11),

$$\Sigma_\star(R) = \frac{mN}{2\pi R \langle j \rangle} \exp\left[-\frac{R v_c(R)}{\langle j \rangle}\right] \left[v_c(R) + R\frac{dv_c}{dR}\right]. \tag{4.13}$$

An more intuitive form is

$$\Sigma_\star(R) = \frac{M}{2\pi R R_e(R)} \exp\left[-\frac{R}{R_e(R)}\right] \left(1 + \frac{d\log v_c}{d\log R}\right), \tag{4.14}$$

with $R_e(R) \equiv \langle j \rangle / v_c(R)$ and $M \equiv Nm$ the total mass of the disk.

For a flat rotation curve, ($v_c(R)$ = constant) $R_e$ is independent of radius and we have

$$\Sigma_\star(R) = \frac{M}{2\pi R_e^2} \cdot \frac{R_e}{R} \exp\left(-\frac{R}{R_e}\right). \tag{4.15}$$

Then, the surface density is an approximately exponential function of radius for $R \gg R_e$, and is $\propto R^{-1}$ for $R \ll R_e$. Alternatively, we may ask for what rotation curve the maximum-entropy angular momentum distribution (4.11) has a Type-I surface density profile, $\Sigma_\star(R) \propto \exp(-R/R_{\exp})$. It is straightforward to show that in this case

$$v_c(R) = v_\infty \left[1 - \frac{R_{\exp}}{R} \log(1 + R/R_{\exp})\right], \tag{4.16}$$

where $v_\infty \equiv \langle j \rangle / R_{\exp}$ is the circular speed at large radii.

In this analysis, we have derived the angular momentum distribution under the condition of a maximal entropy (equation (4.11)). Starting from that result and the assumption of circular orbits, I translate this distribution into a surface density profile for a given galactic rotation curve. The functional form of the rotation curve is determined by the combined gravitational field of the DM halo and the stellar disk. The gaseous disk usually also contributes to it.

Scott Tremaine describes the special case of a stellar disk that is not hosted by a DM halo. Then, the gravitational potential is set by the stellar disk only. He treats this system in a fully self-consistent manner. The results are presented in Appendix B of Herpich et al. (2017). In this case, an analytic expression for the surface density profile can only be determined for very large and very small radii. For the former case it varies as $\exp[-(R/R_0)^{1/2}]$ and for the latter as $R^{-1}$. It is in principle possible to calculate the fully self-consistent case for a disk in a DM halo. Then, the surface density profile, the halo density distribution, and the rotation curve as a result of efficient migration have to be calculated, taking into account the combined potential that each component generates. This is much more difficult and beyond the scope of this thesis (see the discussion in section 5.3).

## 4.4 Tests of the Model

### 4.4.1 Comparison with Observational Data

I now ask, whether observed surface density profiles of disk galaxies match the prediction from equations (4.11) or (4.13). To do so, I consider the circular-velocity curve, or rotation curve, $v_c(R)$ and the surface brightness profile $I(R)$ for a set of disk-dominated galaxies. I assume that the stellar mass-to-light ratio Y is independent of radius so $I(R) \propto \Sigma_\star(R)$, although the actual value of Y is not needed. This assumption is reasonable if observations at red (optical) bands are available, as population and dust extinction gradients have only modest impact (van der Kruit and Freeman 2011).

I use a set of 304 disk galaxies with $r$-band surface brightness profiles and H$\alpha$ rotation curves from Courteau (1996, 1997)[2]. Courteau (1997) also provides fitting functions and best-fit parameters for the rotation curves, which I use to derive a smooth approximation to $v_c(R)$. I use Courteau's Model 2, which fits the rotation curve to the form

$$v_c(R) = v_m(1 + R_t/R)^\beta/(1 + R_t^\gamma/R^\gamma)^{1/\gamma}. \tag{4.17}$$

There are four fitting parameters, $v_m$, $r_t$, $\gamma$, and $\beta$, but $\beta$ is set to 0 for most of the galaxies. See the paper for more detail.

Based on these data, and the assumption of circular orbits, I can calculate $F(j)$ using equations (4.8) and (4.12). I then fit $\log F(j)$ to the logarithm of the exponential form from equation (4.11) using a set of 60 equally spaced angular momenta $\{j_k\}$ and assuming equal weights for each point[3]. The free parameters determined by the fit are the normalization and the mean angular momentum $\langle j \rangle$. For the fit I use equal weights for every data point.

Figure 4.1 shows the stacked specific angular momentum distributions of all the galaxies in the sample in the normalized coordinates $j/\langle j \rangle$ and $2\pi\langle j \rangle F(j)/N$. The blue straight line represents the prediction for maximum-entropy disks, equation (4.11). The angular momentum profiles reconstructed from the data are broadly consistent with the predictions over much of the $j$-range. Only for $j \lesssim \langle j \rangle$ are there some systematic deviations from the prediction. These could arise from contamination by bulge components or because the model assumption of circular orbits breaks down at small radii. Note also that a number of *individual* galaxies are clearly not consistent with our model, while others show almost perfectly exponential specific angular momentum distributions—this is seen more clearly in figure 4.3. These results

---

[2]The data are available at `http://www.cadc-ccda.hia-iha.nrc-cnrc.gc.ca/COURTEAU/`. Some galaxies have more than a single data set, in which case I choose the first one.

[3]To realize equally spaced $\{j_k\}$, I interpolate the data which provide measurements for equally spaced spatial values.
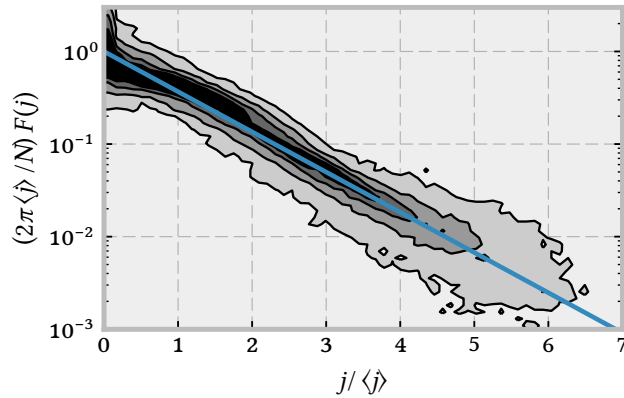
**Figure 4.1:** The distribution of specific angular momentum stacked for 304 disk galaxies from Courteau (1996, 1997). Every distribution has been rescaled using two fit parameters (normalization and $\langle j \rangle$). The contours enclose 40, 60, 80 and 95% of the plotted data points. The blue line is the maximum-entropy distribution (equation 4.11). Despite some small but systematic deviations for small $j$ there is good agreement with the model prediction.
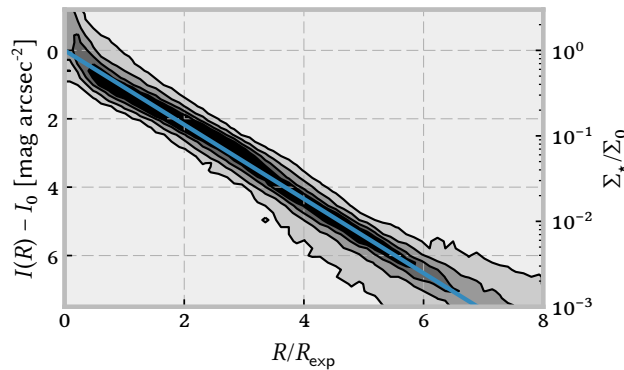


**Figure 4.2:** Stacked surface brightness profiles for 304 disk galaxies from Courteau (1996, 1997). The profiles have been rescaled using two fit parameters (normalization and $R_{\text{exp}}$), determined by fitting to a Type-I disk. The contours enclose 40, 60, 80 and 95% of the plotted data points. The blue line represents a purely exponential disk. The agreement is similar to that of the fit to the angular momentum distribution in figure 4.1.

suggest that more factors than radial migration play a role in establishing the angular momentum profile, at least in some galaxies.

For comparison, in figure 4.2, I show the stacked surface brightness profiles from the galaxies in Courteau (1996, 1997), rescaled by a fit to the usual exponential disk,

$\Sigma_\star(R) = \Sigma_0 \exp(-R/R_{\mathrm{exp}})$. The fitting procedure is identical to that for the angular momentum distribution. The overall agreement, and the scatter, are very similar to that of the fit to the angular momentum distribution in figure 4.1. A more quantitative comparison in figure 4.4 confirms this result.

A different approach is to use the rotation curve from Courteau (1997) to calculate the expected stellar surface density according to equation (4.13). This defines a function with two free parameters, $\langle j \rangle$ and a normalization constant, which can be fitted to the observed surface brightness data from Courteau (1996). I use standard $\chi^2$-minimization with data points weighted by the inverse error in the surface brightness data. This procedure ignores errors in the rotation-curve data and fits. The innermost data point at $R = 0$ is not included in the fit, because the surface brightness data from (Courteau 1996) do not state errors for this data point.

In figure 4.3, I show the fits for fifteen galaxies randomly selected from the full sample. The top panel for each galaxy contains the rotation-curve data (blue points and error bars) along with the Model 2 fit (red line) from Courteau (1997). The bottom panel shows the corresponding surface brightness data with the best-fit maximum-entropy profile, using the same color scheme. Some of the surface brightness profiles are fitted remarkably well (e.g., UGC 10536). Most of the profiles are fit well in the central regions. However, many of the profiles fall below the maximum-entropy fit at large radii, possibly because migration operates slowly at large radii and the disk has not had time to approach a maximum-entropy state. For about one in four of the galaxies, both in figure 4.3 and in the full sample of 304 galaxies, the profile in the center is also not reproduced very well.

I also compare the model to the exponential Type-I disk profile. I fit the parameters $\Sigma_0$ and $R_{\mathrm{exp}}$ for each of the galaxies in the sample, again assuming the same weights (inverse error) per $\log \Sigma_\star$. In figure 4.4, I show a scatter plot of the respective $\chi^2$ values for the two fits, which each involve two free parameters, a normalization and a scale. The figure shows that on average, the maximum-entropy model and the exponential model fit the data about equally well. Galaxies, which fit one model well, tend to fit the other and vice versa, although there is significant scatter. The difference is that the exponential model is empirical while the maximum-entropy model is motivated by general properties of the dynamics of disk evolution.

However, the $\chi^2$ values are generally much larger than the number of degrees of freedom, mostly because of two properties of the surface brightness profiles of galaxy disks: first, azimuthally averaged profiles often have bumps and wiggles due to spiral structure or other perturbations that are highly significant in a formal sense; second, profiles often show breaks at small and large radii that cannot be captured in the functional forms of either model (see figure 4.3). Clearly, the processes that set the disk profiles have aspects that are too complex to be captured by the simple
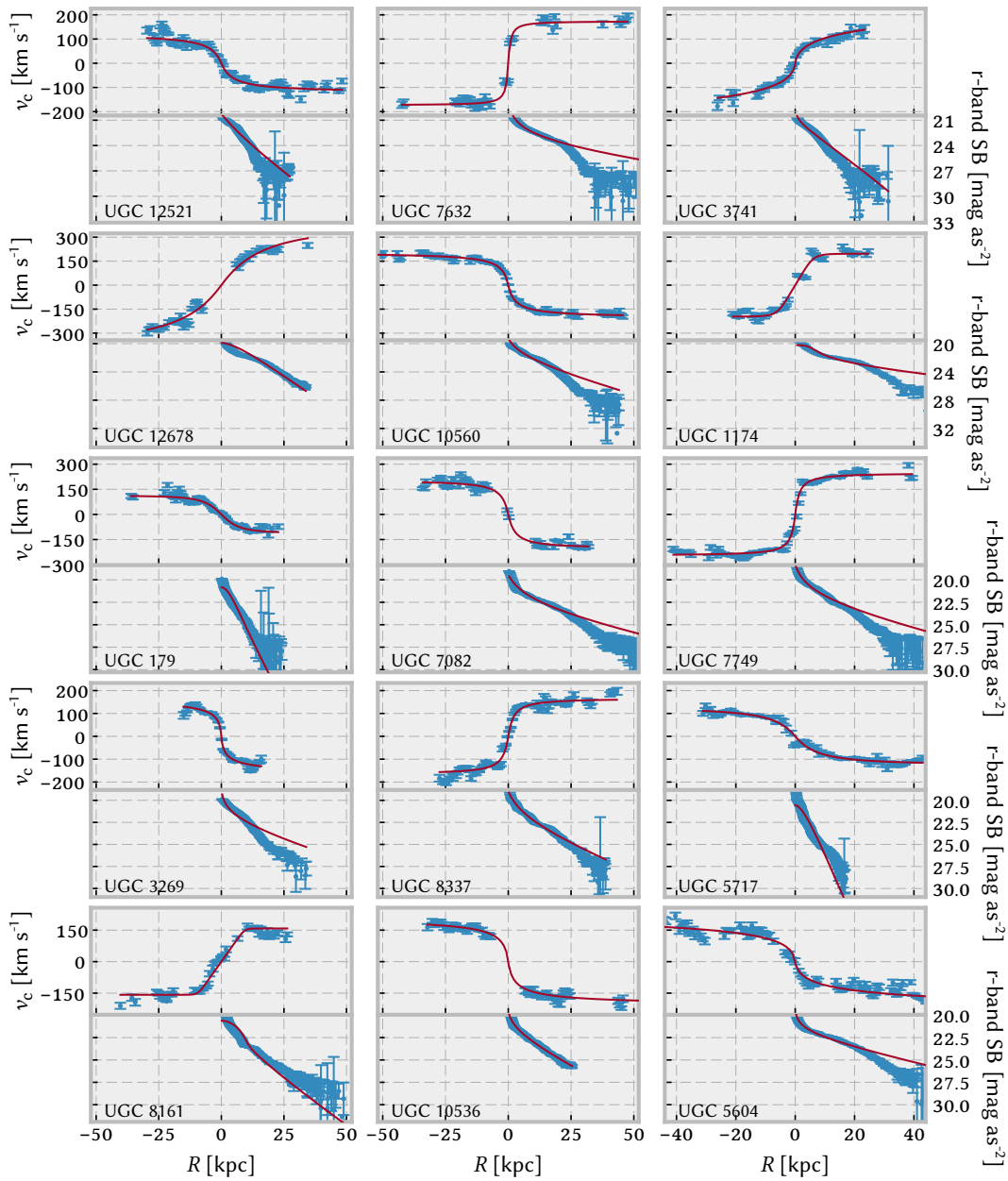
**Figure 4.3:** Model fits for 15 randomly selected galaxies from Courteau (1996, 1997). For each galaxy the top panel shows the measured rotation curve (blue) and the Model 2 fit from Courteau (1997, equation (4.17), red line). The bottom panel shows the measured surface brightness profile (blue) and the best-fit model profile for a maximum-entropy disk (red line) derived from the rotation curve from Courteau (1997) using equation (4.13) and the assumption of constant mass-to-light ratio Y. Distances are obtained from the redshifts assuming a Hubble constant of $H_0 = 70\,\mathrm{km\,s^{-1}\,Mpc^{-1}}$. See text for a description of the fitting procedure.
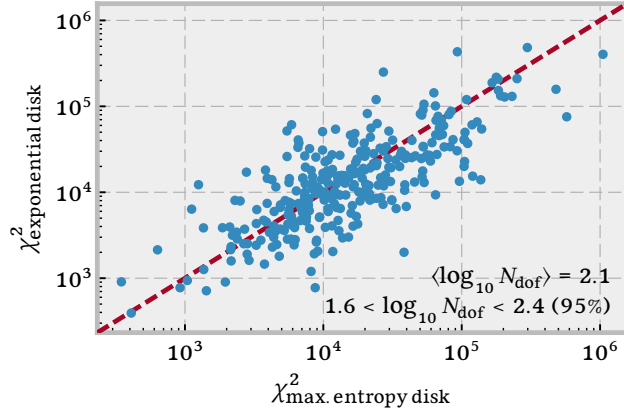
**Figure 4.4:** Scatter plot of $\chi^2$ values for fits to an exponential disk (vertical axis) and the maximum-entropy model (horizontal axis). The dashed line represents the locus of equal $\chi^2$ values for both models. $\chi^2$ values have been computed using the inverse of the error of the surface brightness data as weights for each data point. The average number of degrees of freedom is $\langle \log_{10} N_{\mathrm{dof}} \rangle = 2.1$, and 95% of the galaxies satisfy $1.6 < \log_{10} N_{\mathrm{dof}} < 2.4$. The maximum-entropy model and the exponential model fit the data about equally well.

maximum-entropy model.

## 4.4.2  Comparison with Simulations

Simulations of disk galaxy formation offer a controlled way to test whether galaxy disks evolve towards a maximum-entropy state. We use the first suite of hydrodynamical simulations with constant shape parameter for this purpose (see section 2.1.3). These simulations use non-cosmological environments, that is, they lack cosmological perturbations such as external torques, mergers, fly-bys, etc. Hence, they are well-suited to testing the predictions, which are based on the internal dynamical evolution of the disk (of course, for the same reasons they are not well-suited for exploring whether internal evolution or cosmological perturbations dominate the disk evolution in real galaxies). A characteristic of this particular suite of simulations is that the simulated galaxies with low initial halo spin have disks that are dominated by stars on eccentric orbits and those with high initial spin are dominated by stars on near-circular orbits (see also section 3.1.2). Thus, only the high-spin simulations satisfy our assumption of near-circular stellar orbits.

I calculate the circular-velocity or rotation curve in the simulations by differentiating the gravitational potential $\Phi(R)$ ($v_c^2 = R \, \mathrm{d}\Phi / \mathrm{d}R$). I also extract the total stellar
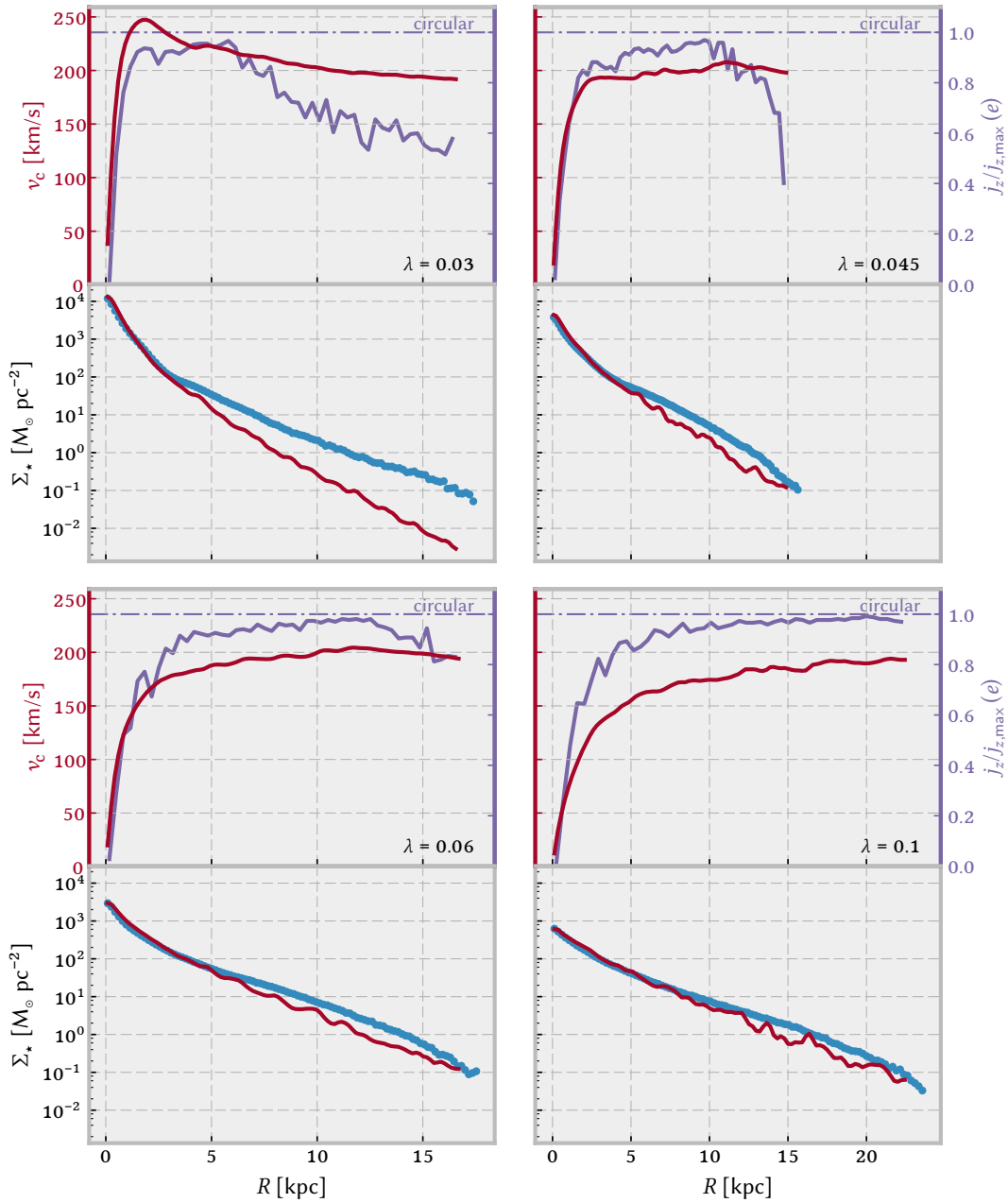
**Figure 4.5:** Comparison of maximum-entropy disks to the surface density profiles of a subset of simulated galaxies from chapters 2 and 3. For each of the simulated galaxies the upper panel shows the circular-velocity curve (red line, left axis), and the circularity parameter (purple line, right axis), both as a function of galactocentric radius $R$. The corresponding bottom panels show the stellar surface density profile (blue points) and the maximum-entropy profile (red line) based on equation (4.13). Note that there are no free parameters although in deriving the maximum-entropy model I use the known total mass and angular momentum of the disk. The wiggles in the predicted surface density profile are due to irregularities in the rotation curve which are amplified because the maximum-entropy surface density depends on the gradient $dv_c/dR$. The half-mass radius of each simulated galaxy is indicated by a vertical dashed line. The initial halo spin $\lambda$ of each galaxy is given at the bottom of the top panel. In general, disks with larger halo spin have larger circularity parameters outside the half-mass radius and give better agreement with the maximum-entropy model, which assumes circular orbits.

mass $M$ and the mean specific angular momentum $\langle j \rangle$ of each disk from the simulation. With these data, it is straightforward to predict the surface density profile of the maximum-entropy disk and to compare this to the actual surface density. The results are presented in figure 4.5. For each galaxy, the upper panel shows the circular-velocity curve (red) and the mode of the circularity parameter $j_z/j_{z,\mathrm{max}}(e)$ (purple). The corresponding bottom panels show the surface density profile as extracted from the simulations (blue points) and the prediction for a maximum-entropy model (red line). Note that these predictions have no adjustable parameters, but since I use the total mass and angular momentum from the simulation, these parameters are guaranteed to match the intrinsic values of the galaxy by construction.

For almost all galaxies, the inner part of the surface density profile is reproduced nicely by the maximum-entropy model. In the outer part of the disk, the agreement gets progressively better with increasing values for the halo spin parameter $\lambda$. The agreement for the lowest-spin galaxy ($\lambda = 0.03$) is poor in the outer region, while for the highest-spin simulation ($\lambda = 0.1$), the prediction follows the actual profile closely over the entire radial range. The lower-spin simulations might not represent realistic disk dominated galaxies, as their orbits are far from circular even at large radii (section 3.1.2). I infer that the maximum-entropy model provides a remarkably good match to the surface density profiles of simulated disk galaxies with near-circular orbits (or realistic radial velocity dispersions).

## 4.5  Summary

### 4.5.1  The Radial Profile of Maximum-Entropy Disks

Using arguments from equilibrium statistical mechanics, I derived an analytic expression for the stellar surface density profiles of disk galaxies. The profile of these "maximum-entropy" disks depends only on the underlying rotation curve and the total stellar mass and angular momentum. The derivation rests on several idealized assumptions:

- The disk is axisymmetric, thin, and cold, in the sense that the stellar orbits are near-circular and coplanar,

- the total mass and angular momentum of the stars are conserved (i. e. negligible ongoing star formation, mass loss or accretion, exchange of angular momentum with the halo, etc.),

- and there is a radial mixing mechanism that is efficient enough to distribute

the stars uniformly on the phase-space manifold allowed by the conserved quantities.

These are strong assumptions that certainly over-simplify the physics of real disk galaxies. Nevertheless, I have shown in section 4.4.2 that the model correctly predicts the surface density profiles of simulated galaxies, at least for isolated disks that are dominated by stars on near-circular orbits.

I have compared the surface density distribution in maximum-entropy disks to the expected profiles of 304 disk-dominated galaxies from Courteau (1996, 1997) given their rotation curves. This comparison requires deriving the angular momentum vs. radius relation and fitting the model to the total angular momentum and mass of the observed disks. I find that overall the maximum-entropy model fits about as well as the usual exponential disk (Freeman 1970), an empirical formula chosen to match the observations that has the same number (2) of free parameters. Only a few of the galaxies were completely incompatible with maximum-entropy models. The majority of the galaxies show a qualitatively sensible fit and a significant fraction of galaxies yield excellent consistency.

This match is very encouraging, as it suggests that the physics in the extremely simple and restrictive model plays an important role in determining the radial profiles of galaxy disks.

## 4.5.2 Model Limitations

It is worth reviewing the simplifying assumptions and approximations that I made when comparing the model to observations, which I now do. I have assumed that the disk stars are on circular, coplanar orbits, i.e., that the disk is dynamically cold and razor-thin. This is a reasonable first approximation: for edge-on disk galaxies the scale height normal to the disk midplane is approximately independent of radius and only $\approx 10\,\%$ of the scale length $R_{\mathrm{exp}}$ of the exponential disk that characterizes the radial distribution of mass in the disk (Peters et al. 2017). The typical radial velocity dispersion $\sigma_R$ in galaxy disks at $R_{\mathrm{exp}}$ is estimated to be only $30\,\%$ of the circular speed $v_{\mathrm{c}}$ in external galaxies (van der Kruit and Freeman 2011) and the ratio $\sigma_R/v_{\mathrm{c}}$ is even smaller at larger radii (in the solar neighbourhood the ratio is $\approx 20\,\%$).

However, these approximations are less good close to the center of galaxies and the comparison of the maximum-entropy model with simulations in section 4.4.2 suggests that it breaks down when the assumption of near-circular orbits is not met (see also Figure 4.5). This is a strong hint that the assumption of circular orbits is necessary.

To explore the effects of relaxing this assumption we may allow the stars to have

small but non-zero radial and vertical actions $J_R$ and $J_z$. Since these are adiabatic invariants they should be conserved by the slow interactions with transient spirals that drive migration (provided that the influence of the spirals is localized near the CR and does not extend to the Lindblad resonances, as appears to be the case). This expectation is consistent with N-body simulations, which show that the vertical and radial actions are approximately conserved even for stars that migrate (e. g. Sellwood and Binney 2002; Solway et al. 2012; Minchev et al. 2012; Vera-Ciro et al. 2016). If the radial and vertical actions are conserved, the maximum-entropy distribution function is $F(j, J_R, J_z) \propto G(J_R, J_z) \exp(-j/\langle j \rangle)$, where $G(J_R, J_z)$ is the initial distribution of the disk stars in $J_R$ and $J_z$. A more realistic approximation is to include slow growth in $J_R$ and $J_z$ due to scattering by giant molecular clouds and non-corotating spiral arms (Spitzer and Schwarzschild 1951; Julian and Toomre 1966; Carlberg 1987; Fouvry et al. 2015). Implementing these generalizations would be straightforward but that is beyond the scope of this thesis. It is noteworthy that the migration efficiency decreases as $J_R$ and $J_z$ increase (Sellwood and Binney 2002; Solway et al. 2012; Vera-Ciro et al. 2016) and it is possible, for example, that the disk is close to a maximum-entropy state only for stars on near-circular orbits.

In a strict sense, ongoing star formation in disks and infall of halo gas and minor mergers must violate the assumption of total mass and angular momentum conservation. Nonetheless, this approximation may be sensible for the purpose of this model. It is natural to assume that the timescales for mass ($\tau_M = M_\star/\dot{M}_\star$) and angular momentum ($\tau_J = J/\dot{J}$) buildup are similar, $\tau_M \approx \tau_J$. Then, if the migration time $\tau_{\mathrm{mig}} \ll \tau_{MJ}$, the disk will always be close to a maximum-entropy state although the surface density profile of this state will vary on a timescale $\tau_{MJ}$.

In a true maximum-entropy disk there should be no radial age or metallicity gradients. Consequently, there is some tension between this simple model and observations of metallicity and age gradients in disk galaxies. However, not all disk galaxies have significant gradients and those that do generally show only shallow gradients (Sánchez-Blázquez et al. 2014; Wilkinson et al. 2015; Goddard et al. 2016), which could persist even if the disks were close to maximum entropy. Moreover the youngest stellar populations are the brightest and therefore tend to dominate observed abundance gradients. Only stars with ages much longer than the migration time are expected to have a maximum-entropy distribution, and indeed the metallicity gradient in the Milky Way appears to be smaller for older stars (Yu et al. 2012). In general, the maximum-entropy disk profile with no gradients can be considered an asymptotic solution, which the disks approach but may not yet have achieved (Schönrich and McMillan 2016).

There is strong evidence that substantial radial mixing has occurred in the Milky Way (see section 1.7.2). So far the model is based on the assumption that a radial

mixing process exists that preserves circular coplanar orbits. Consequently it has to preserve radial and vertical actions of the orbits. The process of radial migration, induced by transient spirals (see section 1.7.2), is a suitable candidate because it operates on time scales smaller than one Hubble time and (approximately) preserves the radial action (Sellwood and Binney 2002; Roškar et al. 2012). To my knowledge there is no other plausible mechanism in disk galaxies that satisfies the above conditions.

The maximum-entropy approach presented here allows for computing the surface density profile of a stellar disk for a given rotation curve. It does not describe the underlying mass distributions (DM halo, disk, spheroid, gas) and how they give rise to the rotation curve of a galaxy. In particular, it does not explain what determines the respective mass distributions. As shown in Appendix B of Herpich et al. (2017) it is possible to calculate the mass distribution of a razor-thin stellar disk, which is not embedded in a DM halo, in a fully self-consistent manner, i. e. the underlying rotation curve is generated by the mass of the disk. Such a galaxy is inconsistent with the current paradigm of galaxy formation in the framework of the ΛCDM cosmological model (sections 1.1.3 and 1.5.1). In a given DM halo, the rotation curve and the maximum-entropy disk surface density profile can be computed, in principle, if one follows the response of the halo to slow changes in the mass distribution of the stellar disk (Blumenthal et al. 1986; Gnedin et al. 2004). However, in this case the result depends on the initial state of the disk and the halo. Accretion of DM and gas as well as ongoing star formation also play a role in the evolution of a galaxy. The angular momentum distribution would still obey the simple exponential shape in equation (4.11) but the rotation curve and surface density profile depend on the initial conditions and the cosmological context.

The model may not be applicable to low-mass disk galaxies for several reasons:

1. Turbulent velocities of the interstellar gas in low-mass galaxies are larger compared to the circular velocity which causes stellar orbits to be eccentric and off-planar.

2. Rotation curves in low-mass galaxies are usually rising and, thus, do not experience strong shear. As a consequence suppressed spiral activity is expected because shear is thought to be a major source of spiral perturbations (J. Sellwood, private communication, also Sellwood 2014).

3. Stellar feedback can remove a significant amount of gas on very short time scales from low-mass disks which modifies the galactic potential and, hence, the rotation curve (Navarro et al. 1996; Mo and Mao 2004; Read and Gilmore 2005; Mashchenko et al. 2006; Pontzen and Governato 2012; Macciò et al. 2012). The deeper potential wells of more massive galaxies limit the amount of ejected

gas and a strong effect on the rotation curve is not expected (Di Cintio et al. 2014).

### 4.5.3 Concluding Remarks

In this chapter, I present a very simple model that describes the equilibrium state of very efficient radial migration in galaxy disks. Its universal result is that the distribution function of orbital angular momenta is exponential. For a given rotation curve it is straightforward to use this angular momentum distribution to calculate the corresponding stellar surface density profile, given the assumption that orbits are circular. Surface density profiles, derived via this approach, fit observed and simulated disk profiles about as well as the observationally motivated but well-established exponential surface density profile (Freeman 1970).

The model is based on the simple ansatz that the time scales on which disk stars' angular momenta are shuffled completely is short compared to the age of the galaxy. This process is treated as a mechanism that creates entropy, which is maximized respecting idealized but physically motivated constraints. The derivation is completely analogous to deriving the Boltzmann distribution of ideal gases.

The methods of this model are very different from previous analytical attempts to explain the radial profiles of stellar disks in galaxies. These either assume that they are a consequence of the initial conditions (e. g. Fall and Efstathiou 1980; Dalcanton et al. 1997; Dutton 2009), viscous evolution of the parent gas disk (e. g. Lin and Pringle 1987; Yoshii and Sommer-Larsen 1989), scattering by interstellar clouds (Elmegreen and Struck 2013, 2016; Struck and Elmegreen 2017), or a combination of the above (Ferguson and Clarke 2001). Observations of weak radial age and metallicity gradients in galaxy disks support the assumption of efficient radial migration. However, disks with even weak metallicity gradients cannot be in a state of full equilibrium. The mixing of angular momenta cannot be complete but its efficiency appears to be sufficient for the resulting surface density profiles predicted by this model to be a good fit to data from observations and simulations.

# 5 Discussion, Conclusions and Prospects

In this thesis, I set out to explain the origin of the observed radial structure of stellar disks in the context of the formation of isolated galaxies. I deliberately exclude the cosmological context of the $\Lambda$CDM cosmological model to see to which extent certain aspects of galaxy formation and morphology can be explained independent of an underlying cosmological model.

## 5.1 The Origin of Breaks in the Radial Stellar Surface Density Profiles of Disk Galaxies

### 5.1.1 Summary and Discussion of Results

The shape of the radial density profiles of observed spiral galaxies fall into three main classes: (i) unbroken exponentials or Type-I, (ii) truncated two-component exponentials or Type-II, and (iii) antitruncated two-component exponentials or Type-III. Here, I employ numerical hydrodynamic $N$body simulations and successfully reproduce all three classes of disk galaxies.

These simulations are self-consistent in the sense that they model the hydrodynamics of the galactic gas, radiative cooling of that gas, star formation according to the Kennicutt-Schmidt law, and energetic stellar feedback. Some of these processes, especially star formation and feedback, cannot be resolved with the currently available computational power. For these processes the simulations rely on models that describe the effects of these processes on scales, which can be resolved by simulations.

The initial conditions for these simulations resemble a live dark matter halo that hosts a rotating gas sphere in hydrostatic equilibrium. They are evolved in complete isolation, hence all aspects of the evolution of the simulated galaxies are secular (internal) to the galaxy. The only aspect that is cosmologically motivated is the initial angular momentum distribution of the halo gas. It is chosen to represent typical angular momentum distributions of DM halos in cosmological simulations.

Since the simulations model gas cooling, the gas sphere starts to cool and collapse to the center of the dark matter halo where it settles into a rotating disk. Gas particles that settled in a disk rotate on near-circular orbits because gas is pressurized and the orbits of gas particles in simulations cannot cross. The galactocentric distance of a gas particle's orbit is set by its angular momentum and the rotation curve of the combined halo-disk system[1]. In the simulations, low-angular momentum gas cools first and settles in the center of the disk. As the simulations evolve, gas with progressively larger angular momentum cools and settles at larger radii. Consequently the disk grows.

To first order the amount of gas that settles at a given radius is determined by the initial angular momentum distribution of the gas halo. The more low-angular momentum material is present, the more gas settles at small radii. As soon as the first gas settles in the center, it reaches temperatures and densities that are necessary for star formation and the stellar disk forms. This resembles the currently favored picture of inside-out galaxy formation (Somerville and Davé 2015).

In chapter 2, I show results of two suites of simulations. In the first suite, I scale the global angular momentum distribution, in the second suite, I vary the shape of the distribution. Both have an impact on the amount of low-angular momentum gas (figure 2.1). In both suites I find that galaxies that form in halos with a lot of low-angular momentum gas have Type-III disk profiles and galaxies, which form in halos with little low-angular momentum gas have Type-II disks. In between these two regimes, the simulated galaxies feature near-exponential Type-I disks.

This is the first study of secular evolution of galaxies in the literature, which reproduces all types of observed stellar surface density profiles in spiral galaxies. The apparent dependence of the profile type on the amount of low-angular momentum gas gives rise to a correlation between the inner exponential scale length and the break type: The inner scale lengths increase with break type in the following order: Type-III, Type-I, Type-II. Gutiérrez et al. (2011) find the same qualitative trend but cannot establish a significant difference between the inner slopes of Type-I and II profiles.

In the first suite of simulations, near-exponential Type-I disks occur only for a narrow range of initial halo spin parameters $\lambda$. This is in qualitative agreement with studies of the demographics of disk types. These find fractions of purely exponential disks to be as low as 10 % (Pohlen and Trujillo 2006). The highest frequency of Type-I disks is found in cluster environments (Roediger et al. 2012; Maltby et al. 2015). It is 25 % (Maltby et al. 2015). Recent work explained the enhanced abundance of Type-I profiles in cluster environments (Clarke et al. 2017). They show that tidal interactions

---

[1]Here, the disk includes both, the gaseous and the stellar disk.

with the cluster potential triggers transient spiral activity, which, in turn, excite radial migration. Through this process they show that an initial Type-II profile is transformed to a Type-I profile and, therefore, provide a natural explanation for the lack of Type-II disks in clusters compared to field galaxies. This lack is compensated by a larger abundance of Type-I disks (Erwin et al. 2012).

My simulated galaxies, however, are completely isolated and their low frequency of emerging Type-I disks seems to agree well with the data for field galaxies, at least qualitatively. Quantitatively, there is a slight discrepancy between the relative abundance of Type-II and Type-III disks. Observational results suggest that Type-II disks are clearly more frequent than Type-II disks (e. g., Pohlen and Trujillo 2006, also see section 1.6.2). The spin parameter $\lambda \approx 0.035$ at which Type-I disks form in my simulations is slightly larger than the median value $\lambda = 0.031$ found in pure DM cosmological simulations (Macciò et al. 2008). Assuming that the gas and dark matter halo share the same angular momentum, the simulations suggest that Type-III disks are more frequent than Type-II disks.

For the second suite of simulations, such a sharp transition between the regime of Type-II and Type-III disks cannot be identified. The main reason is that I carried out fewer simulations in that suite and did not sample the shape parameter $\mu$ as dense as I sampled the spin parameter $\lambda$ in the first suite. The shape parameter, at which the transition occurs, is roughly $\mu = 1.3$ (the value of the simulation that forms a Type-I profile). This value is similar to the median value of shape parameters in cosmological simulations (Bullock et al. 2001), which points to roughly equal abundances of Type-II and Type-III disks.

Stewart et al. (2013) show that accreted gas tends to have higher angular momentum than the DM halo onto which it accretes. Their study is based on a sample of Milky Way-sized halos, which is the same mass regime as for my simulations. This potentially weakens the tension with observed abundances of Type-II/III disks.

On the other hand, this discrepancy might just be an indication that the situation in my simulations is overly simplified. The simulations do not consider any effects external to the galaxy. In particular the formation of Type-III profiles has previously been attributed to external factors such as interactions with companion galaxies (e. g., van der Kruit and Freeman 2011; Laine et al. 2014; Sellwood 2014) or gas accretion (Minchev et al. 2012).

The results of my simulations do show that each of the observed disk profile types can be reproduced via secular evolution of galaxies. However, the initial conditions, i. e. the angular momentum distribution of the host halo, may be determined by the cosmological background such as the local environment (cluster or field galaxy) or the merging history. Halo gas acquires its angular momentum via tidal torques in the early linear regime of structure formation (Peebles 1969; Doroshkevich 1970; White

1984; Schäfer 2009) and, later on, through merging with other halos (e. g. Dubois et al. 2014). These are processes that are affected by the underlying cosmological model.

### 5.1.2 Future Prospects

To better understand the formation of the different disk profiles, it would be interesting to check whether a similar correlation between the amount of low-angular momentum gas in a galaxy and the profile type can be found in cosmological simulations of disk galaxy formation. There exists a wide variety of suitable simulations such as the *FIRE* (Hopkins et al. 2014), the *Illustris* (Vogelsberger et al. 2014a,b; Genel et al. 2014; Sijacki et al. 2015), or the *NIHAO* (Wang et al. 2015) projects. Of course, for such a comparison one would have to identify a suitable measure for the amount of low-angular momentum gas.

Another possibility to test the predicted correlation would be to link the initial angular momentum distribution to an observable quantity, which is expected to correlate with the break type of the stellar profile as well. A suitable candidate is the effective spin parameter of a stellar disk (equation (2) in Emsellem et al. 2011). It is straightforward to derive this quantity from simulated disks and it can be observed with the technique of integral field spectroscopy[2] for galaxies that are moderately inclined with respect to the line of sight.

## 5.2 The Dynamical Link Between Bars and Antitruncated Type-III Disk Profiles

### 5.2.1 Summary and Discussion of Results

I performed a detailed analysis of the stellar dynamics in the simulations to gain further insight into the mechanism that leads to the formation of the Type-II and III profiles. In previous studies, galaxies with Type-II disk breaks could already be explained through secular evolution (e. g., Debattista et al. 2006; Roškar et al. 2008a; Foyle et al. 2008; Minchev et al. 2012). Therefore, the simulations that formed galaxies with a Type-III disk profile are the main subject of this project. I focused the analysis on stars that make up the disk outside the respective break radii in the final simulation outputs, which I call *outer disk stars*.

In both, simulated Type-II and III disks, I find that all outer disk stars initially formed on near-circular orbits and inside the respective break radius. Hence, all

---

[2]Integral field spectroscopy is a technique that allows to obtain spectra that are spatially resolved in two dimensions.

these stars must have migrated outwards. In the simulated Type-II disks, these stars are still on predominantly near-circular orbits in the final simulation output. This is consistent with the mechanism found by Roškar et al. (2008a). For this reason I did not investigate these simulations any further but instead focused the analysis on the simulation with the lowest halo spin ($\lambda = 0.02$), which formed a galaxy with a Type-III profile.

In this simulation the stars that "migrated" beyond the disk break are on very eccentric orbits. This is inconsistent with the "classic" churning mechanism (Sellwood and Binney 2002) that Roškar et al. (2008a) found to be responsible for populating the outskirts of Type-II disks. Instead I find a prominent signature of a strong central bar in the evolution of the stars' orbital energy and angular momentum, but only for those stars that make up the antitruncated part of the Type-III disk. The stars' orbits do, however, stay bound to the bar region because their pericentric distances do not significantly evolve. This is a strong hint that the bar drives the outward migration of the stars.

Such a strong bar only forms in the simulations with lots of low-angular momentum gas in their initial conditions. These form because of the resulting large surface densities in the center of the simulated galaxies, which are more susceptible to instabilities (Toomre 1964) and consequently to bar formation. The simulations with little low-angular momentum material form much weaker bars or none at all.

In a simplified toy model, I mimic a bar-like potential and evolve the orbits of stars that are initially on circular orbits and have an exponential surface density profile. The stars in this model are treated as test particles, their own gravitational attraction is ignored. With this simple numerical experiment, I show that a strong central bar can turn initially circular orbits into very eccentric orbits with large semi-major axes. At large radii this model develops an excess of stars. This demonstrates the potential of a strong bar to cause a mass excess of stars on eccentric orbits at large galactocentric radii. Such a mass excess may possibly comprise the antitruncated part of a Type-III disk.

I interpret the results to be a consequence of the formation of the massive bar. Before the formation of the bar the stars are in a dynamical equilibrium configuration of the unperturbed galaxy potential. When the bar forms, the star particles get "caught" by the resonances (corotation or Lindblad resonances) but for the moment they keep their orbits. Now, these orbits are not in dynamical equilibrium any more because the potential has changed and is now time-dependent, since the bar rotates. The stellar orbits evolve to a new equilibrium configuration, which involves a significant fraction of orbits with large radial excursions.

These dynamics of the stars in the disk outskirts give rise to peculiar global dynamical signatures. Compared to the circular velocity curve, which is determined by

the galactic potential, the actual mean rotational velocity in the outskirts of Type-III disks is about a factor of four slower. The dispersion of the radial velocity component is exceptionally large and significantly exceeds that of the azimuthal and vertical components.

Since the disk outskirts (including the regions where the break in the profiles occurs) are very faint, they are difficult to observe. A possibility to overcome this difficulty is to observe the velocity dispersion of planetary nebulae in the disk outskirts. These are very bright objects, which can be observed even in the very faint parts of stellar disks and they are expected to have the same dynamical properties as the stellar population they belong to. Planetary nebulae have been used before to determine velocity dispersions (Douglas et al. 2000; Herrmann and Ciardullo 2009).

### 5.2.2  Future Prospects

Whether or not the processes, which I find to be responsible for bar formation are efficient in real galaxies, remains an open question. I do, however, provide predictions that can be observed: The disk outskirts of Type-III disks galaxies with a strong bar are slowly rotating and have an exceptionally large radial velocity dispersion. If observations succeed to detect such a galaxy that would be an indication that this model is indeed right. However, it is not a proof, since a similar prediction has been made for Type-III disks in simulations that form through external gas accretion (Minchev et al. 2012). There are researchers that believe that Type-III disks are generally dispersion supported (I. Minchev, private communication). However, if observations fail to detect these dispersion supported disks, the physical processes I identified in the simulations are unlikely to be applicable to real galaxies. Consequently this observational prediction provides a possibility to falsify this model.

Further investigation of the detailed dynamical signatures of bar-driven Type-III disks are necessary to break the degeneracy between the different proposed formation mechanisms of Type-III disks.

The actual surface brightness at the break in the profile might depend on the Type of the profile (V. Debattista, private communication). I did not investigate this. If such a dependence exists, it provides an additional way to test this model observationally. Depending on the strength of such a correlation, making a solid prediction here would involve complicated modeling with radiative transfer models to account for processes like galactic extinction or dust reddening. Alternatively, observers would have to provide data, that allows to deduce a reliable estimate of the actual mass surface densities at the break from the observed surface brightness.

The center of the simulated galaxies that form Type-III disk profiles might be affected by the overcooling problem due to their large gas surface densities (see

section 1.4.4). As a consequence, too many stars form, which leads to instabilities and bar formation. Whether or not this is the case was not investigated in this thesis. A common approach to address this problem in massive galaxies is to implement feedback from active galactic nuclei (AGN). Such feedback is not included in the simulation code CHANGA, which I used to evolve the simulations for this project. It would be interesting to see if the same initial conditions give rise to similar trends and physics if they were evolved with a simulation code that does model AGN feedback.

## 5.3 Radial Surface-Density Profiles in Maximum Entropy Disks

### 5.3.1 Summary and Discussion of Results

Prior to this thesis, it had not been well understood, certainly not analytically, why many disks have near-exponential surface density profiles and why the individual parts of broken disks (section 1.6.2) are also exponential. In the meantime, Berrier and Sellwood (2015) showed that radial migration smoothes galaxy rotation curves and the corresponding surface density profiles. They conclude that this may promote the formation of near-exponential profiles.

In this thesis, I investigated a very different approach. It also rests on the existence of very efficient radial migration in galactic disks and assumes that it increases a suitably defined entropy. Other central assumptions are that stellar orbits are near-circular and coplanar, the absence of radial and vertical heating, and that the total mass and angular momentum of the stellar disk are conserved. These assumptions are likely to be well approximated by radial migration (Sellwood and Binney 2002; Roškar et al. 2012).

I show that in a maximum entropy state, the distribution function $F$ of orbital angular momenta $j$ has an exponential form: $F(j) \propto \exp(-j/\langle j \rangle)$ where $\langle j \rangle$ is the mean specific angular momentum of the stellar disk. Starting from this intermediate result, I derive an analytic expression for the radial ($R$) stellar surface density profile, given a galactic rotation (circular velocity) curve $v_c(R)$:

$$\Sigma_\star(R) = \frac{M}{2\pi R R_e(R)} \exp\left[-\frac{R}{R_e(R)}\right] \left(1 + \frac{\mathrm{d}\log v_c}{\mathrm{d}\log R}\right), \qquad (5.1)$$

with $R_e(R) \equiv \langle j \rangle / v_c(R)$ and $M$ the total mass of the disk.

This expression for stellar surface density profiles is a smooth function of galactocentric radius $R$ and of the circular velocity curve. It provides a natural explanation for

the results from many simulations that surface density profiles tend to be smoothed on rather short time scales (e. g., Berrier and Sellwood 2015). Since, rotation curves in rather massive disk galaxies tend to be flat at large radii (larger than a few scale lengths) the predicted profile in these regions reduces to be $\Sigma_\star \propto R^{-1} \exp\left(-R/R_d\right)$, which is practically indistinguishable from a purely exponential profile at such radii.

Due to the smooth dependence on $v_c(R)$ and $R$, it is not straightforward to reproduce features in the surface density profiles such as Type-II or III breaks within this framework. Such a feature can only be produced by a corresponding feature in the galactic rotation curve. This is exactly what *Renzo's rule* states (Sancisi 2004). However, the derived expression for the surface density does depend on the derivative of the rotation curve and, consequently, any abrupt change in the rotation curve's slope would result in a discontinuous surface density profile. A break-like feature in the profile can be reproduced if the second radial derivative of the rotation curve is discontinuous. This implies that rather subtle features in the rotation may cause clearly visible features in the surface density profile.

## 5.3.2  Comparison to other Work

Other recent studies argue that scattering off of clumps in a disk may produce near-exponential surface density profiles (Elmegreen and Struck 2013, 2016; Struck and Elmegreen 2017). Unlike radial migration, these scattering processes dynamically heat the stellar disk. The latter two of these studies also provide analytic expressions for the resulting surface density profiles. Elmegreen and Struck (2016) assume that the scattering direction off of the clumps is biased towards the galactic center and derive that $\Sigma_\star \propto \exp(-R/R_d)/R$. This is equivalent to my result for a flat rotation curve. Struck and Elmegreen (2017) derive a Sersic-type profile as a result of hydrostatic equilibrium: $\Sigma_\star \propto R^{p-1} \exp\left(-(R/R_d)^p\right)$. They argue that $p \approx 1$, which yields a near-exponential profile. However, Struck and Elmegreen (2017) assume the orbits to be only mildly eccentric, which might be violated by the scattering mechanism that their model is based on. Neither of these studies compare their results to actual data. Struck and Elmegreen (2017) merely state that certain subsets of the available parameter space allow to reproduce Type-II disk profiles.

The argument of the exponential factor in the surface density formula of the maximum-entropy disk scales with the galaxy's mean angular momentum $\langle j \rangle$. This leads to more extended disks for galaxies with larger angular momenta, which qualitatively agrees with a variety of earlier models of disk galaxy formation (e. g., Dalcanton et al. 1997; Mo et al. 1998). The normalization scales with $\langle j \rangle^{-1}$ causing lower central densities for extended high-angular momentum disks, which also agrees qualitatively with the results from Dalcanton et al. (1997).

### 5.3.3 Comparison with Observations and Simulations

It turned out to be rather difficult to compare the derived formula to observations. I used a somewhat dated dataset provided by Courteau (1996, 1997), because it provides *r*-band surface photometry and a functional form as well as best fit-parameters for the rotation curves of 304 disk galaxies. These data has two advantages that are very useful for the comparison. First, the rotation curves can be expressed analytically and, second, it is reasonable to assume that the mass-to-light is constant with galactocentric distance in the *r*-band (van der Kruit and Freeman 2011), which allows for a straightforward comparison to predicted surface density profiles. I find that for a substantial fraction of the observed galaxies, the maximum-entropy surface brightness profiles derived from the rotation curve data agrees quite well with the photometric data. However, for a non-negligible fraction of the galaxies the model does not reproduce the data. Most of the galaxies give at least fair agreement. For most galaxies, the most prominent discrepancies occur at large radii where they may have disk breaks. Due to the functional form of the rotation curve model, which is flat at these radii, such breaks cannot be captured by the maximum-entropy model. Additionally, some observed surface brightness profiles have local features that may reflect other interactions of the galaxies with satellites or close companions, which cannot be reproduced in this framework of maximum-entropy disks.

I also find that the maximum-entropy model describes the data equally well as the empirically motivated exponential disk profile (Freeman 1970). This is a very promising result, because I found a theoretically motivated model that describes observed data equally well as the empirically motivated profile.

In simulations, the circular velocity curve can be computed directly, because the galactic potential is known. With this information, the maximum-entropy model allows to predict the surface density profile, which can then be compared to the data from the simulation. I use the suite of simulations from this work with varying spin parameters to perform such a comparison and find that the central regions agree very well in all considered cases. However, the simulation with low initial spin shows only poor agreement in the outskirts. The agreement gets progressively better with increasing halo spin. This possibly reflects the assumption of the model that stars have to be on circular orbits, which is met best in the high spin simulations (see above).

Given the very idealized and simplifying assumption, which this maximum-entropy model is based on, its agreement with data from observations and simulations is surprisingly good. It provides a natural explanation for the widely observed near-exponential surface density profiles (Freeman 1970) based on the secular process of radial migration. The scale length of the disks, however, depends on the total

galactic angular momentum, which, in turn, depends on the formation history of the respective galaxy's host halo and, hence, on the cosmological model.

### 5.3.4  Future Prospects

Despite the good agreement with observed and simulated data, it is worthwhile to explore the effects of relaxing some of these very restrictive assumptions. The most obvious extension of the model would be to allow for radial and/or vertical motion. While this introduces additional degrees of freedom in the model, it might allow to reproduce even the surface density profiles of the simulated disks that form in low-spin halos. While such an extension to the model is in principle straightforward, the computations will be much more complicated, because a bijective mapping between angular momentum and galactocentric distance is not possible for non-circular orbits.

Another aspect that would deserve further investigation is whether or not the model is applicable to S0 or dwarf galaxies. The former have no spiral activity by definition and the latter are expected to have suppressed spiral activity if any at all. Spiral activity is a prerequisite for radial migration and consequently also for the application of the maximum-entropy model. In the case of dwarf galaxies the applicability of the model might be impaired by additional factors, which are (i) a larger degree of random motion, which I found to limit the applicability of the model and (ii) the capability of stellar feedback to change the galactic potential, and hence the rotation curve on very short timescales, which does not allow for an equilibrium configuration.

## 5.4  Concluding Remarks

In this thesis, I show that several important aspects of the radial structure of stellar disks in galaxies can be explained purely via their secular evolution. Namely, these aspects are the occurrence and formation of broken radial surface density profiles and the ubiquitous near-exponential shape of radial light profiles.

Using numerical simulations, I was able to reproduce all three types of observed radial surface density profiles, purely exponential, truncated and antitruncated, Type-I, II, and III profiles. This is the first study to reproduce all three types within the same framework. The mechanism to form truncated profiles was found to be consistent with previous work. A new result is a potential mechanism of secular evolution of a galaxy that produces antitruncated Type-III profiles.

In the last project of this thesis, I derive an analytic formula for the surface density profile of stellar galaxy disks that is based on secular evolution. It provides a natural

explanation for the occurrence of the omnipresent near-exponential surface brightness profiles.

In both, the simulations and the maximum-entropy model, global properties of the disk such as their radial scale length or the central surface density depend on the cosmological framework. Their detailed structure is governed by the secular evolution of the respective galaxy.

The studies that I carried out for this thesis were designed to ignore any influences that are external to the studied galaxy. Nevertheless, these influences such as mergers or tidal forces are known to have profound consequences for the evolution of galaxies. The relative importance of secular processes over cosmological effects was not topic of this thesis. The mechanisms, which I find in this thesis *may* be responsible for the formation of the observed radial structure of stellar disks but, they do not exclude a possible contribution by other secular or external effects.

I identify a number of new problems that this work raised and which remain unsolved. These questions are sufficiently extensive to fill a thesis on their own.

# Acronyms

**ΛCDM**  Lambda cold dark matter cosmological model

**AGN**  Active galactic nucleus

**CDM**  Cold dark matter

**CMB**  Cosmic microwave background

**CR**  Corotation resonance

**DM**  Dark matter

**ILR**  Inner Lindblad resonance

**LSB**  Low-surface brightness galaxy

**MCMC**  Monte-Carlo Markov-chain

**NFW**  Navarro–Frenk–White halo density profile

**OLR**  Outer Lindblad resonance

**PDF**  Probability density function

**SF**  Star formation

**SFR**  Star formation rate

**SN**  Supernova

**SNe**  Supernovae

**SPH**  Smoothed-particle hydrodynamics

# Bibliography

B. P. Abbott, R. Abbott, T. D. Abbott, M. R. Abernathy, F. Acernese, K. Ackley, C. Adams, T. Adams, P. Addesso, R. X. Adhikari, and et al. Observation of Gravitational Waves from a Binary Black Hole Merger. *Physical Review Letters*, 116(6):061102, February 2016. doi: 10.1103/PhysRevLett.116.061102.

R. J. Allen and F. H. Shu. The extrapolated central surface brightness of galaxies. *ApJ*, 227:67–72, January 1979. doi: 10.1086/156705.

E. Athanassoula, M. Romero-Gómez, and J. J. Masdemont. Rings and spirals in barred galaxies - I. Building blocks. *MNRAS*, 394:67–81, March 2009. doi: 10.1111/j.1365-2966.2008.14273.x.

R. Azzollini, I. Trujillo, and J. E. Beckman. Color Profiles of Disk Galaxies since z~ 1: Probing Outer Disk Formation Scenarios. *ApJ*, 679:L69, June 2008. doi: 10.1086/589283.

J. Baba, K. Morokuma-Matsui, Y. Miyamoto, F. Egusa, and N. Kuno. Gas velocity patterns in simulated galaxies: observational diagnostics of spiral structure theories. *MNRAS*, 460:2472–2481, August 2016. doi: 10.1093/mnras/stw987.

J. Bakos, I. Trujillo, and M. Pohlen. Color Profiles of Spiral Galaxies: Clues on Outer-Disk Formation Scenarios. *ApJ*, 683:L103, August 2008. doi: 10.1086/591671.

I. K. Baldry, K. Glazebrook, and S. P. Driver. On the galaxy stellar mass function, the mass-metallicity relation and the implied baryonic mass function. *MNRAS*, 388:945–959, August 2008. doi: 10.1111/j.1365-2966.2008.13348.x.

A. Barteldrees and R.-J. Dettmar. Parameters of stellar disks from CCD surface photometry of edge-on galaxies. *A&AS*, 103, March 1994.

P. S. Behroozi, R. H. Wechsler, and C. Conroy. The Average Star Formation Histories of Galaxies in Dark Matter Halos from z = 0-8. *ApJ*, 770:57, June 2013. doi: 10.1088/0004-637X/770/1/57.

J. C. Berrier and J. A. Sellwood. Smoothing Rotation Curves and Mass Profiles. *ApJ*, 799:213, February 2015. doi: 10.1088/0004-637X/799/2/213.

G. Bertone, D. Hooper, and J. Silk. Particle dark matter: evidence, candidates and constraints. *Physics Reports*, 405:279–390, 2004.

F. Bigiel, A. Leroy, F. Walter, E. Brinks, W. J. G. de Blok, B. Madore, and M. D. Thornley. The Star Formation Law in Nearby Galaxies on Sub-Kpc Scales. *AJ*, 136:2846–2871, December 2008. doi: 10.1088/0004-6256/136/6/2846.

James Binney and Scott Tremaine. *Galactic dynamics.* Princeton series in astrophysics. Princeton University Press, Princeton, NJ ; Oxford, 2. ed. edition, 2008. ISBN 978-0-691-13027-9 ; 978-0-691-13026-2.

G. R. Blumenthal, S. M. Faber, R. Flores, and J. R. Primack. Contraction of dark matter galactic halos due to baryonic infall. *ApJ*, 301:27–34, February 1986. doi: 10.1086/163867.

A. Borlaff, M. C. Eliche-Moral, C. Rodríguez-Pérez, M. Querejeta, T. Tapia, P. G. Pérez-González, J. Zamorano, J. Gallego, and J. Beckman. Formation of S0 galaxies through mergers. Antitruncated stellar discs resulting from major mergers . *A&A*, 570:A103, October 2014. doi: 10.1051/0004-6361/201424299.

A. Bosma and K. C. Freeman. On the central surface brightness problem in disk galaxies. *AJ*, 106: 1394–1404, October 1993. doi: 10.1086/116734.

F. Bournaud, D. Chapon, R. Teyssier, L. C. Powell, B. G. Elmegreen, D. M. Elmegreen, P.-A. Duc, T. Contini, B. Epinat, and K. L. Shapiro. Hydrodynamics of High-redshift Galaxy Collisions: From Gas-rich Disks to Dispersion-dominated Mergers and Compact Spheroids. *ApJ*, 730:4, March 2011. doi: 10.1088/0004-637X/730/1/4.

M. Boylan-Kolchin, J. S. Bullock, and M. Kaplinghat. Too big to fail? The puzzling darkness of massive Milky Way subhaloes. *MNRAS*, 415:L40–L44, July 2011. doi: 10.1111/j.1745-3933.2011.01074.x.

M. Boylan-Kolchin, J. S. Bullock, and M. Kaplinghat. The Milky Way's bright satellites as an apparent failure of ΛCDM. *MNRAS*, 422:1203–1218, May 2012. doi: 10.1111/j.1365-2966.2012.20695.x.

C. B. Brook, G. Stinson, B. K. Gibson, R. Roškar, J. Wadsley, and T. Quinn. Hierarchical formation of bulgeless galaxies - II. Redistribution of angular momentum via galactic fountains. *MNRAS*, 419: 771–779, January 2012. doi: 10.1111/j.1365-2966.2011.19740.x.

J. S. Bullock, A. V. Kravtsov, and D. H. Weinberg. Reionization and the Abundance of Galactic Satellites. *ApJ*, 539:517–521, August 2000. doi: 10.1086/309279.

J. S. Bullock, A. Dekel, T. S. Kolatt, A. V. Kravtsov, A. A. Klypin, C. Porciani, and J. R. Primack. A Universal Angular Momentum Profile for Galactic Halos. *ApJ*, 555:240–257, July 2001. doi: 10.1086/321477.

R. G. Carlberg. The vertical structure of galactic disks. *ApJ*, 322:59–63, November 1987. doi: 10.1086/165702.

A. J. Clarke, V. P. Debattista, R. Roškar, and T. Quinn. The origin of type I profiles in cluster lenticulars: an interplay between ram pressure stripping and tidally induced spiral migration. *MNRAS*, 465: L79–L83, February 2017. doi: 10.1093/mnrasl/slw214.

M. Colless, G. Dalton, S. Maddox, W. Sutherland, P. Norberg, S. Cole, J. Bland-Hawthorn, T. Bridges, R. Cannon, C. Collins, W. Couch, N. Cross, K. Deeley, R. De Propris, S. P. Driver, G. Efstathiou, R. S. Ellis, C. S. Frenk, K. Glazebrook, C. Jackson, O. Lahav, I. Lewis, S. Lumsden, D. Madgwick, J. A. Peacock, B. A. Peterson, I. Price, M. Seaborne, and K. Taylor. The 2dF Galaxy Redshift Survey: spectra and redshifts. *MNRAS*, 328:1039–1063, December 2001. doi: 10.1046/j.1365-8711.2001.04902.x.

S. Courteau. Deep r-Band Photometry for Northern Spiral Galaxies. *ApJS*, 103:363, April 1996. doi: 10.1086/192281.

S. Courteau. Optical Rotation Curves and Linewidths for Tully-Fisher Applications. *AJ*, 114:2402, December 1997. doi: 10.1086/118656.

Richard H. Cyburt, Brian D. Fields, Keith A. Olive, and Tsung-Han Yeh. Big bang nucleosynthesis: Present status. *Rev. Mod. Phys.*, 88:015004, Feb 2016. doi: 10.1103/RevModPhys.88.015004. URL http://link.aps.org/doi/10.1103/RevModPhys.88.015004.

J. J. Dalcanton, D. N. Spergel, and F. J. Summers. The Formation of Disk Galaxies. *ApJ*, 482:659–676, June 1997.

C. Dalla Vecchia and J. Schaye. Simulating galactic outflows with thermal supernova feedback. *MNRAS*, 426:140–158, October 2012. doi: 10.1111/j.1365-2966.2012.21704.x.

W. J. G. de Blok, S. S. McGaugh, A. Bosma, and V. C. Rubin. Mass Density Profiles of Low Surface Brightness Galaxies. *ApJ*, 552:L23–L26, May 2001a. doi: 10.1086/320262.

W. J. G. de Blok, S. S. McGaugh, and V. C. Rubin. High-Resolution Rotation Curves of Low Surface Brightness Galaxies. II. Mass Models. *AJ*, 122:2396–2427, November 2001b. doi: 10.1086/323450.

R. de Grijs, M. Kregel, and K. H. Wesson. Radially truncated galactic discs. *MNRAS*, 324:1074–1086, July 2001. doi: 10.1046/j.1365-8711.2001.04380.x.

R. S. de Jong. Near-infrared and optical broadband surface photometry of 86 face-on disk dominated galaxies. IV. Using color profiles to study stellar and dust content of galaxies. *A&A*, 313:377–395, September 1996.

G. de Vaucouleurs. Classification and Morphology of External Galaxies. *Handbuch der Physik*, 53:275, 1959.

V. P. Debattista, L. Mayer, C. M. Carollo, B. Moore, J. Wadsley, and T. Quinn. The Secular Evolution of Disk Structural Parameters. *ApJ*, 645:209–227, July 2006. doi: 10.1086/504147.

A. Dekel, Y. Birnboim, G. Engel, J. Freundlich, T. Goerdt, M. Mumcuoglu, E. Neistein, C. Pichon, R. Teyssier, and E. Zinger. Cold streams in early massive hot haloes as the main mode of galaxy formation. *Nature*, 457:451–454, January 2009. doi: 10.1038/nature07648.

A. Di Cintio, C. B. Brook, A. V. Macciò, G. S. Stinson, A. Knebe, A. A. Dutton, and J. Wadsley. The dependence of dark matter profiles on the stellar to halo mass ratio: a prediction for cusps vs cores. *arXiv:1306.0898*, June 2013.

A. Di Cintio, C. B. Brook, A. V. Macciò, G. S. Stinson, A. Knebe, A. A. Dutton, and J. Wadsley. The dependence of dark matter profiles on the stellar-to-halo mass ratio: a prediction for cusps versus cores. *MNRAS*, 437:415–423, January 2014. doi: 10.1093/mnras/stt1891.

P. Di Matteo, M. Haywood, F. Combes, B. Semelin, and O. N. Snaith. Signatures of radial migration in barred galaxies: Azimuthal variations in the metallicity distribution of old stars. *A&A*, 553:A102, May 2013. doi: 10.1051/0004-6361/201220539.

S. Dodelson. *Modern cosmology*. 2003.

E. D'Onghia, M. Vogelsberger, and L. Hernquist. Self-perpetuating Spiral Arms in Disk Galaxies. *ApJ*, 766:34, March 2013. doi: 10.1088/0004-637X/766/1/34.

A. G. Doroshkevich. Spatial structure of perturbations and origin of galactic rotation in fluctuation theory. *Astrophysics*, 6:320–330, October 1970. doi: 10.1007/BF01001625.

N. G. Douglas, J. Gerssen, K. Kuijken, and M. R. Merrifield. Using slitless spectroscopy to study the kinematics of the planetary nebula population in M94. *MNRAS*, 316:795–802, August 2000. doi: 10.1046/j.1365-8711.2000.03574.x.

J. L. E. Dreyer. A New General Catalogue of Nebulæ and Clusters of Stars, being the Catalogue of the late Sir John F. W. Herschel, Bart, revised, corrected, and enlarged. *MmRAS*, 49:1, 1888.

J. L. E. Dreyer. Index Catalogue of Nebulæ found in the years 1888 to 1894, with Notes and Corrections to the New General Catalogue. *MmRAS*, 51:185, 1895.

J. L. E. Dreyer. Second Index Catalogue of Nebulæ and Clusters of Stars, containing objects found in the years 1895 to 1907; with Notes and Corrections to the New General Catalouge and to the Index Catalogue for 1888-94. *MmRAS*, 59:105, 1910.

Y. Dubois, C. Pichon, C. Welker, D. Le Borgne, J. Devriendt, C. Laigle, S. Codis, D. Pogosyan, S. Arnouts, K. Benabed, E. Bertin, J. Blaizot, F. Bouchet, J.-F. Cardoso, S. Colombi, V. de Lapparent, V. Desjacques, R. Gavazzi, S. Kassin, T. Kimm, H. McCracken, B. Milliard, S. Peirani, S. Prunet, S. Rouberol, J. Silk, A. Slyz, T. Sousbie, R. Teyssier, L. Tresse, M. Treyer, D. Vibert, and M. Volonteri. Dancing in the dark: galactic properties trace spin swings along the cosmic web. *MNRAS*, 444:1453–1468, October 2014. doi: 10.1093/mnras/stu1227.

A. A. Dutton. On the origin of exponential galaxy discs. *MNRAS*, 396:121–140, June 2009. doi: 10.1111/j.1365-2966.2009.14741.x.

A. A. Dutton, A. V. Macciò, J. Frings, L. Wang, G. S. Stinson, C. Penzo, and X. Kang. NIHAO V: too big does not fail - reconciling the conflict between ΛCDM predictions and the circular velocities of nearby field galaxies. *MNRAS*, 457:L74–L78, March 2016. doi: 10.1093/mnrasl/slv193.

O. J. Eggen, D. Lynden-Bell, and A. R. Sandage. Evidence from the motions of old stars that the Galaxy collapsed. *ApJ*, 136:748, November 1962. doi: 10.1086/147433.

B. G. Elmegreen and C. Struck. Exponential Galaxy Disks from Stellar Scattering. *ApJ*, 775:L35, October 2013. doi: 10.1088/2041-8205/775/2/L35.

B. G. Elmegreen and C. Struck. Exponential Disks from Stellar Scattering. III. Stochastic Models. *ApJ*, 830:115, October 2016. doi: 10.3847/0004-637X/830/2/115.

B. G. Elmegreen, F. Bournaud, and D. M. Elmegreen. Bulge Formation by the Coalescence of Giant Clumps in Primordial Disk Galaxies. *ApJ*, 688:67-77, November 2008. doi: 10.1086/592190.

E. Emsellem, M. Cappellari, D. Krajnović, K. Alatalo, L. Blitz, M. Bois, F. Bournaud, M. Bureau, R. L. Davies, T. A. Davis, P. T. de Zeeuw, S. Khochfar, H. Kuntschner, P.-Y. Lablanche, R. M. McDermid, R. Morganti, T. Naab, T. Oosterloo, M. Sarzi, N. Scott, P. Serra, G. van de Ven, A.-M. Weijmans, and L. M. Young. The ATLAS$^{3D}$ project - III. A census of the stellar angular momentum within the effective radius of early-type galaxies: unveiling the distribution of fast and slow rotators. *MNRAS*, 414:888–912, June 2011. doi: 10.1111/j.1365-2966.2011.18496.x.

P. Erwin, J. E. Beckman, and M. Pohlen. Antitruncation of Disks in Early-Type Barred Galaxies. *ApJ*, 626:L81–L84, June 2005. doi: 10.1086/431739.

P. Erwin, M. Pohlen, and J. E. Beckman. The Outer Disks of Early-Type Galaxies. I. Surface-Brightness Profiles of Barred Galaxies. *AJ*, 135:20–54, January 2008. doi: 10.1088/0004-6256/135/1/20.

P. Erwin, L. Gutiérrez, and J. E. Beckman. A Strong Dichotomy in S0 Disk Profiles between the Virgo Cluster and the Field. *ApJ*, 744:L11, January 2012. doi: 10.1088/2041-8205/744/1/L11.

S. M. Faber and J. S. Gallagher. Masses and mass-to-light ratios of galaxies. *ARAA*, 17:135–187, 1979. doi: 10.1146/annurev.aa.17.090179.001031.

S. M. Faber and R. E. Jackson. Velocity dispersions and mass-to-light ratios for elliptical galaxies. *ApJ*, 204:668–683, March 1976. doi: 10.1086/154215.

S. M. Fall and G. Efstathiou. Formation and rotation of disc galaxies with haloes. *MNRAS*, 193:189–206, October 1980.

A. Fattahi, J. F. Navarro, T. Sawala, C. S. Frenk, L. V. Sales, K. Oman, M. Schaller, and J. Wang. The cold dark matter content of Galactic dwarf spheroidals: no cores, no failures, no problem. *ArXiv e-prints*, July 2016.

A.M.N. Ferguson and C. J. Clarke. The evolution of stellar exponential discs. *MNRAS*, 325:781–791, August 2001. doi: 10.1046/j.1365-8711.2001.04501.x.

D. Foreman-Mackey, D. W. Hogg, D. Lang, and J. Goodman. emcee: The MCMC Hammer. *PASP*, 125:306–312, March 2013. doi: 10.1086/670067.

J. B. Fouvry, C. Pichon, J. Magorrian, and P. H. Chavanis. Secular diffusion in discrete self-gravitating tepid discs II. Accounting for swing amplification via the matrix method. *A&A*, 584:A129, December 2015. doi: 10.1051/0004-6361/201527052.

K. Foyle, S. Courteau, and R. J. Thacker. An N-body/SPH study of isolated galaxy mass density profiles. *MNRAS*, 386:1821–1844, June 2008. doi: 10.1111/j.1365-2966.2008.13201.x.

K. C. Freeman. On the Disks of Spiral and so Galaxies. *ApJ*, 160:811, June 1970. doi: 10.1086/150474.

C. S. Frenk and S. D. M. White. Dark matter and cosmic structure. *Annalen der Physik*, 524:507–534, October 2012. doi: 10.1002/andp.201200212.

D. Friedli, W. Benz, and R. Kennicutt. On the influence of bars and star formation on galactic abundance gradients. *ApJ*, 430:L105–L108, August 1994. doi: 10.1086/187449.

A. Friedmann. Über die Krümmung des Raumes. *Zeitschrift fur Physik*, 10:377–386, 1922. doi: 10.1007/BF01332580.

B. Fuchs. Density waves in the shearing sheet. IV. Interaction with a live dark halo. *A&A*, 419:941–948, June 2004. doi: 10.1051/0004-6361:20040098.

A. Gallazzi, S. Charlot, J. Brinchmann, S. D. M. White, and C. A. Tremonti. The ages and metallicities of galaxies in the local universe. *MNRAS*, 362:41–58, September 2005. doi: 10.1111/j.1365-2966.2005.09321.x.

S. Garrison-Kimmel, M. Rocha, M. Boylan-Kolchin, J. S. Bullock, and J. Lally. Can feedback solve the too-big-to-fail problem? *MNRAS*, June 2013. doi: 10.1093/mnras/stt984.

M. J. Geller and J. P. Huchra. Mapping the universe. *Science*, 246:897–903, November 1989. doi: 10.1126/science.246.4932.897.

S. Genel, M. Vogelsberger, V. Springel, D. Sijacki, D. Nelson, G. Snyder, V. Rodriguez-Gomez, P. Torrey, and L. Hernquist. Introducing the Illustris project: the evolution of galaxy populations across cosmic time. *MNRAS*, 445:175–200, November 2014. doi: 10.1093/mnras/stu1654.

K. Genovali, B. Lemasle, G. Bono, M. Romaniello, M. Fabrizio, I. Ferraro, G. Iannicola, C. D. Laney, M. Nonino, M. Bergemann, R. Buonanno, P. François, L. Inno, R.-P. Kudritzki, N. Matsunaga, S. Pedicelli, F. Primas, and F. Thévenin. On the fine structure of the Cepheid metallicity gradient in the Galactic thin disk. *A&A*, 566:A37, June 2014. doi: 10.1051/0004-6361/201323198.

G. Gentile, B. Famaey, H. Zhao, and P. Salucci. Universality of galactic surface densities within one dark halo scale-length. *Nature*, 461:627–628, October 2009. doi: 10.1038/nature08437.

J. Gerssen, K. Kuijken, and M. R. Merrifield. The shape of the velocity ellipsoid in NGC 488. *MNRAS*, 288:618–622, July 1997. doi: 10.1093/mnras/288.3.618.

J. Gerssen, K. Kuijken, and M. R. Merrifield. Disc heating in NGC 2985. *MNRAS*, 317:545–549, September 2000. doi: 10.1046/j.1365-8711.2000.03667.x.

L. Girardi, B. F. Williams, K. M. Gilbert, P. Rosenfield, J. J. Dalcanton, P. Marigo, M. L. Boyer, A. Dolphin, D. R. Weisz, J. Melbourne, K. A. G. Olsen, A. C. Seth, and E. Skillman. The ACS Nearby Galaxy Survey Treasury. IX. Constraining Asymptotic Giant Branch Evolution with Old Metal-poor Galaxies. *ApJ*, 724:1030–1043, December 2010. doi: 10.1088/0004-637X/724/2/1030.

O. Y. Gnedin, A. V. Kravtsov, A. A. Klypin, and D. Nagai. Response of Dark Matter Halos to Condensation of Baryons: Cosmological Simulations and Improved Adiabatic Contraction Model. *ApJ*, 616:16–26, November 2004. doi: 10.1086/424914.

D. Goddard, D. Thomas, C. Maraston, K. Westfall, J. Etherington, R. Riffel, N. D. Mallmann, Z. Zheng, M. Argudo-Fernández, M. Bershady, K. Bundy, N. Drory, D. Law, R. Yan, D. Wake, A. Weijmans, D. Bizyaev, J. Brownstein, R. R. Lane, R. Maiolino, K. Masters, M. Merrifield, C. Nitschelm, K. Pan, A. Roman-Lopes, and T. Storchi-Bergmann. Sdss-iv manga: Stellar population gradients as a function of galaxy environment. *MNRAS*, 2016. doi: 10.1093/mnras/stw2719. URL http://mnras.oxfordjournals.org/content/early/2016/10/23/mnras.stw2719.abstract.

P. Goldreich and D. Lynden-Bell. II. Spiral arms as sheared gravitational instabilities. *MNRAS*, 130:125, 1965. doi: 10.1093/mnras/130.2.125.

F. Governato, L. Mayer, J. Wadsley, J. P. Gardner, B. Willman, E. Hayashi, T. Quinn, J. Stadel, and G. Lake. The Formation of a Realistic Disk Galaxy in Λ-dominated Cosmologies. *ApJ*, 607:688–696, June 2004. doi: 10.1086/383516.

F. Governato, B. Willman, L. Mayer, A. Brooks, G. Stinson, O. Valenzuela, J. Wadsley, and T. Quinn. Forming disc galaxies in ΛCDM simulations. *MNRAS*, 374:1479–1494, February 2007. doi: 10.1111/j.1365-2966.2006.11266.x.

F. Governato, C. Brook, L. Mayer, A. Brooks, G. Rhee, J. Wadsley, P. Jonsson, B. Willman, G. Stinson, T. Quinn, and P. Madau. Bulgeless dwarf galaxies and dark matter cores from supernova-driven outflows. *Nature*, 463:203–206, January 2010. doi: 10.1038/nature08640.

R. J. J. Grand, D. Kawata, and M. Cropper. The dynamics of stars around spiral arms. *MNRAS*, 421: 1529–1538, April 2012. doi: 10.1111/j.1365-2966.2012.20411.x.

R.J.J. Grand, D. Kawata, and M. Cropper. Impact of radial migration on stellar and gas radial metallicity distribution. *MNRAS*, 447:4018–4027, March 2015. doi: 10.1093/mnras/stv016.

R.J.J. Grand, V. Springel, D. Kawata, I. Minchev, P. Sánchez-Blázquez, F. A. Gómez, F. Marinacci, R. Pakmor, and D. J. R. Campbell. Spiral-induced velocity and metallicity patterns in a cosmological zoom simulation of a Milky Way-sized galaxy. *MNRAS*, 460:L94–L98, July 2016. doi: 10.1093/mnrasl/slw086.

J. Guedes, S. Callegari, P. Madau, and L. Mayer. Forming Realistic Late-type Spirals in a ΛCDM Universe: The Eris Simulation. *ApJ*, 742:76, December 2011. doi: 10.1088/0004-637X/742/2/76.

J. E. Gunn. The evolution of galaxies. In H. A. Brueck, G. V. Coyne, and M. S. Longair, editors, *Astrophysical Cosmology Proceedings*, pages 233–259, 1982.

L. Gutiérrez, P. Erwin, R. Aladro, and J. E. Beckman. The Outer Disks of Early-type Galaxies. II. Surface-brightness Profiles of Unbarred Galaxies and Trends with Hubble Type. *AJ*, 142:145, November 2011. doi: 10.1088/0004-6256/142/5/145.

J. T. C. G. Head, J. R. Lucey, and M. J. Hudson. Beyond Sérsic + exponential disc morphologies in the Coma Cluster. *MNRAS*, 453:3729–3753, November 2015. doi: 10.1093/mnras/stv1662.

L. Hernquist. An analytical model for spherical galaxies and bulges. *ApJ*, 356:359–364, June 1990. doi: 10.1086/168845.

J. Herpich, G. S. Stinson, A. A. Dutton, H.-W. Rix, M. Martig, R. Roškar, A. V. Macciò, T. R. Quinn, and J. Wadsley. How to bend galaxy disc profiles: the role of halo spin. *MNRAS*, 448:L99–L103, March 2015a. doi: 10.1093/mnrasl/slv006.

J. Herpich, G. S. Stinson, H.-W. Rix, M. Martig, and A. A. Dutton. How to bend galaxy disc profiles II: stars surfing the bar in anti-truncated discs. *ArXiv e-prints*, November 2015b.

J. Herpich, S. Tremaine, and H.-W. Rix. Galactic disc profiles and a universal angular momentum distribution from statistical physics. *ArXiv e-prints*, December 2017.

K. A. Herrmann and R. Ciardullo. Planetary Nebulae in Face-On Spiral Galaxies. III. Planetary Nebula Kinematics and Disk Mass. *ApJ*, 705:1686–1703, November 2009. doi: 10.1088/0004-637X/705/2/1686.

J. F. W. Herschel. Catalogue of Nebulae and Clusters of Stars. *Royal Society of London Philosophical Transactions Series I*, 154:1–137, 1864.

F. Hohl. Numerical Experiments with a Disk of Stars. *ApJ*, 168:343, September 1971. doi: 10.1086/151091.

P. F. Hopkins. A general class of Lagrangian smoothed particle hydrodynamics methods and implications for fluid mixing problems. *MNRAS*, 428:2840–2856, February 2013. doi: 10.1093/mnras/sts210.

P. F. Hopkins, D. Kereš, J. Oñorbe, C.-A. Faucher-Giguère, E. Quataert, N. Murray, and J. S. Bullock. Galaxies on FIRE (Feedback In Realistic Environments): stellar feedback explains cosmologically inefficient star formation. *MNRAS*, 445:581–603, November 2014. doi: 10.1093/mnras/stu1738.

E. Hubble. A Relation between Distance and Radial Velocity among Extra-Galactic Nebulae. *Proceedings of the National Academy of Science*, 15:168–173, March 1929. doi: 10.1073/pnas.15.3.168.

E. P. Hubble. Cepheids in spiral nebulae. *The Observatory*, 48:139–142, May 1925.

E. P. Hubble. A spiral nebula as a stellar system: Messier 33. *ApJ*, 63:236–274, May 1926a. doi: 10.1086/142976.

E. P. Hubble. Extragalactic nebulae. *ApJ*, 64:321–369, December 1926b. doi: 10.1086/143018.

E. P. Hubble. *Realm of the Nebulae.* 1936.

M. J. Hudson, B. R. Gillis, J. Coupon, H. Hildebrandt, T. Erben, C. Heymans, H. Hoekstra, T. D. Kitching, Y. Mellier, L. Miller, L. Van Waerbeke, C. Bonnett, L. Fu, K. Kuijken, B. Rowe, T. Schrabback, E. Semboloni, E. van Uitert, and M. Velander. CFHTLenS: co-evolution of galaxies and their dark matter haloes. *MNRAS*, 447:298–314, February 2015. doi: 10.1093/mnras/stu2367.

J. H. Jeans. *Problems of cosmogony and stellar dynamics.* 1919.

L. Jetley, P. Wesolowski, F. Gioachin, C. Mendes, L. V. Kale, and T. R. Quinn. Scaling hierarchical n-body simulations on gpu clusters. *In Proceedings of the 2010 ACM/IEEE International Conference for High Performance Computing, Networking, Storage and Analysis*, SC '10, 2010.

P. Jetley, F. Gioachin, C. Mendes, L. V. Kale, and T. R. Quinn. Massively parallel cosmological simulations with changa. *Proceedings of IEEE International Parallel and Distributed Processing Symposium 2008*, 2008.

W. H. Julian and A. Toomre. Non-Axisymmetric Responses of Differentially Rotating Disks of Stars. *ApJ*, 146:810, December 1966. doi: 10.1086/148957.

N. Katz. Dissipational galaxy formation. II - Effects of star formation. *ApJ*, 391:502–517, June 1992. doi: 10.1086/171366.

T. Kaufmann, L. Mayer, J. Wadsley, J. Stadel, and B. Moore. Angular momentum transport and disc morphology in smoothed particle hydrodynamics simulations of galaxy formation. *MNRAS*, 375: 53–67, February 2007. doi: 10.1111/j.1365-2966.2006.11314.x.

S. Kazantzidis, J. Magorrian, and B. Moore. Generating Equilibrium Dark Matter Halos: Inadequacies of the Local Maxwellian Approximation. *ApJ*, 601:37–46, January 2004. doi: 10.1086/380192.

S. Kazantzidis, A. R. Zentner, A. V. Kravtsov, J. S. Bullock, and V. P. Debattista. Cold Dark Matter Substructure and Galactic Disks. II. Dynamical Effects of Hierarchical Satellite Accretion. *ApJ*, 700: 1896–1920, August 2009. doi: 10.1088/0004-637X/700/2/1896.

B. W. Keller, J. Wadsley, S. M. Benincasa, and H.M.P. Couchman. A superbubble feedback model for galaxy simulations. *MNRAS*, 442:3013–3025, August 2014. doi: 10.1093/mnras/stu1058.

B. W. Keller, J. Wadsley, and H. M. P. Couchman. Cosmological galaxy evolution with superbubble feedback - I. Realistic galaxies with moderate feedback. *MNRAS*, 453:3499–3509, November 2015. doi: 10.1093/mnras/stv1789.

B. W. Keller, J. Wadsley, and H. M. P. Couchman. Cosmological galaxy evolution with superbubble feedback - II. The limits of supernovae. *MNRAS*, 463:1431–1445, December 2016. doi: 10.1093/ mnras/stw2029.

R. C. Kennicutt, Jr. The star formation law in galactic disks. *ApJ*, 344:685–703, September 1989. doi: 10.1086/167834.

R. C. Kennicutt, Jr. The Global Schmidt Law in Star-forming Galaxies. *ApJ*, 498:541, May 1998. doi: 10.1086/305588.

A. Klypin, A. V. Kravtsov, O. Valenzuela, and F. Prada. Where Are the Missing Galactic Satellites? *ApJ*, 522:82–92, September 1999. doi: 10.1086/307643.

J. Kormendy. Brightness distributions in compact and normal galaxies. II - Structure parameters of the spheroidal component. *ApJ*, 218:333–346, December 1977. doi: 10.1086/155687.

M. Kregel, P. C. van der Kruit, and R. de Grijs. Flattening and truncation of stellar discs in edge-on spiral galaxies. *MNRAS*, 334:646–668, August 2002. doi: 10.1046/j.1365-8711.2002.05556.x.

J. Laine, E. Laurikainen, H. Salo, S. Comerón, R. J. Buta, D. Zaritsky, E. Athanassoula, A. Bosma, J.-C. Muñoz-Mateos, D. A. Gadotti, J. L. Hinz, S. Erroz-Ferrer, A. Gil de Paz, T. Kim, K. Menéndez-Delmestre, T. Mizusawa, M. W. Regan, M. Seibert, and K. Sheth. Morphology and environment of galaxies with disc breaks in the S$^4$G and NIRS0S. *MNRAS*, 441:1992–2012, July 2014. doi: 10.1093/mnras/stu628.

R. B. Larson. Models for the formation of disc galaxies. *MNRAS*, 176:31–52, July 1976. doi: 10.1093/ mnras/176.1.31.

H. S. Leavitt and E. C. Pickering. Periods of 25 Variable Stars in the Small Magellanic Cloud. *Harvard College Observatory Circular*, 173:1–3, March 1912.

D.N.C. Lin and J. E. Pringle. The formation of the exponential disk in spiral galaxies. *ApJ*, 320:L87–L91, September 1987. doi: 10.1086/184981.

S. Longair. *The Cosmic Century: A History of Astrophysics and Cosmology*. Cambridge University Press, 2006. ISBN 9780521474368. URL `https://books.google.de/books?id=zOvlYHQZHJcC`.

D. Lynden-Bell. Statistical mechanics of violent relaxation in stellar systems. *MNRAS*, 136:101, 1967. doi: 10.1093/mnras/136.1.101.

D. Lynden-Bell and A. J. Kalnajs. On the generating mechanism of spiral structure. *MNRAS*, 157:1, 1972. doi: 10.1093/mnras/157.1.1.

A. V. Macciò, A. A. Dutton, and F. C. van den Bosch. Concentration, spin and shape of dark matter haloes as a function of the cosmological model: WMAP1, WMAP3 and WMAP5 results. *MNRAS*, 391:1940–1954, December 2008. doi: 10.1111/j.1365-2966.2008.14029.x.

A. V. Macciò, X. Kang, F. Fontanot, R. S. Somerville, S. Koposov, and P. Monaco. Luminosity function and radial distribution of Milky Way satellites in a ΛCDM Universe. *MNRAS*, 402:1995–2008, March 2010. doi: 10.1111/j.1365-2966.2009.16031.x.

A. V. Macciò, G. Stinson, C. B. Brook, J. Wadsley, H.M.P. Couchman, S. Shen, B. K. Gibson, and T. Quinn. Halo Expansion in Cosmological Hydro Simulations: Toward a Baryonic Solution of the Cusp/Core Problem in Massive Spirals. *ApJ*, 744:L9, January 2012. doi: 10.1088/2041-8205/744/1/L9.

D. T. Maltby, M. E. Gray, A. Aragón-Salamanca, C. Wolf, E. F. Bell, S. Jogee, B. Häußler, F. D. Barazza, A. Böhm, and K. Jahnke. The environmental dependence of the structure of outer galactic discs in STAGES spiral galaxies. *MNRAS*, 419:669–686, January 2012a. doi: 10.1111/j.1365-2966.2011.19727.x.

D. T. Maltby, C. Hoyos, M. E. Gray, A. Aragón-Salamanca, and C. Wolf. Antitruncated stellar light profiles in the outer regions of STAGES spiral galaxies: bulge or disc related? *MNRAS*, 420: 2475–2479, March 2012b. doi: 10.1111/j.1365-2966.2011.20211.x.

D. T. Maltby, A. Aragón-Salamanca, M. E. Gray, C. Hoyos, C. Wolf, S. Jogee, and A. Böhm. The environmental dependence of the structure of galactic discs in STAGES S0 galaxies: implications for S0 formation. *MNRAS*, 447:1506–1530, February 2015. doi: 10.1093/mnras/stu2536.

P. Marigo, L. Girardi, A. Bressan, M. A. T. Groenewegen, L. Silva, and G. L. Granato. Evolution of asymptotic giant branch stars. II. Optical to far-infrared isochrones with improved TP-AGB models. *A&A*, 482:883–905, May 2008. doi: 10.1051/0004-6361:20078467.

J. W.-K. Mark. On density waves in galaxies. IV - Wave amplification through processes that remove angular momentum from galactic disks. *ApJ*, 206:418–434, June 1976. doi: 10.1086/154396.

S. Mashchenko, H.M.P. Couchman, and J. Wadsley. The removal of cusps from galaxy centres by stellar feedback in the early Universe. *Nature*, 442:539–542, August 2006. doi: 10.1038/nature04944.

S. Mashchenko, J. Wadsley, and H.M.P. Couchman. Stellar Feedback in Dwarf Galaxy Formation. *Science*, 319:174–, January 2008. doi: 10.1126/science.1148666.

L. Mayer, F. Governato, and T. Kaufmann. The formation of disk galaxies in computer simulations. *Advanced Science Letters*, 1:7–27, June 2008.

H. Menon, L. Wesolowski, G. Zheng, P. Jetley, L. Kale, T. Quinn, and F. Governato. Adaptive Techniques for Clustered N-Body Cosmological Simulations. *ArXiv e-prints*, September 2014.

C. Messier. Catalogue des Nébuleuses & des amas d'Étoiles (Catalog of Nebulae and Star Clusters). Technical report, 1781.

L. Mestel. On the galactic law of rotation. *MNRAS*, 126:553, 1963. doi: 10.1093/mnras/126.6.553.

I. Minchev and B. Famaey. A New Mechanism for Radial Migration in Galactic Disks: Spiral-Bar Resonance Overlap. *ApJ*, 722:112–121, October 2010. doi: 10.1088/0004-637X/722/1/112.

I. Minchev, B. Famaey, F. Combes, P. Di Matteo, M. Mouhcine, and H. Wozniak. Radial migration in galactic disks caused by resonance overlap of multiple patterns: Self-consistent simulations. *A&A*, 527:A147, March 2011. doi: 10.1051/0004-6361/201015139.

I. Minchev, B. Famaey, A. C. Quillen, P. Di Matteo, F. Combes, M. Vlajić, P. Erwin, and J. Bland-Hawthorn. Evolution of galactic discs: multiple patterns, radial migration, and disc outskirts. *A&A*, 548:A126, December 2012. doi: 10.1051/0004-6361/201219198.

I. Minchev, C. Chiappini, and M. Martig. Chemodynamical evolution of the Milky Way disk. I. The solar vicinity. *A&A*, 558:A9, October 2013. doi: 10.1051/0004-6361/201220189.

H. Mo, F. van den Bosch, and S. White. *Galaxy Formation and Evolution*. Galaxy Formation and Evolution. Cambridge University Press, 2010. ISBN 9780521857932. URL https://books.google.de/books?id=Zj7fDU3Z4wsC.

H. J. Mo and S. Mao. Galaxy formation in pre-processed dark haloes. *MNRAS*, 353:829–840, September 2004. doi: 10.1111/j.1365-2966.2004.08114.x.

H. J. Mo, S. Mao, and S. D. M. White. The formation of galactic discs. *MNRAS*, 295:319–336, April 1998. doi: 10.1046/j.1365-8711.1998.01227.x.

B. Moore. Evidence against dissipation-less dark matter from observations of galaxy haloes. *Nature*, 370:629–631, August 1994. doi: 10.1038/370629a0.

B. Moore. Dark matter. *Royal Society of London Philosophical Transactions Series A*, 357:3259, December 1999. doi: 10.1098/rsta.1999.0493.

B. P. Moster, R. S. Somerville, C. Maulbetsch, F. C. van den Bosch, A. V. Macciò, T. Naab, and L. Oser. Constraints on the Relationship between Stellar Mass and Halo Mass at Low and High Redshift. *ApJ*, 710:903–923, February 2010. doi: 10.1088/0004-637X/710/2/903.

B. P. Moster, T. Naab, and S. D. M. White. Galactic star formation and accretion histories from matching galaxies to dark matter haloes. *MNRAS*, 428:3121–3138, February 2013. doi: 10.1093/mnras/sts261.

T. Naab and J. P. Ostriker. Theoretical Challenges in Galaxy Formation. *ArXiv e-prints*, December 2016.

J. F. Navarro and W. Benz. Dynamics of cooling gas in galactic dark halos. *ApJ*, 380:320–329, October 1991. doi: 10.1086/170590.

J. F. Navarro and M. Steinmetz. The Effects of a Photoionizing Ultraviolet Background on the Formation of Disk Galaxies. *ApJ*, 478:13–28, March 1997. doi: 10.1086/303763.

J. F. Navarro and M. Steinmetz. Dark Halo and Disk Galaxy Scaling Laws in Hierarchical Universes. *ApJ*, 538:477–488, August 2000. doi: 10.1086/309175.

J. F. Navarro and S.D.M. White. Simulations of dissipative galaxy formation in hierarchically clustering universes-2. Dynamics of the baryonic component in galactic haloes. *MNRAS*, 267:401–412, March 1994. doi: 10.1093/mnras/267.2.401.

J. F. Navarro, V. R. Eke, and C. S. Frenk. The cores of dwarf galaxy haloes. *MNRAS*, 283:L72–L78, December 1996. doi: 10.1093/mnras/283.3.L72.

J. F. Navarro, C. S. Frenk, and S.D.M. White. A Universal Density Profile from Hierarchical Clustering. *ApJ*, 490:493, December 1997. doi: 10.1086/304888.

M. Ness, D. W. Hogg, H.-W. Rix, M. Martig, M. H. Pinsonneault, and A. Y. Q. Ho. Spectroscopic Determination of Masses (and Implied Ages) for Red Giants. *ApJ*, 823:114, June 2016. doi: 10.3847/0004-637X/823/2/114.

S. Nickerson, G. Stinson, H.M.P. Couchman, J. Bailin, and J. Wadsley. Mechanisms of baryon loss for dark satellites in cosmological smoothed particle hydrodynamics simulations. *MNRAS*, 415: 257–270, July 2011. doi: 10.1111/j.1365-2966.2011.18700.x.

K. G. Noeske, B. J. Weiner, S. M. Faber, C. Papovich, D. C. Koo, R. S. Somerville, K. Bundy, C. J. Conselice, J. A. Newman, D. Schiminovich, E. Le Floc'h, A. L. Coil, G. H. Rieke, J. M. Lotz, J. R. Primack, P. Barmby, M. C. Cooper, M. Davis, R. S. Ellis, G. G. Fazio, P. Guhathakurta, J. Huang, S. A. Kassin, D. C. Martin, A. C. Phillips, R. M. Rich, T. A. Small, C. N. A. Willmer, and G. Wilson. Star Formation in AEGIS Field Galaxies since z=1.1: The Dominance of Gradually Declining Star Formation, and the Main Sequence of Star-forming Galaxies. *ApJ*, 660:L43–L46, May 2007. doi: 10.1086/517926.

J. North. *Cosmos: An Illustrated History of Astronomy and Cosmology*. University of Chicago Press, 2008. ISBN 9780226594415. URL http://books.google.de/books?id=qq8Luhs7rTUC.

T. Okamoto, V. R. Eke, C. S. Frenk, and A. Jenkins. Effects of feedback on the morphology of galaxy discs. *MNRAS*, 363:1299–1314, November 2005. doi: 10.1111/j.1365-2966.2005.09525.x.

F. S. Patterson. The Luminosity Gradient of Messier 33. *Harvard College Observatory Bulletin*, 914: 9–10, December 1940.

P. J. E. Peebles. Origin of the Angular Momentum of Galaxies. *ApJ*, 155:393, February 1969. doi: 10.1086/149876.

M. S. Peeples and F. Shankar. Constraints on star formation driven galaxy winds from the mass-metallicity relation at z= 0. *MNRAS*, 417:2962–2981, November 2011. doi: 10.1111/j.1365-2966.2011.19456.x.

A. A. Penzias and R. W. Wilson. A Measurement of Excess Antenna Temperature at 4080 Mc/s. *ApJ*, 142:419–421, July 1965. doi: 10.1086/148307.

S. Perlmutter, G. Aldering, G. Goldhaber, R. A. Knop, P. Nugent, P. G. Castro, S. Deustua, S. Fabbro, A. Goobar, D. E. Groom, I. M. Hook, A. G. Kim, M. Y. Kim, J. C. Lee, N. J. Nunes, R. Pain, C. R. Pennypacker, R. Quimby, C. Lidman, R. S. Ellis, M. Irwin, R. G. McMahon, P. Ruiz-Lapuente, N. Walton, B. Schaefer, B. J. Boyle, A. V. Filippenko, T. Matheson, A. S. Fruchter, N. Panagia, H. J. M. Newberg, W. J. Couch, and T. S. C. Project. Measurements of $\Omega$ and $\Lambda$ from 42 High-Redshift Supernovae. *ApJ*, 517:565–586, June 1999. doi: 10.1086/307221.

A. H. G. Peter. Dark matter: A brief review. In *Frank N. Bash Symposium 2011: New Horizons in Astronomy*, 2012.

S. P. C. Peters, G. de Geyter, P. C. van der Kruit, and K. C. Freeman. The shape of dark matter haloes - IV. The structure of stellar discs in edge-on galaxies. *MNRAS*, 464:48–64, January 2017. doi: 10.1093/mnras/stw2100.

Planck Collaboration, P. A. R. Ade, N. Aghanim, M. Arnaud, M. Ashdown, J. Aumont, C. Baccigalupi, A. J. Banday, R. B. Barreiro, J. G. Bartlett, and et al. Planck 2015 results. XIII. Cosmological parameters. *A&A*, 594:A13, September 2016. doi: 10.1051/0004-6361/201525830.

M. Pohlen and I. Trujillo. The structure of galactic disks. Studying late-type spiral galaxies using SDSS. *A&A*, 454:759–772, August 2006. doi: 10.1051/0004-6361:20064883.

M. Pohlen, R.-J. Dettmar, and R. Lütticke. Cut-off radii of galactic disks . A new statistical study on the truncation of galactic disks. *A&A*, 357:L1–L4, May 2000.

M. Pohlen, R. Lütticke, and R.-J. Dettmar. Cut-Off Radii of Galactic Disks. In J. G. Funes and E. M. Corsini, editors, *Galaxy Disks and Disk Galaxies*, volume 230 of *Astronomical Society of the Pacific Conference Series*, pages 135–136, 2001.

M. Pohlen, R.-J. Dettmar, R. Lütticke, and G. Aronica. Outer edges of face-on spiral galaxies. Deep optical imaging of NGC 5923, UGC 9837 and NGC 5434. *A&A*, 392:807–816, September 2002. doi: 10.1051/0004-6361:20020994.

A. Pontzen and F. Governato. How supernova feedback turns dark matter cusps into cores. *MNRAS*, 421:3464–3471, April 2012. doi: 10.1111/j.1365-2966.2012.20571.x.

A. Pontzen, R. Roškar, G. Stinson, and R. Woods. pynbody: N-Body/SPH analysis for python. Astrophysics Source Code Library, May 2013.

A. C. Quillen. Chaos Caused by Resonance Overlap in the Solar Neighborhood: Spiral Structure at the Bar's Outer Lindblad Resonance. *AJ*, 125:785–793, February 2003. doi: 10.1086/345725.

A. C. Quillen, J. Dougherty, M. B. Bagley, I. Minchev, and J. Comparetta. Structure in phase space associated with spiral and bar density waves in an N-body hybrid galactic disc. *MNRAS*, 417: 762–784, October 2011. doi: 10.1111/j.1365-2966.2011.19349.x.

D. J. Radburn-Smith, R. Roškar, V. P. Debattista, J. J. Dalcanton, D. Streich, R. S. de Jong, M. Vlajić, B. W. Holwerda, C. W. Purcell, A. E. Dolphin, and D. B. Zucker. Outer-disk Populations in NGC 7793: Evidence for Stellar Radial Migration. *ApJ*, 753:138, July 2012. doi: 10.1088/0004-637X/753/2/138.

J. I. Read and G. Gilmore. Mass loss from dwarf spheroidal galaxies: the origins of shallow dark matter cores and exponential surface brightness profiles. *MNRAS*, 356:107–124, January 2005. doi: 10.1111/j.1365-2966.2004.08424.x.

A. G. Riess, A. V. Filippenko, P. Challis, A. Clocchiatti, A. Diercks, P. M. Garnavich, R. L. Gilliland, C. J. Hogan, S. Jha, R. P. Kirshner, B. Leibundgut, M. M. Phillips, D. Reiss, B. P. Schmidt, R. A. Schommer, R. C. Smith, J. Spyromilio, C. Stubbs, N. B. Suntzeff, and J. Tonry. Observational Evidence from Supernovae for an Accelerating Universe and a Cosmological Constant. *AJ*, 116: 1009–1038, September 1998. doi: 10.1086/300499.

B. W. Ritchie and P. A. Thomas. Multiphase smoothed-particle hydrodynamics. *MNRAS*, 323:743–756, May 2001. doi: 10.1046/j.1365-8711.2001.04268.x.

M. S. Roberts. M 31 and a Brief History of Dark Matter. In A. H. Bridle, J. J. Condon, and G. C. Hunt, editors, *Frontiers of Astrophysics: A Celebration of NRAO's 50th Anniversary*, volume 395 of *Astronomical Society of the Pacific Conference Series*, page 283, August 2008.

B. Robertson, N. Yoshida, V. Springel, and L. Hernquist. Disk Galaxy Formation in a Λ Cold Dark Matter Universe. *ApJ*, 606:32–45, May 2004. doi: 10.1086/382871.

J. C. Roediger, S. Courteau, P. Sánchez-Blázquez, and M. McDonald. Stellar Populations and Radial Migrations in Virgo Disk Galaxies. *ApJ*, 758:41, October 2012. doi: 10.1088/0004-637X/758/1/41.

M. Romero-Gómez, J. J. Masdemont, E. Athanassoula, and C. García-Gómez. The origin of $rR_1$ ring structures in barred galaxies. *A&A*, 453:39–45, July 2006. doi: 10.1051/0004-6361:20054653.

M. Romero-Gómez, E. Athanassoula, J. J. Masdemont, and C. García-Gómez. The formation of spiral arms and rings in barred galaxies. *A&A*, 472:63–75, September 2007. doi: 10.1051/0004-6361: 20077504.

R. Roškar, V. P. Debattista, G. S. Stinson, T. R. Quinn, T. Kaufmann, and J. Wadsley. Beyond Inside-Out Growth: Formation and Evolution of Disk Outskirts. *ApJ*, 675:L65–L68, 3 2008a. doi: 10.1086/586734.

R. Roškar, V. P. Debattista, T. R. Quinn, G. S. Stinson, and J. Wadsley. Riding the Spiral Waves: Implications of Stellar Migration for the Properties of Galactic Disks. *ApJ*, 684:L79–L82, 9 2008b. doi: 10.1086/592231.

R. Roškar, V. P. Debattista, T. R. Quinn, and J. Wadsley. Radial migration in disc galaxies - I. Transient spiral structure and dynamics. *MNRAS*, 426:2089–2106, November 2012. doi: 10.1111/j.1365-2966. 2012.21860.x.

T. Ruiz-Lara, I. Pérez, E. Florido, P. Sánchez-Blázquez, J. Méndez-Abreu, M. Lyubenova, J. Falcón-Barroso, L. Sánchez-Menguiano, S. F. Sánchez, L. Galbany, R. García-Benito, R. M. González Delgado, B. Husemann, C. Kehrig, Á. R. López-Sánchez, R. A. Marino, D. Mast, P. Papaderos, G. van de Ven, C. J. Walcher, S. Zibetti, and the CALIFA team. No direct coupling between bending of galaxy disc stellar age and light profiles. *ArXiv e-prints*, November 2015.

P. Sánchez-Blázquez, F. F. Rosales-Ortega, J. Méndez-Abreu, I. Pérez, S. F. Sánchez, S. Zibetti, J. A. L. Aguerri, J. Bland-Hawthorn, C. Catalán-Torrecilla, R. Cid Fernandes, A. de Amorim, A. de Lorenzo-Caceres, J. Falcón-Barroso, A. Galazzi, R. García Benito, A. Gil de Paz, R. González Delgado, B. Husemann, J. Iglesias-Páramo, B. Jungwiert, R. A. Marino, I. Márquez, D. Mast, M. A. Mendoza, M. Mollá, P. Papaderos, T. Ruiz-Lara, G. van de Ven, C. J. Walcher, and L. Wisotzki. Stellar population gradients in galaxy discs from the CALIFA survey. The influence of bars. *A&A*, 570:A6, October 2014. doi: 10.1051/0004-6361/201423635.

L. Sánchez-Menguiano, S. F. Sánchez, D. Kawata, L. Chemin, I. Pérez, T. Ruiz-Lara, P. Sánchez-Blázquez, L. Galbany, J. P. Anderson, R. J. J. Grand, I. Minchev, and F. A. Gómez. Evidence of Ongoing Radial Migration in NGC 6754: Azimuthal Variations of the Gas Properties. *ApJ*, 830:L40, October 2016. doi: 10.3847/2041-8205/830/2/L40.

R. Sancisi. The visible matter – dark matter coupling. In S. Ryder, D. Pisano, M. Walker, and K. Freeman, editors, *Dark Matter in Galaxies*, volume 220 of *IAU Symposium*, page 233, July 2004.

A. Sandage, K. C. Freeman, and N. R. Stokes. The Intrinsic Flattening of e, so, and Spiral Galaxies as Related to Galaxy Formation and Evolution. *ApJ*, 160:831, June 1970. doi: 10.1086/150475.

T. Sawala, C. S. Frenk, A. Fattahi, J. F. Navarro, R. G. Bower, R. A. Crain, C. Dalla Vecchia, M. Furlong, J. C. Helly, A. Jenkins, K. A. Oman, M. Schaller, J. Schaye, T. Theuns, J. Trayford, and S. D. M. White. The APOSTLE simulations: solutions to the Local Group's cosmic puzzles. *MNRAS*, 457:1931–1943, April 2016. doi: 10.1093/mnras/stw145.

B. M. Schäfer. Galactic Angular Momenta and Angular Momentum Correlations in the Cosmological Large-Scale Structure. *International Journal of Modern Physics D*, 18:173–222, 2009. doi: 10.1142/S0218271809014388.

R. Schönrich and J. Binney. Chemical evolution with radial mixing. *MNRAS*, 396:203–222, June 2009. doi: 10.1111/j.1365-2966.2009.14750.x.

R. Schönrich and P. McMillan. Understanding inverse metallicity gradients in galactic discs as a consequence of inside-out formation. *ArXiv e-prints*, May 2016.

J. A. Sellwood. Spiral Instabilities in N-body Simulations. I. Emergence from Noise. *ApJ*, 751:44, May 2012. doi: 10.1088/0004-637X/751/1/44.

J. A. Sellwood. Secular evolution in disk galaxies. *Reviews of Modern Physics*, 86:1–46, January 2014. doi: 10.1103/RevModPhys.86.1.

J. A. Sellwood and J. J. Binney. Radial mixing in galactic discs. *MNRAS*, 336:785–796, November 2002. doi: 10.1046/j.1365-8711.2002.05806.x.

J. A. Sellwood and R. G. Carlberg. Spiral instabilities provoked by accretion and star formation. *ApJ*, 282:61–74, July 1984. doi: 10.1086/162176.

R. Sengerling and J. North. *Viewegs Geschichte der Astronomie und Kosmologie: Aus dem Englischen übersetzt von Rainer Sengerling*. Springer Berlin Heidelberg, 2012. ISBN 9783642638954. URL https://books.google.de/books?id=vcwfnwEACAAJ.

S. Shen, J. Wadsley, and G. Stinson. The enrichment of the intergalactic medium with adiabatic feedback - I. Metal cooling and metal diffusion. *MNRAS*, 407:1581–1596, September 2010. doi: 10.1111/j.1365-2966.2010.17047.x.

D. Sijacki, M. Vogelsberger, S. Genel, V. Springel, P. Torrey, G. F. Snyder, D. Nelson, and L. Hernquist. The Illustris simulation: the evolving population of black holes across cosmic time. *MNRAS*, 452: 575–596, September 2015. doi: 10.1093/mnras/stv1340.

M. Solway, J. A. Sellwood, and R. Schönrich. Radial migration in galactic thick discs. *MNRAS*, 422: 1363–1383, May 2012. doi: 10.1111/j.1365-2966.2012.20712.x.

R. S. Somerville and R. Davé. Physical Models of Galaxy Formation in a Cosmological Framework. *ARAA*, 53:51–113, August 2015. doi: 10.1146/annurev-astro-082812-140951.

J. Sommer-Larsen, S. Gelato, and H. Vedel. Formation of Disk Galaxies: Feedback and the Angular Momentum Problem. *ApJ*, 519:501–512, July 1999. doi: 10.1086/307374.

J. Sommer-Larsen, M. Götz, and L. Portinari. Galaxy Formation: Cold Dark Matter, Feedback, and the Hubble Sequence. *ApJ*, 596:47–66, October 2003. doi: 10.1086/377685.

L. Spitzer, Jr. and M. Schwarzschild. The Possible Influence of Interstellar Clouds on Stellar Velocities. *ApJ*, 114:385, November 1951. doi: 10.1086/145478.

V. Springel and S. D. M. White. Tidal tails in cold dark matter cosmologies. *MNRAS*, 307:162–178, July 1999. doi: 10.1046/j.1365-8711.1999.02613.x.

V. Springel, C. S. Frenk, and S. D. M. White. The large-scale structure of the Universe. *Nature*, 440: 1137–1144, April 2006. doi: 10.1038/nature04805.

M. Steinmetz and E. Muller. The formation of disc galaxies in a cosmological context: structure and kinematics. *MNRAS*, 276:549–562, September 1995. doi: 10.1093/mnras/276.2.549.

K. R. Stewart, A. M. Brooks, J. S. Bullock, A. H. Maller, J. Diemand, J. Wadsley, and L. A. Moustakas. Angular Momentum Acquisition in Galaxy Halos. *ApJ*, 769:74, May 2013. doi: 10.1088/0004-637X/769/1/74.

G. Stinson, A. Seth, N. Katz, J. Wadsley, F. Governato, and T. Quinn. Star formation and feedback in smoothed particle hydrodynamic simulations - I. Isolated galaxies. *MNRAS*, 373:1074–1090, December 2006. doi: 10.1111/j.1365-2966.2006.11097.x.

G. S. Stinson, C. Brook, A. V. Macciò, J. Wadsley, T. R. Quinn, and H. M. P. Couchman. Making Galaxies In a Cosmological Context: the need for early stellar feedback. *MNRAS*, 428:129–140, January 2013. doi: 10.1093/mnras/sts028.

C. Struck and B. G. Elmegreen. Near-exponential surface densities as hydrostatic, non-equilibrium profiles in galaxy discs. *MNRAS*, 464:1482–1492, January 2017. doi: 10.1093/mnras/stw2462.

R. A. Swaters, B. F. Madore, F. C. van den Bosch, and M. Balcells. The Central Mass Distribution in Dwarf and Low Surface Brightness Galaxies. *ApJ*, 583:732–751, February 2003. doi: 10.1086/345426.

A. Toomre. On the gravitational stability of a disk of stars. *ApJ*, 139:1217–1238, May 1964. doi: 10.1086/147861.

A. Toomre. Mergers and Some Consequences. In B. M. Tinsley and R. B. G. Larson, D. Campbell, editors, *Evolution of Galaxies and Stellar Populations*, page 401, 1977.

S. Tremaine and J. P. Ostriker. Relaxation in stellar systems, and the shape and rotation of the inner dark halo. *MNRAS*, 306:662–668, July 1999. doi: 10.1046/j.1365-8711.1999.02558.x.

C. A. Tremonti, T. M. Heckman, G. Kauffmann, J. Brinchmann, S. Charlot, S. D. M. White, M. Seibert, E. W. Peng, D. J. Schlegel, A. Uomoto, M. Fukugita, and J. Brinkmann. The Origin of the Mass-Metallicity Relation: Insights from 53,000 Star-forming Galaxies in the Sloan Digital Sky Survey. *ApJ*, 613:898–913, October 2004. doi: 10.1086/423264.

R. B. Tully and J. R. Fisher. A new method of determining distances to galaxies. *A&A*, 54:661–673, February 1977.

H. Übler, T. Naab, L. Oser, M. Aumer, L. V. Sales, and S. D. M. White. Why stellar feedback promotes disc formation in simulated galaxies. *MNRAS*, 443:2092–2111, September 2014. doi: 10.1093/mnras/stu1275.

P. C. van der Kruit. Optical surface photometry of eight spiral galaxies studied in Westerbork. *A&AS*, 38:15–38, October 1979.

P. C. van der Kruit. The radial distribution of surface brightness in galactic disks. *A&A*, 173:59–80, February 1987.

P. C. van der Kruit. The three-dimensional distribution of light and mass in disks of spiral galaxies. *A&A*, 192:117–127, March 1988.

P. C. van der Kruit and R. J. Allen. The kinematics of spiral and irregular galaxies. *ARAA*, 16:103–139, 1978. doi: 10.1146/annurev.aa.16.090178.000535.

P. C. van der Kruit and K. C. Freeman. Galaxy Disks. *ARAA*, 49:301–371, September 2011. doi: 10.1146/annurev-astro-083109-153241.

P. C. van der Kruit and L. Searle. Surface photometry of edge-on spiral galaxies. I - A model for the three-dimensional distribution of light in galactic disks. *A&A*, 95:105–115, February 1981a.

P. C. van der Kruit and L. Searle. Surface Photometry of Edge-On Spiral Galaxies. II - the Distribution of Light and Colour in the Disk and Spheroid of NGC891. *A&A*, 95:116, February 1981b.

P. C. van der Kruit and L. Searle. Surface photometry of edge-on spiral galaxies. III - Properties of the three-dimensional distribution of light and mass in disks of spiral galaxies. *A&A*, 110:61–78, June 1982.

C. J. van Houten, J. H. Oort, and W. A. Hiltner. Photoelectric Measurements of Extragalactic Nebulae. *ApJ*, 120:439, November 1954. doi: 10.1086/145933.

C. Vera-Ciro, E. D'Onghia, and J. F. Navarro. The imprint of radial migration on the vertical structure of galaxy disks. *ArXiv e-prints*, May 2016.

M. Viel, G. D. Becker, J. S. Bolton, and M. G. Haehnelt. Warm Dark Matter as a solution to the small scale crisis: new constraints from high redshift Lyman-alpha forest data. *arXiv:1306.2314*, June 2013.

M. Vogelsberger, S. Genel, V. Springel, P. Torrey, D. Sijacki, D. Xu, G. Snyder, S. Bird, D. Nelson, and L. Hernquist. Properties of galaxies reproduced by a hydrodynamic simulation. *Nature*, 509:177–182, May 2014a. doi: 10.1038/nature13316.

M. Vogelsberger, S. Genel, V. Springel, P. Torrey, D. Sijacki, D. Xu, G. Snyder, D. Nelson, and L. Hernquist. Introducing the Illustris Project: simulating the coevolution of dark and visible matter in the Universe. *MNRAS*, 444:1518–1547, October 2014b. doi: 10.1093/mnras/stu1536.

J. W. Wadsley, J. Stadel, and T. Quinn. Gasoline: a flexible, parallel implementation of TreeSPH. *New. Astron.*, 9:137–158, February 2004. doi: 10.1016/j.newast.2003.08.004.

L. Wang, A. A. Dutton, G. S. Stinson, A. V. Macciò, C. Penzo, X. Kang, B. W. Keller, and J. Wadsley. NIHAO project - I. Reproducing the inefficiency of galaxy formation across cosmic time with a large sample of cosmological hydrodynamical simulations. *MNRAS*, 454:83–94, November 2015. doi: 10.1093/mnras/stv1937.

A. R. Wetzel, P. F. Hopkins, J.-h. Kim, C.-A. Faucher-Giguère, D. Kereš, and E. Quataert. Reconciling Dwarf Galaxies with ΛCDM Cosmology: Simulating a Realistic Population of Satellites around a Milky Way-mass Galaxy. *ApJ*, 827:L23, August 2016. doi: 10.3847/2041-8205/827/2/L23.

S. D. M. White. Angular momentum growth in protogalaxies. *ApJ*, 286:38–41, November 1984. doi: 10.1086/162573.

S. D. M. White and M. J. Rees. Core condensation in heavy halos - A two-stage theory for galaxy formation and clustering. *MNRAS*, 183:341–358, May 1978. doi: 10.1093/mnras/183.3.341.

D. M. Wilkinson, C. Maraston, D. Thomas, L. Coccato, R. Tojeiro, M. Cappellari, F. Belfiore, M. Bershady, M. Blanton, K. Bundy, S. Cales, B. Cherinka, N. Drory, E. Emsellem, H. Fu, D. Law, C. Li, R. Maiolino, K. Masters, C. Tremonti, D. Wake, E. Wang, A.-M. Weijmans, T. Xiao, R. Yan, K. Zhang, D. Bizyaev, J. Brinkmann, K. Kinemuchi, E. Malanushenko, V. Malanushenko, D. Oravetz, K. Pan, and A. Simmons. P-MaNGA: full spectral fitting and stellar population maps from prototype observations. *MNRAS*, 449:328–360, May 2015. doi: 10.1093/mnras/stv301.

S. Wuyts, N. M. Förster Schreiber, A. van der Wel, B. Magnelli, Y. Guo, R. Genzel, D. Lutz, H. Aussel, G. Barro, S. Berta, A. Cava, J. Graciá-Carpio, N. P. Hathi, K.-H. Huang, D. D. Kocevski, A. M. Koekemoer, K.-S. Lee, E. Le Floc'h, E. J. McGrath, R. Nordon, P. Popesso, F. Pozzi, L. Riguccini, G. Rodighiero, A. Saintonge, and L. Tacconi. Galaxy Structure and Mode of Star Formation in the SFR-Mass Plane from z~2.5 to z~0.1. *ApJ*, 742:96, December 2011. doi: 10.1088/0004-637X/742/2/96.

P. Yoachim, R. Roškar, and V. P. Debattista. Integral Field Unit Spectroscopy of the Stellar Disk Truncation Region of NGC 6155. *ApJ*, 716:L4–L8, June 2010. doi: 10.1088/2041-8205/716/1/L4.

D. G. York, J. Adelman, J. E. Anderson, Jr., S. F. Anderson, J. Annis, N. A. Bahcall, J. A. Bakken, R. Barkhouser, S. Bastian, E. Berman, W. N. Boroski, S. Bracker, C. Briegel, J. W. Briggs, J. Brinkmann, R. Brunner, S. Burles, L. Carey, M. A. Carr, F. J. Castander, B. Chen, P. L. Colestock, A. J. Connolly, J. H. Crocker, I. Csabai, P. C. Czarapata, J. E. Davis, M. Doi, T. Dombeck, D. Eisenstein, N. Ellman, B. R. Elms, M. L. Evans, X. Fan, G. R. Federwitz, L. Fiscelli, S. Friedman, J. A. Frieman, M. Fukugita, B. Gillespie, J. E. Gunn, V. K. Gurbani, E. de Haas, M. Haldeman, F. H. Harris, J. Hayes, T. M. Heckman, G. S. Hennessy, R. B. Hindsley, S. Holm, D. J. Holmgren, C.-h. Huang, C. Hull, D. Husby, S.-I. Ichikawa, T. Ichikawa, Ž. Ivezić, S. Kent, R. S. J. Kim, E. Kinney, M. Klaene, A. N. Kleinman, S. Kleinman, G. R. Knapp, J. Korienek, R. G. Kron, P. Z. Kunszt, D. Q. Lamb, B. Lee, R. F. Leger, S. Limmongkol, C. Lindenmeyer, D. C. Long, C. Loomis, J. Loveday, R. Lucinio, R. H. Lupton, B. MacKinnon, E. J. Mannery, P. M. Mantsch, B. Margon, P. McGehee, T. A. McKay, A. Meiksin, A. Merelli, D. G. Monet, J. A. Munn, V. K. Narayanan, T. Nash, E. Neilsen, R. Neswold, H. J. Newberg, R. C. Nichol, T. Nicinski, M. Nonino, N. Okada, S. Okamura, J. P. Ostriker, R. Owen, A. G. Pauls, J. Peoples, R. L. Peterson, D. Petravick, J. R. Pier, A. Pope, R. Pordes, A. Prosapio, R. Rechenmacher, T. R. Quinn, G. T. Richards, M. W. Richmond, C. H. Rivetta, C. M. Rockosi, K. Ruthmansdorfer, D. Sandford, D. J. Schlegel, D. P. Schneider, M. Sekiguchi, G. Sergey, K. Shimasaku, W. A. Siegmund, S. Smee, J. A. Smith, S. Snedden, R. Stone, C. Stoughton, M. A. Strauss, C. Stubbs, M. SubbaRao, A. S. Szalay, I. Szapudi, G. P. Szokoly, A. R. Thakar, C. Tremonti, D. L. Tucker, A. Uomoto, D. Vanden Berk, M. S. Vogeley, P. Waddell, S.-i. Wang, M. Watanabe, D. H. Weinberg, B. Yanny, N. Yasuda, and SDSS Collaboration. The Sloan Digital Sky Survey: Technical Summary. *AJ*, 120:1579–1587, September 2000. doi: 10.1086/301513.

Y. Yoshii and J. Sommer-Larsen. On the formation of exponential discs. *MNRAS*, 236:779–799, February 1989. doi: 10.1093/mnras/236.4.779.

J. D. Younger, T. J. Cox, A. C. Seth, and L. Hernquist. Antitruncated Stellar Disks via Minor Mergers. *ApJ*, 670:269–278, November 2007. doi: 10.1086/521976.

J. Yu, J. A. Sellwood, C. Pryor, L. Chen, and J. Hou. A Test for Radial Mixing Using Local Star Samples. *ApJ*, 754:124, August 2012. doi: 10.1088/0004-637X/754/2/124.

H. J. Zahid, M. J. Geller, L. J. Kewley, H. S. Hwang, D. G. Fabricant, and M. J. Kurtz. The Chemical Evolution of Star-forming Galaxies over the Last 11 Billion Years. *ApJ*, 771:L19, July 2013. doi: 10.1088/2041-8205/771/2/L19.

A. R. Zentner and J. S. Bullock. Halo Substructure and the Power Spectrum. *ApJ*, 598:49–72, November 2003. doi: 10.1086/378797.

# Acknowledgements

Finishing this work certainly marks a tremendous professional and personal accomplishment. But this is not just my accomplishment. So many family, friends and colleagues contributed to the successful completion of my thesis. Naming all of them would add several pages to this thesis. However, I wish to express special thank to some selected people.

First, and most importantly, I like to thank my wife, Iris and my daughters, Charlotte and Eva. Iris, you are the best partner that I can imagine. I am very grateful for getting to meet, know and love you. I am also very grateful for your love and support. I know that it was not always easy and that I didn't always give you the respect that you deserve. Nevertheless, you put up with all my flaws and imperfections. I love you so very very much.

Charlotte und Eva, euch zu haben, ist das großartigste Geschenk, das mir das Leben je bereitet hat. Eure bedingungslose Liebe ist und bleibt unerreicht. Wenn ich von der Arbeit oder meinem Leben frustriert war, habt ihr mich immer wieder aufgemuntert. Auch wenn es euch nicht bewusst ist – ihr habt einen erheblichen Teil dazu beigetragen, dass ich während meiner Promotion nicht verrückt geworden bin.

Writing this thesis did not start with carrying out the research projects. It was a long way to get to that point and I could have not taken this path without the support of my parents. They supported my interests, when I was a little boy, they were interested in the progress I made at school, they allowed me to study at university, they were always interested in my research, not to mention the moral support that I received. My sister, Juliane, deserves special thanks as well. She has always been a very important person in my life, especially her empathy and willingness to support me when I needed help.

I owe my interest in astronomy to Opa Friedemann. He was the first to teach me about the sky, the planets, and the stars, even before I started school. I dedicate this thesis to you, Opa Friedemann. I wish you would still be there so I could tell you all about it. The seed of curiosity that you planted grew. It had been watered by my teachers at the Gauß-Gymnasium in Frankfurt(Oder), by my professors at university in Heidelberg, and by the people who supervised my research, during my Bachelor, Master, and PhD projects.

I consider myself incredibly lucky to be able to work in the encouraging envi-

**Matthias Bartelmann** helped with the derivation of the angular momentum distribution for maximum entropy disks.

**Scott Tremaine** provided his expertise on galactic dynamics and helped with preparing the third paper in this thesis.

**Tobias Buck, Tobias Schmidt and Michael Walther** helped me with the creation of the mock observational images.

Other people who helped me with their expertise are Jerry Sellwood, Frank van den Bosch and Glenn van de Venn. I thank the anonymous referee of the second paper for their very useful suggestions. Special thanks go to Christian Obermeier and Peter Zeidler for proof reading parts of this thesis.

I also want to thank my friends Botho, Paolo, Ben, and Jasper. They were there for me, when I was going through a personal crisis. I wish we would live closer together. I thank Christina, Ben, and Simon for being great office mates who made my time at the institute even better. We should export our office habits to our future work places. Of course, I also thank all my other friends for being friends. Naming all of you is impossible here but be assured that I did not forget you.

Last but not least, I acknowledge that I am lucky to be part of a society that values the importance of research, including research that society does not benefit from directly. I consider science to be an integral part of human life and I consider it worth to be defended against those who consider it dispensable or discredit it because they are not pleased by its results.